4-19-2016 12:00 AM

Optical Characterization of Anisotropic Interfaces

Renjie Hou
The University of Western Ontario

Supervisor
Dr. François Lagugné-Labarthet
The University of Western Ontario

Graduate Program in Physics

A thesis submitted in partial fulfillment of the requirements for the degree in Doctor of Philosophy

© Renjie Hou 2016

Abstract

The understanding of optical properties of surfaces and interfaces is critical for the development of new technologies ranging from photonics to molecular electronics. Knowing for example the orientation of molecules functionalized onto a surface yields valuable information about the macroscopic properties of the resulting surface. The optical properties can be tuned using various strategies such as molecular functionalization or patterning of meta-structures that ultimately interact with light in a rational way. Advanced optical and spectroscopy methods allowing one to probe such surfaces are therefore key to correlate properties and surface functionalization.

In this thesis, multiple approaches have been taken to understand the optical response of anisotropic interfaces. First, polarization-modulation infrared linear dichroism is used to characterize thin films of azobenzene-containing glasses and follow the dynamic of their orientation. Because of the high charge-transfer of these molecules, their nonlinear properties are also investigated using second harmonic generation microscopy. The coupling of nonlinear active molecules with metallic nanostructures is also investigated using SHG to evaluate the plasmonic enhancements from the nanostructures alone or functionalized with molecules that exhibit high second order hyperpolarizability.

Keywords

Dedication

To my beloved family

Co-Authorship Statement

The following thesis contains material from previously published manuscripts. Dr. François Lagugné-Labarthet was the corresponding author on the presented papers and was responsible for the supervision of Renjie Hou over the course of his studies.

Renjie Hou was a co-author of the published paper presented in Chapter 3, first author of the papers presented in Chapters 4, 6 and 7. The manuscripts corresponding with Chapter 6 and Chapter 7 are still in preparation. He was responsible for the majority of the experimental work as well as the writing and revision for all drafts, including final manuscripts. Some data were jointly acquired and analyzed by co-authors, Clément Lafargue and Radoslaw Kolkowski.

Dr. Kristen E. Snell was the first author of the paper presented in Chapter 3 and was mainly in charge of the synthesis of the molecular glasses studied using the polarization modulation technique. Her contribution is gratefully appreciated.

Acknowledgments

First of all, I would like to acknowledge, with gratitude, my supervisor Dr. François Lagugné-Labarthet for his encouragement and support for all these years. His wisdom and knowledge guided me and enthusiasm gave me strength to go further in not only the path of science, but also the journey of life. It is also his personality I would like to appreciate. His humor makes science more fun. Thanks to him, I had the chance to collaborate with national and international research groups. It would have been impossible for me to achieve anything without his help.

Special thanks to both present and past members of the F.L.L group: Dr. Mohammadali Tabatabaei, Dr. Sylvain Vedraine, Dr. Kristen Snell, Dr. Nastaran Kazemi-Zanjani, Dr. Betty C. Galarreta, Dr. Farshid Pashaee, Gregory Q. Wallace, Shabila Fayyaz, Matt Coady, Bairong Zhang. Thanks for their friendship and support. They made my Ph. D. time more exciting and colorful.

I would also like to acknowledge the staff at Western's Nanofabrication Facility: Tim Goldhawk and Dr. Todd Simpson. Many thanks are extended to all researchers at Dr. Joseph Zyss' research group at Ecole Normale Supérieure de Cachan (Paris, France) in particular Dr. Vasyl Shynkar for his training on the second harmonic generation microscope.

Finally, the love, support and education I received from my family, especially my first physics teacher: my father. Thanks to my grandparents for their understanding of my choice to come to Canada.

Table of Contents

List of Tables

List of Figures

List of Abbreviations, Symbols and Nomenclature

AC	Alternating Current
AFM	atomic force microscopy
APD	avalanche photodiode
AR	anti-reflective
$\boldsymbol{B}$	magnetic field
β_{ijk}	molecular hyper-polarizability
c	speed of light in vacuum
CaF_2	Calcium fluoride
Carb	4-bis(4-tert-butyl)carbazolylphenyl
CD	circular dichroism
CF_3	(3,5-bis(trifluoromethyl)phenyl
C_{Hv}, C_{Hh}	calibration spectra
$\boldsymbol{D}$	displacement field
DC	Direct Current
ΔA	linear dichroism
$\boldsymbol{E}$	electric field
EBL	electron beam lithography
F_θ	distribution function
FT-IR	Fourier transform infrared spectroscopy
$\boldsymbol{H}$	magnetizing field
I	intensity
I_d	total intensity obtained by the detector
$\boldsymbol{J}$	current density
J_0, J_2	zeroth and the second-order Bessel functions
k_b	bond strength
k_i^{or}, k_i^{rel}	rate constant of orientation/relaxation
$\boldsymbol{k_{sp}}$	dispersion along the interface
$\boldsymbol{k_z}$	dispersion normal to the interface
λ	wavelength
LBO	lithium triborate
LD	linear dichroism
LDT	laser damage threshold
LN	liquid nitrogen
l_{sp}	propagation length
LSPR	localized surface plasmon resonance
MCT	mercury cadmium telluride
m_e	mass of an electron
m_i^{or}, m_i^{rel}	weights of rate constants
m_r	reduced mass
n	refrective index
N.A.	numerical aperture
NaCl	Sodium chloride
n_e	number of electrons per unit volume
NI	National Instruments

NLO	nonlinear optics
NSL	nanosphere lithography
$\boldsymbol{P}$	polarizability
pDR1M	poly[4'-(((2-(methacryloyloxy)ethyl)ethyl)-amino)-4-nitroazobenzene-co-Methyl methacrylate]
PEM	photoelastic modulator
PI	Physik Instrumente
$\langle P_i \rangle$	ith order Legendre polynomial
PM-IRLD	polarization modulation infrared dichroism
PM-IRRAS	polarization modulation infrared reflection-adsorption spectroscopy
q	normal coordinate
q_e	electron charge
ρ	charge density
$\boldsymbol{r}$	oscillation induced displacement
SERS	surface enhanced Raman spectroscopy
SHG	second harmonic generation
SHGM	second harmonic generation microscopy
STM	scanning tunneling spectroscopy
T	transmittance
tBu	4-tert-butylphenyl
TCSPC	Time-Correlated Single-Photon Counting
Tg	glass transition temperature
TPPL	two-photon photoluminescence
μ_0	permeability of free-space
μ_d	dipole moment
UI	user interface
ν	stretching mode
VCD	vibrational circular dichroism
$\boldsymbol{\omega_m}$	modulation frequency
χ	susceptibility
$\chi^{(2)}$	second order nonlinear susceptibility
χ_D	dipole contribution to the second-order nonlinear susceptibility
ε_0	permittivity of a dielectric
ε_m	complex dielectric function of a metal
ε_d	permittivity of free-space
τ	lifetime

Chapter 1

1   General introduction

The orientation of molecules at surfaces and interfaces is a parameter of importance for a variety of applications ranging from the manipulation of macroscopic surface properties, catalytic reactivity, to sensing reactions mediated by guest-host recognition. The ability to measure and determine the molecular orientation of bulk or surface samples is therefore important since it enables one to better correlate macroscopic properties to local molecular interactions. This field has been studied since the pioneering work of Irving Langmuir in the early 20th century. Langmuir introduced the concept of molecular monolayer field and was awarded the 1938 Nobel Prize in Chemistry. Since then, many innovations in the field of surface science have enabled new tools to probe surfaces with molecular resolution. The revolution of scanning tunneling microscopy in the early 1980s has played a considerable role by permitting imaging of the geometrical arrangement of single molecule deposited onto pristine single-crystal surfaces. Other techniques based on the use of photons have also yielded very rich information about surfaces that has led to multiple advances in material science such as adhesives, thin-film technology, and materials for photonic applications or hydrophilic/hydrophobic surface properties. For example, a common application of surface science is the use of rubbed polymers for liquid-crystal displays (LCD). The LCD screens that we are all using are technologically complex pieces that need a rubbed surface to pre-orient the LC molecules. This rubbing process orients the surface polymer chains of the screen that will in turn interact with LC molecules and provide them a define anisotropic orientation as opposed to a random isotropic orientation.

Probing the anisotropy of molecules is therefore critical and has thoroughly been studied in the 1980-2000 period using optical techniques through a variety of physical processes. For example, polarization modulation spectroscopy was used to probe birefringence, linear dichroism (LD), and circular dichroism (CD) associated with different spectral ranges. The chirality of molecules or structural units can be accessed by probing the parity of the electronic transitions of the sample. Measurements performed in the mid-infrared range could probe the linear or circular vibrational dichroism providing information about the molecular orientation and local interactions through the analysis of their molecular fingerprints. Such experimental

developments were supported by parallel critical improvements in quantum mechanical modeling associated with density functional theory which was itself enabled by an exponential increase of computational power. In the same 20-year period, nonlinear optical processes were also heavily investigated due to numerous progresses in laser science providing a wide range of wavelengths, pulse width and repetition rates to probe the intimate nature of materials. Second harmonic generation (SHG) has been a technique of choice to determine molecular orientation at solid or liquid interfaces and, unlike linear optical techniques, is intrinsically surface "specific" allowing one to discriminate the surface contribution from the bulk contribution. The spectroscopic version (i.e. broadband) of second-order processes is known as sum-frequency generation (SFG) which can yield absolute information about molecular orientation at surfaces. Since second-order nonlinear optical processes involve two input fields and one output field, polarized and phase measurements show that for a molecule with high symmetry, we can determine an absolute molecular orientation and associated distribution function that takes into consideration the width of the distribution.

Since the 2000s, the interest in nanomaterials and technological nanofabrication methods has naturally led surface scientists to adapt their techniques to investigate the nanoworld and make new critical discoveries such as for graphene. Current research in laser science involves the combination of linear and nonlinear optical processes in microscopic experimental conditions: the laser light source(s) is now directed into a microscope objective with a high numerical aperture, which yields spatial resolution beyond the diffraction limit enabling one to probe static or dynamic processes at the nanoscale. The research in nanoscale science has fostered many new concepts and applications ranging from quantum computers, solar-cell technology and next-generation of high-capacity batteries. Reciprocally, nanomaterials with conductive properties (metals, graphene and carbon nanotubes) have shown specific interactions with light and delineated the field of plasmonics. In simple terms, a plasmon – also called a surface plasmon polariton - is a surface wave originating from the interaction of light with the free electrons of conductive materials. The frequency and the propagation of such wave depend not only on the chemical composition of the materials but also on the shape, the size, and the anisotropy of the conductive nanostructures. Although observed for the first time in the 1902 by Prof. Wood, the theoretical description and coining of the word "Plasmon" occurred 50 years later from the work of Pines and Ritchie (1957). The re-discovery of plasmon waves in the past decade was the result

of intense activity in nanomaterial synthesis, as well as micro-/nano-fabrication technology as highlighted by the historical evolution of manuscripts in the field, as shown in Figure 1-1.[1] The field of plasmonics is multifaceted and aims at conceiving these complex two- or three-dimensional structures as replacement of individual electronic components: performing logical operations using the plasmon wave at the surface of a conductor ultimately driven by an optical field could lead to much faster photonic devices that would surpass the characteristics of current electronic components. This area is still in its infancy, but substantial progress has been made over the past decade as highlighted by Engheta et al.[2] Another very active field is the use of plasmonic materials to use local electromagnetic field enhancements located in the vicinity of metallic nanoparticles. As observed by Ebbesen looking at an array of nanoholes carved into a gold film with dimensions smaller than the wavelength of visible spectrum light[3], the transmitted light was significantly higher than expected. Such observation, due to the local enhancement of light in the vicinity of the nanohole structures, has been exploited for a variety of applications such as in optical data storage,[4-8] biosensing,[9,10] biomarkers,[11-14] and high-sensitivity single-molecule spectroscopy.[15-18] Other families of nanoparticles and structures, such as gold spheres,[19] pyramids,[20] and triangular prisms,[21] have wisely been selected according to their opto-geometric parameters, and their resulting localized surface plasmon resonances (LSPR) have been critically exploited for surface-enhanced spectroscopy effects. For example, surface enhanced Raman spectroscopy (SERS) has been used to yield single molecule detection,[22-24] while tip-enhanced Raman spectroscopy (TERS) reveals molecular functionalization, and defects or features of interest at surfaces with an unprecedented spatial resolution.[25,26]
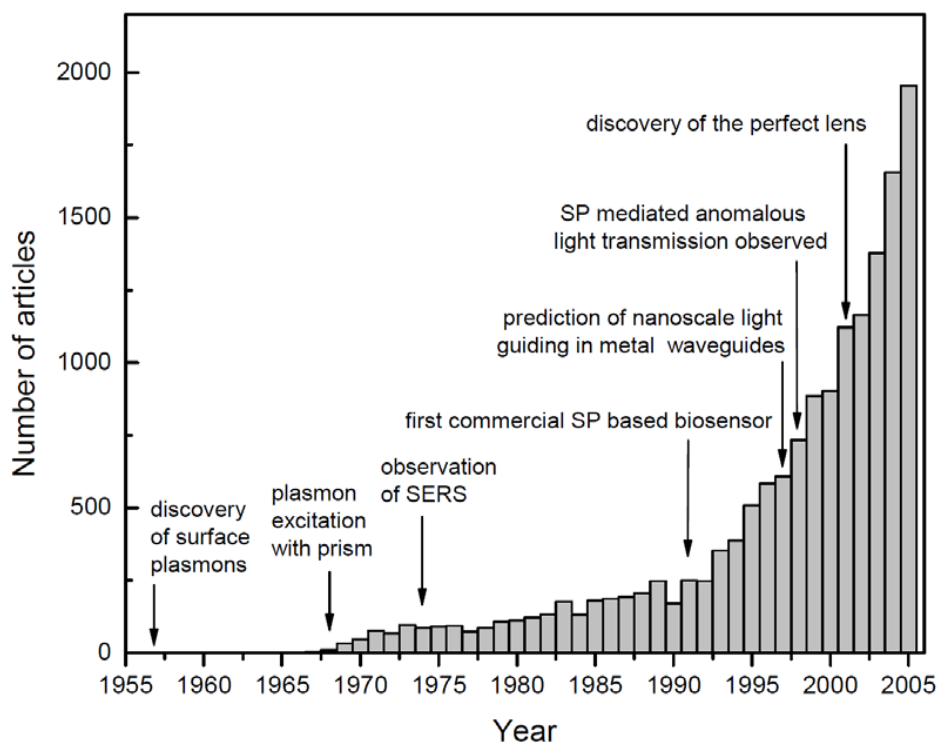
Figure 1-1: Historical milestones in the field of surface plasmons together with the number of citations containing the phrase "Surface Plasmon".[1]

The optical activity of such "plasmonic materials" is under investigation using multiple spectroscopy methods for the material itself as well as when the material is functionalized at its surface by a monolayer of molecules. The connection with the problematic of molecular orientation is of particular interest since the shape of the metallic particle can alter the orientation and the properties of molecules located in its vicinity. Anisotropic metallic structures can be used to induce an anisotropic distribution of molecules adsorbed at their surface and can potentially display new properties. In other terms, the ability to control shapes of metallic structures at the nanoscale opens a variety of hybrid applications to further control chemical, structural and orientational properties of molecules at the single molecule level. Such applications could lead to application in molecular electronics such as a molecular junction[27] or molecular transistor.[28]

In this context, optical techniques are critical for probing these nanoscale materials as well as to evaluate the effect on molecular orientation. The scope of this thesis was to develop tools to i)

access anisotropy of molecular systems, and ii) probe the second-order nonlinearities of metamaterials made of gold nanostructures with anisotropic shapes.

More specifically the thesis is organized as follows:

In **Chapter 2**, we have summarized the main experimental procedures and setups used in this thesis. We first report on the development of polarization modulation spectroscopy developed in our laboratory to investigate dynamically the orientation of molecules that undergo specific molecular orientation when irradiated by a polarized light. The setup has been modified to measure the molecular orientation of azobenzene-containing glass thin films dynamically with in-situ irradiation of the samples. The fundamental principles of plasmonics are then explained by considering the complex dielectric function of metals. The modeling of the electric field in the vicinity of the metal nanostructures organized in arrays provides essential information regarding the localization of the EM field and to define its relationship with the incident polarization of the incoming light. We provide here the basis of Finite-Difference Time-Domain calculations used in this study. Last, a brief introduction of second-order nonlinear optical processes is provided with a focus on second harmonic generation technique developed and used in this thesis.

In **Chapter 3**, we report on the photoinduced vibrational linear dichroism in azobenzene-containing molecular glasses. We focus on the use of the polarization modulation technique to access dynamically the rate constants associated with the dynamics of each vibrational modes of a series of azobenzene-containing glasses. This work has been published in Langmuir[29] and was performed within a multidisciplinary environment involving Western University and Université de Nantes (France). In this project, I was in charge of the development of the experimental setup, its calibration and the data treatment of the collected data. The first author (Dr. Kristen Snell) was in charge of the chemical synthesis of an original series of triphenylamine compounds substituted with azobenzene core.

In **Chapter 4**, the anisotropy of metastructures composed of gold nanoprisms organized in a three-fold symmetry was investigated using second-harmonic generation. I was the first author of this work published in Phys. Chem. Chem. Phys., that was enabled by a collaboration between Western and Ecole Normale Supérieure (Paris). Dr. Joseph Zyss provided us valuable access to a tunable femtosecond laser source combined with an optical microscope.[30]

From the work reported in Chapter 4, we have built our own SHG microscope with a fixed wavelength femtosecond excitation light (λ=800 nm). The development of the setup is described in **Chapter 5**. The construction of this setup took 1.5 years, and we provide here a comprehensive description of the operating setup. We carefully detail the home-built setup (hardware and software) that offers full control over the input and output polarizations.

The setup introduced in Chapter 5 was used in **Chapters 6 and 7** to investigate selected nanostructures. In Chapter 6, half-coated spheres made of polystyrene were investigated by SHG microscopy. The half-coated spheres have no center of inversion and should show clear evidence of SHG activity. In addition to SHG activity, we also demonstrated that the irradiation of the half coated spheres with a pulsed femtosecond source induced the evaporation of the polystyrene material presumably due to the local field enhancement generated by the curved gold coating. The effect of the functionalization of the resulting gold nanocups with azobenzene molecules is investigated to evaluate if molecules with high charge transfer can further enhance the nonlinear response. In Chapter 7, fractal structures of gold prisms are investigated by SHG microcopy. Here we focused on Sierpinski structures that are investigated by SHG with the goal to evaluate the effect of the order of the fractal's generation and the distribution of hot-spots over the fractal structure.

Finally, the main results of this PhD work are highlighted in Chapter 8 providing some future directions in this field.

1.1 References

(1) Brongersma, M. L.; Kik, P. G. *Surface plasmon nanophotonics*; Springer: Dordrecht, 2007.

(2) Engheta, N. *Science.* **2007**, *317*, 1698-1702.

(3) Ebbesen, T. W.; Lezec, H. J.; Ghaemi, H.; Thio, T.; Wolff, P. *Nature.* **1998**, *391*, 667-669.

(4) Park, S.; Won Hahn, J. *Opt. Express.* **2009**, *17*, 20203-20210.

(5) Mansuripur, M.; Zakharian, A. R.; Lesuffleur, A.; Oh, S. H.; Jones, R. J.; Lindquist, N. C.; Im, H.; Kobyakov, A.; Moloney, J. V. *Opt. Express.* **2009**, *17*, 14001-14014.

(6) Li, X. P.; Lan, T. H.; Tien, C. H.; Gu, M. *Nat. Commun.* **2012**, *3*, 998.

(7) Guo, Y. G.; Hu, J. S.; Wan, L. J. *Adv. Mater.* **2008**, *20*, 4384-4384.

(8) Zijlstra, P.; Chon, J. W. M.; Gu, M. *Nature.* **2009**, *459*, 410-413.

(9) Large, N.; Aizpurua, J.; Lin, V. K.; Teo, S. L.; Marty, R.; Tripathy, S.; Mlayah, A. *Opt. Express.* **2011**, *19*, 5587-5595.

(10) El-Sayed, I. H.; Huang, X. H.; El-Sayed, M. A. *Nano Lett.* **2005**, *5*, 829-834.

(11) Loo, C.; Hirsch, L.; Lee, M.-H.; Chang, E.; West, J.; Halas, N.; Drezek, R. *Opt. Lett.* **2005**, *30*, 1012-1014.

(12) Gobin, A. M.; Lee, M. H.; Halas, N. J.; James, W. D.; Drezek, R. A.; West, J. L. *Nano Lett.* **2007**, *7*, 1929-1934.

(13) Halas, N. J.; Lal, S.; Chang, W.-S.; Link, S.; Nordlander, P. *Chem. Rev.* **2011**, *111*, 3913-3961.

(14) Prodan, E.; Radloff, C.; Halas, N.; Nordlander, P. *Science.* **2003**, *302*, 419-422.

(15) Ko, K. D.; Kumar, A.; Fung, K. H.; Ambekar, R.; Liu, G. L.; Fang, N. X.; Toussaint, K. C. *Nano Lett.* **2011**, *11*, 61-65.

(16) Benedetti, A.; Centini, M.; Bertolotti, M.; Sibilia, C. *Opt. Express.* **2011**, *19*, 26752-26767.

(17) Kim, S.; Piao, L.; Han, D.; Kim, B. J.; Chung, T. D. *Adv. Mater.* **2013**, *25*, 2056-2061.

(18) Kim, T.; Jeon, K. S.; Heo, K.; Kim, H. M.; Park, J.; Suh, Y. D.; Hong, S. *Analyst.* **2013**, *138*, 5588-5593.

(19) Chen, C. Y.; Wang, J. Y.; Tsai, F. J.; Lu, Y. C.; Kiang, Y. W.; Yang, C. C. *Opt. Express.* **2009**, *17*, 14186-14198.

(20) Cui, B.; Clime, L.; Li, K.; Veres, T. *Nanotechnology.* **2008**, *19*, 145302.

(21) Moran, A. M.; Sung, J.; Hicks, E. M.; Van Duyne, R. P.; Spears, K. G. *J. Phys. Chem. B.* **2005**, *109*, 4501-4506.

(22) Potara, M.; Baia, M.; Farcau, C.; Astilean, S. *Nanotechnology.* **2012**, *23*, 055501.

(23) Tabatabaei, M.; Najiminaini, M.; Davieau, K.; Kaminska, B.; Singh, M. R.; Carson, J. J.; Lagugné-Labarthet, F. *ACS Photonics.* **2015**, *2*, 752-759.

(24) Kneipp, K.; Wang, Y.; Kneipp, H.; Perelman, L. T.; Itzkan, I.; Dasari, R.; Feld, M. S. *Phys. Rev. Lett.* **1997**, *78*, 1667-1670.

(25) Kazemi-Zanjani, N.; Chen, H.; Goldberg, H. A.; Hunter, G. K.; Grohe, B.; Lagugné-Labarthet, F. *J. Am. Chem. Soc.* **2012**, *134*, 17076-17082.

(26) Schmid, T.; Opilik, L.; Blum, C.; Zenobi, R. *Angew. Chem. Int. Ed.* **2013**, *52*, 5940-5954.

(27) Reed, M. A.; Zhou, C.; Muller, C.; Burgin, T.; Tour, J. *Science.* **1997**, *278*, 252-254.

(28) Ghosh, A. W.; Rakshit, T.; Datta, S. *Nano Lett.* **2004**, *4*, 565-568.

(29) Snell, K. E.; Hou, R.; Ishow, E.; Lagugné-Labarthet, F. *Langmuir.* **2015**, *31*, 7296-7305.

(30) Hou, R.; Shynkar, V.; Lafargue, C.; Kolkowski, R.; Zyss, J.; Lagugné-Labarthet, F. *Phys. Chem. Chem. Phys.* **2016**, *18*, 7956-7965.

Chapter 2

2 Experimental methods: the optical scientist toolbox to address molecular and structural anisotropy.

2.1 Measuring molecular anisotropy using Polarization-Modulation Infrared Spectroscopy(PM-IRLD)

The relationship between the anisotropy of molecular orientation and the macroscopic properties of a material or a surface has drawn particular attention for a variety of applications ranging from dichroic optical elements,[1-3] materials for data storage, [4,5] and stretched or rubbed polymers for molecular alignment.[6] Knowing the orientation of molecules is therefore critical to further tailor materials and improve surface properties of materials such as reactivity, lubrication or adhesion processes.[7] In this thesis, we have measured photoinduced anisotropy of azobenzene-containing materials using polarization modulation vibrational spectroscopy. Specifically, we have used polarization modulation infrared linear dichroism (PM-IRLD) to evaluate the degree of anisotropy of the azobenzene molecular unit when irradiated by a polarized field. The results are reported in Chapter 3. Herein, we report on the development, the signal conditioning, and the calibration methods of the PM-IRLD technique.

For a long time, IR spectroscopy has been a technique of critical importance to study molecules. The basic principle relies on the absorption of electromagnetic radiation by a molecular group that undergoes vibrational motion thus dissipating the absorbed radiation. Each chemical bond provides a unique "fingerprint", which makes IR spectroscopy a useful technique to identify a compound in solid, liquid or gas phases. The selection rule of IR spectroscopy implies that an active mode must show a variation of its dipolar moment associated with the change of the normal coordinates between the two atoms that form a bond. In other terms, $\frac{d\mu_d}{dq} \neq 0$, where $d\mu_d$ stands for the variation of dipole moment μ_d and dq is the variation of the normal coordinate q.

Although the first infrared spectrometer was introduced in 1957 by Perkin Elmer,[8] significant progress in signal treatment were enabled by the parallel development of the computer, and the first commercial Fourier-transform infrared spectrometer (FT-IR) using a Michelson interferometer was commercialized in the early 1970s by Digilab.[9] In FTIR, the radiation of an

infrared source is modulated by the moving mirror of the Michelson interferometer. The collected signal is a superimposition of all the wavelengths used to probe the sample and is called an interferogram. The Fourier transformation implies a calculation from the length domain, which corresponds to the position of the moving mirror, to the reciprocal length domain also referred to as wavenumber. The ratio of the FT-IR single beams from sample and reference yields an absorption spectrum.

In a spectrum provided by an IR spectrometer, the absorbance (Abs.) is generally presented as a function of wavenumber ($\bar{v}$ in cm^{-1}). Each functional group satisfying the selection rule shows a band with a certain intensity and width. The position of that band can be calculated as $\bar{v} = \frac{1}{2\pi c}\sqrt{\frac{k_b}{m_r}}$, where c is the speed of light in vacuum, k_b is the bond strength and m_r is the reduced mass of the atoms forming the diatomic bond. For most of the IR spectrometers, the IR radiation is non-polarized, which implies that the measurement cannot yield information about the molecular orientation of each vibrational mode that is IR active. To go further and obtain the information of the molecular orientation, the IR radiation must to be polarized. Only the chemical bond with a component along the polarized direction will absorb the IR light and will show an absorption band. Reciprocally, if the bond is perpendicular to the impinging polarization, no absorption will be detected since the interaction between polarized field and the bond is minimal. Such polarized spectra can then be used to evaluate the anisotropy and the orientation of molecules with respect to a reference direction.

The difference between polarized absorptions in the two different orthogonal directions is known as linear dichroism (LD). The difference between spectra obtained with circularly co- (left) and contra- (right) polarized sources is referred as circular dichroism. In the infrared range it is referred as vibrational circular dichroism (VCD). VCD measurements are usually conducted to identify chiral compounds, whereas LD is associated with uniaxial anisotropy. One typical example of induced LD is a stretched polymer thin film, in which the molecular level orientation is modified. Such anisotropy can be measured through the use of polarized FT-IR spectroscopy. Two absorption spectra are required to obtain the dichroism: one absorbance with a parallel polarization with respect to the stretching axis ($A_{\parallel}$), and an absorbance perpendicular to the stretching direction ($A_{\perp}$). Then their difference can be calculated and presented as the resulting

linear dichroism, $\Delta A = A_\parallel - A_\perp$. This can be done easily by introducing a IR polarizer between the IR radiation source and the sample. The main drawback of this approach arises from the fact that two spectra are measured independently which does not permit the measurement of dynamic processes. Furthermore, for each of the spectra, a baseline together with purging of carbon dioxide (CO_2) in the sample compartment are necessary thus increasing significantly the acquisition time of the linear dichroism measurement. Such increase of acquisition time is detrimental and limits the interest for sequential polarized spectroscopy. To overcome such drawbacks, Polarization-modulation IR linear dichroism has been introduced in the early 90s.[10,11]

Polarization-modulation infrared linear dichroism, or PM-IRLD, is based on the use of a photoelastic modulator (PEM) that modulates the polarization between two orthogonal states at a high frequency. The detected signal is now doubly modulated: (i) modulated in wavelength by the interferometer (f_1=1 kHz), and (ii) in polarization by the photoelastic modulator (f_2=74 KHz). Since the frequencies of modulation are very distinct, it is possible to filter them using a lock-in amplifier and electronic filter to extract the information related to the linear dichroism. This approach requires a complex setup and necessitates a calibration part to provide quantitative measurements of $\Delta A = A_\parallel - A_\perp$ as explained in the next paragraph.

2.1.1   PM-IRLD setup and calibration

The PM-IRLD setup is based on the use of a photoelastic modulator. This optical component functions based on the photoelastic effect. It is composed of a crystal of Zinc Selenide (ZnSe) compatible with the infrared spectral range, and that becomes birefringent upon application of a stress. The PEM crystal is attached to a piezoelectric transducer that induces a mechanical stress to the crystal in a very precise and controlled way. This stress is calculated to rotate the polarization of light between its two linear and orthogonal directions. Once the stress is released, the polarization is rotated back to its original state. This process can be done delicately, accurately and quickly. The key is therefore to detect the signal between two linearly polarized states of light and calculate the linear dichroism of a given anisotropic molecular system.

The typical setup used in this thesis is shown in Figure 2-1. The IR beam from the interferometer is directed outside the spectrometer and is focused by a barium fluoride (BaF_2) lens onto the sample. The light emerging from the interferometer is polarized with a wire grid polarizer before

entering the photoelastic modulator. The role of the PEM is to switch the polarization of the infrared beam between horizontal and vertical directions at a high frequency (74 kHz). After passing through the sample, the IR signal is focused onto a liquid nitrogen cooled mercury cadmium telluride (MCT) detector. Since the signal is double modulated it must undergo electronic filtering to separate the signals modulated at the frequency of the interferometer (noted Direct Current, DC) and the signal modulated at the frequency of the modulator (noted Alternating Current, AC).
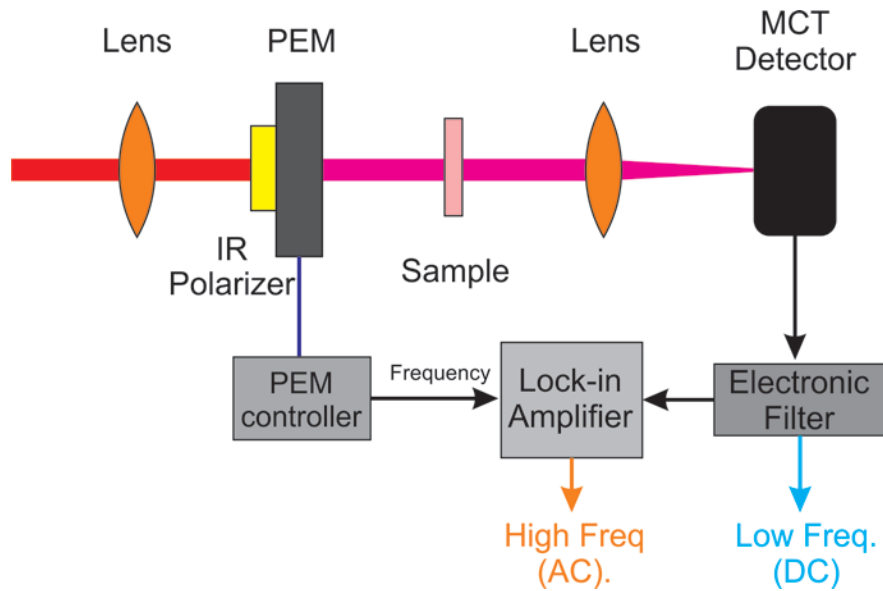
Figure 2-1: PM-IRLD setup developed in this study. PEM: Photoelastic modulator. MCT: Mercury Cadmium Telluride detector.

The detected signal can theoretically be expressed as:[11-13]

$$I_d = \frac{C * I_\parallel^0(\omega_i)}{2} * [(T_\parallel + T_\perp) + (T_\parallel - T_\perp) * J_0(\varphi_0)$$

$$-2 * (T_\parallel - T_\perp) * J_2(\varphi_0) * \cos(2\omega_m t)] \qquad [2\text{-}1]$$

Where I_d is the total intensity obtained by the detector, C is a factor that takes into account the transmission of optical elements and the settings of the electronic filters, $I_\parallel^0(\omega_i)$ is the intensity

of the IR beam after first polarizer. $\cos(2\omega_m t)$ is the modulation term of the PEM, with the modulation frequency $\omega_m = 74$ kHz, $T_\parallel$ and $T_\perp$ are the transmittances of IR radiation along the parallel and perpendicular directions with respect to the first polarizer, J_0 and J_2 are the zeroth and the second-order Bessel functions, which compensate for the deviations in the PEM retardation of light at wavelengths other than the selected retardation wavelength, φ_0 is the optical retardation caused by the PEM and is set to the half-waveplate mode to obtain oscillations between two linear orthogonal polarizations. It can be seen that in Equation 2-1, there are two main terms including one that is not driven by a cosine function and one multiplied by a cosine function that includes the PEM frequency as an argument. The term driven by the cosine function is an oscillating signal, which can be called an "AC" signal and the other term is called a "DC" term. A lock-in amplifier will collect the frequency from the PEM and extract the signal solely modulated by the PEM, while the DC signal will be collected simultaneously in a separate channel. By doing so, the two signals become:

$$I_{DC} = \text{Constant} * [(T_\parallel + T_\perp) + (T_\parallel - T_\perp) * J_0(\varphi_0)] \qquad [2\text{-}2]$$

$$I_{AC} = \text{Constant} * 2 * (T_\parallel - T_\perp) * J_2(\varphi_0) \qquad [2\text{-}3]$$

The ratio of the two signals AC/DC becomes:

$$S = \frac{I_{AC}}{I_{DC}} = \frac{G(T_\parallel - T_\perp)|J_2(\varphi_0)|}{(T_\parallel + T_\perp) + (T_\parallel - T_\perp) * J_0(\varphi_0)} \qquad [2\text{-}4]$$

While G is a constant that depends on the setting of electronic filters and the sensitivity of the lock-in amplifier.
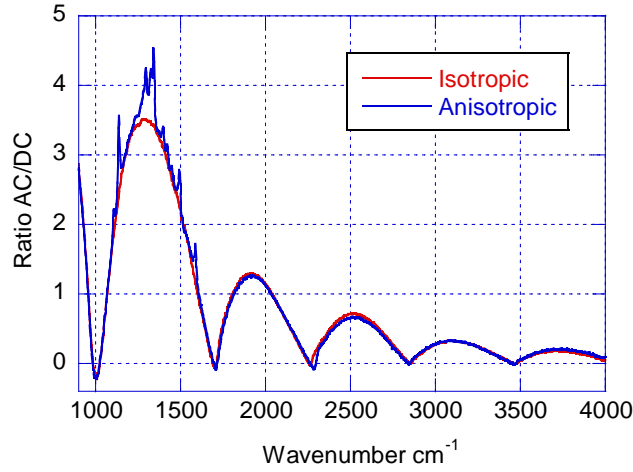
Figure 2-2: Typical non-normalized AC/DC signals collected for an isotropic sample (red) and for an anisotropic thin film (blue).

Two examples are displayed in Figure 2-2. A test anisotropic sample (Signal, in blue) is used to compare with a blank acquisition (Background, in red). The next step is to express the collected signal AC/DC in terms of linear dichroism ΔA.

Equation 2-4 can be further rearranged to:

$$\frac{T_\parallel - T_\perp}{T_\parallel + T_\perp} = \frac{S}{G|J_2| - S*J_0} \qquad [2\text{-}5]$$

The linear dichroism, can be expressed as:

$$\Delta A = A_\parallel - A_\perp = \log\left(\frac{1 - \frac{T_\parallel - T_\perp}{T_\parallel + T_\perp}}{1 + \frac{T_\parallel - T_\perp}{T_\parallel + T_\perp}}\right) \qquad [2\text{-}6]$$

When Equation 2-5 is combined with Equation 2-6, we can also write:

$$\Delta A = \log\left(\frac{C_{Hv} * (\frac{G'}{G} C_{Hh} - S)}{C_{Hh} * (\frac{G'}{G} C_{Hv} + S)}\right) \qquad [2\text{-}7]$$

with:
$$C_{Hv} = \frac{G'|J_2|}{1 - J_0}, \quad C_{Hh} = \frac{G'|J_2|}{1 + J_0} \qquad [2\text{-}8]$$

Here C_{Hv} or C_{Hh} are the calibration spectra collected with a polarizer (also referred as an analyzer) placed in the v (vertical) or h (horizontal) directions with respect to the input polarization, G and G' are the sensitivity of the lock-in amplifier. This second polarizer is used solely to obtain the calibration spectra C_{Hv} or C_{Hh} that are necessary to obtain ΔA. The letter H indicated by the first subscript in C_{Hv} ,C_{Hh} is the orientation of the first polarizer in front of the PEM. The orientation of this polarizer is never altered and is kept to H (horizontal). The resulting calibration curves are shown in Figure 2-3.
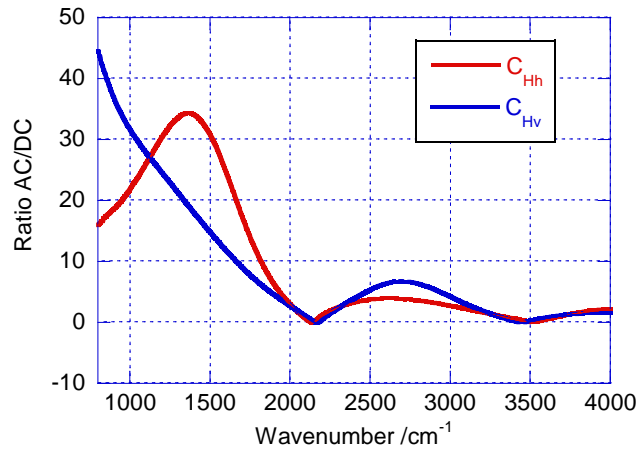
Figure 2-3: C_{Hv} and C_{Hh} calibration curves measured by PM-IRLD with a polarizer placed in the H position before the PEM and with an analyzer placed in the h or v position in lieu of the sample.

In summary, knowing C_{Hv} and C_{Hh}, the gain parameters G and G' together with the experimental raw signal S can be used to determine the absolute linear dichroism of a given sample. This approach may appear to be also time consuming compared to two independent polarized measurements. Yet, PM-IRLD has significant advantages

First, the calibration curves must be done a single time and re-used for multiple samples or for dynamic measurements.

Second, the measurement is differential, i.e. the result of Equation 2-7 provides directly the value of ΔA in a single measurement. The signal to noise ratio is much better than for the two polarizer method, and ΔA can be measured with a precision better than 10^{-4}-10^{-5} which allows one to

probe IR modes with smaller intensities. The typical time resolution for dynamical measurements will be of about 1 PM-IRLD spectra per minute.

Third, the setup is outside the spectrometer without any enclosure. Yet, it is insensitive to the isotropic absorption of water and CO_2 in the air. Water and carbon dioxide gases absorb linearly polarized light the same way for horizontal or vertical polarization since gases are isotropic. Therefore their difference is null and PM-IRLD can therefore be done without any purging step, which would be impossible for separate measurements.

Typical measurement of an anisotropic material is shown in the Figure 2-4. We compare here the two methods of acquisition, i.e. sequential and using PM-IRLD. The quality of the PM-IRLD spectra (red) shows less noise in particular in the region where water absorbs (1396 - 1594 cm^{-1}).
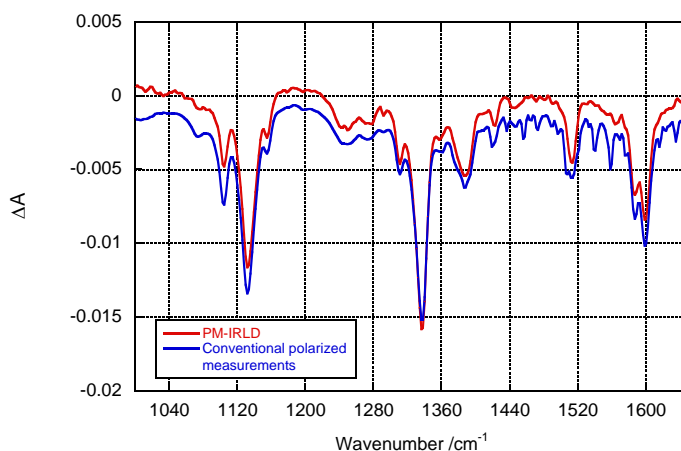
Figure 2-4: Comparison of IRLD spectra obtained using sequential and PM-IRLD methods. The PM-IRLD spectra show significantly less noise in the region where there is absorption due to water. Such parasitic absorption is much more difficult to observe using conventional linear dichroism which needs two separate spectra with two baseline spectras measured independently.

2.2 Surface plasmon and localized surface plasmon resonance

The free conduction electrons of a conductor metal undergo oscillation when subject to an external driving field such as it is the case for an electromagnetic field. This interaction causes a displacement of the electron, which makes the electrons out-of-phase with respect to the positively charged lattice in metal. Like any oscillation, these will occur at defined frequencies coined plasmon frequencies and plasmon resonances. The displacement law can be described as a function of time as $r(t) = r_0 e^{-i\omega t}$, with ω being the angular frequency of the driving external field. The generated dipole moment $\boldsymbol{\mu_{dp}}$ for one conduction electron can be defined as $\boldsymbol{\mu_{dp}} = q_e r(t)$, and its macroscopic polarization is defined as $\boldsymbol{P} = n_e \boldsymbol{\mu_{dp}} = n_e q_e r_0 e^{-i\omega t}$, where q_e represents the electron charge and n_e denotes the number of electrons per unit volume. This oscillation will be enhanced only at the resonance frequency, which can be defined as:[14]

$$\omega = \frac{1}{2\pi} \sqrt{\frac{n_e q_e^2}{m_e \varepsilon_0}}. \qquad \text{[2-9]}$$

with ε_0 as the dielectric constant and m_e being the mass of an electron. However, at the interface between the metal surface and a dielectric material like glass or air, plasmons are confined at the interface and are referred as surface plasmons. Higher incidence angles of incoming irradiation favor a more efficient coupling with metal surface.[14] As illustrated in Figure 2-5, surface plasmons appear as a combination of an electromagnetic wave and surface charges.[15] A transverse magnetic field which is parallel to the interface will be induced at the metal surface. Meanwhile, an electric field that has a perpendicular component with respect to the metal surface will also be induced. This electric field is localized on the surface, and its magnitude will decay exponentially when going away from the metal surface.
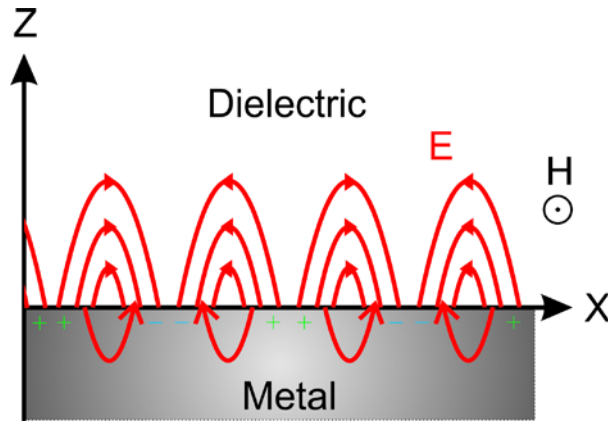
Figure 2-5: Illustration of propagating surface plasmon at the interface between metal surface and a dielectric material.

In order to exhibit a surface plasmon, the complex dielectric constant of the metal requires a positive imaginary part and a negative real part. Noble metals have such properties as well as conductors, such as graphene.[16,17] By treating the microscopic behavior of electrons classically, the electrons can be considered as bouncing off immobile ions. The Drude model is generally used to calculate the dielectric function of metals. The real and imaginary part of the dielectric constant as a function of the wavelength are shown for Au, Ag, Cu and Al in Figure 2-6.[18] Gold and silver are commonly used for exciting surface plasmon using the UV-visible region due to their complex dielectric constants. In Figure 2-6a, it appears that the imaginary part of the dielectric constant for silver and gold are very close but the small differences will result in a significant difference in plasmonic properties of these two metals such as the wavelength of their optical resonances.

To characterize the propagation of the surface plasmon, two wavevectors must be considered: k_{sp} describes the dispersion along the interface, and k_z is for dispersion normal to the interface:[15]

$$k_{sp} = \frac{2\pi}{\lambda} \sqrt{\frac{\varepsilon_d \varepsilon_m}{\varepsilon_d + \varepsilon_m}}$$ [2-10]

$$\left(k_z^{d,m}\right)^2 = \varepsilon_{d,m}\left(\frac{2\pi}{\lambda}\right)^2 - k^2{}_{sp}$$ [2-11]

Here λ stands for the wavelength of the light, ε_d and ε_m are the dielectric constants of the dielectric and metal, respectively.[18] For the metal, the complex dielectric constant can be expressed as $\varepsilon_m = Re(\varepsilon_m) + Im(\varepsilon_m)$. According to Equation 2-11, ε_d is a real function, and the $\mathbf{k_z}$ will remain a complex function.
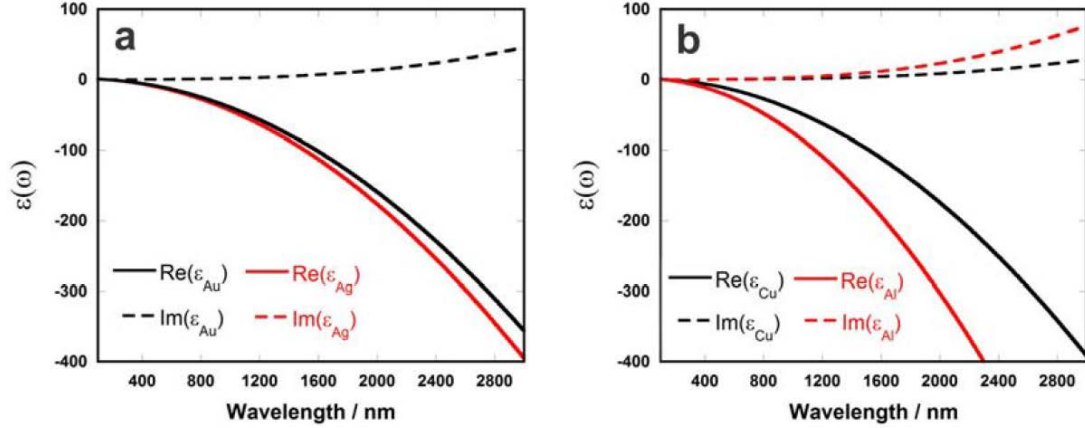
Figure 2-6: Complex dielectric dispersion functions for (a) gold and silver (b) copper and aluminum using the Drude model.

The dispersion normal to the interface, $\mathbf{k_z}^{d,m}$ indicates that the decay of the plasmon field into the dielectric medium and the metal are different. Due to the screening effect of free charges[19] and the metal skin depth[16], the decay length into the metal is smaller than that in dielectric medium, which is in the order of half of the excitation wavelength. The distance along the interface over which the surface plasmon gets dissipated due to damping of electron oscillation, can be defined as the propagation length. Predicted by the Drude model, the propagating length can be plotted in Figure 2-7, as well as the dispersion of the plasmon wavevector. The mismatch of momentum can be observed between the surface plasmon (solid line) and free-space photons (dotted lines), for gold-air (a), silver-air (b), copper-air (c) and aluminum-air (d) interfaces.
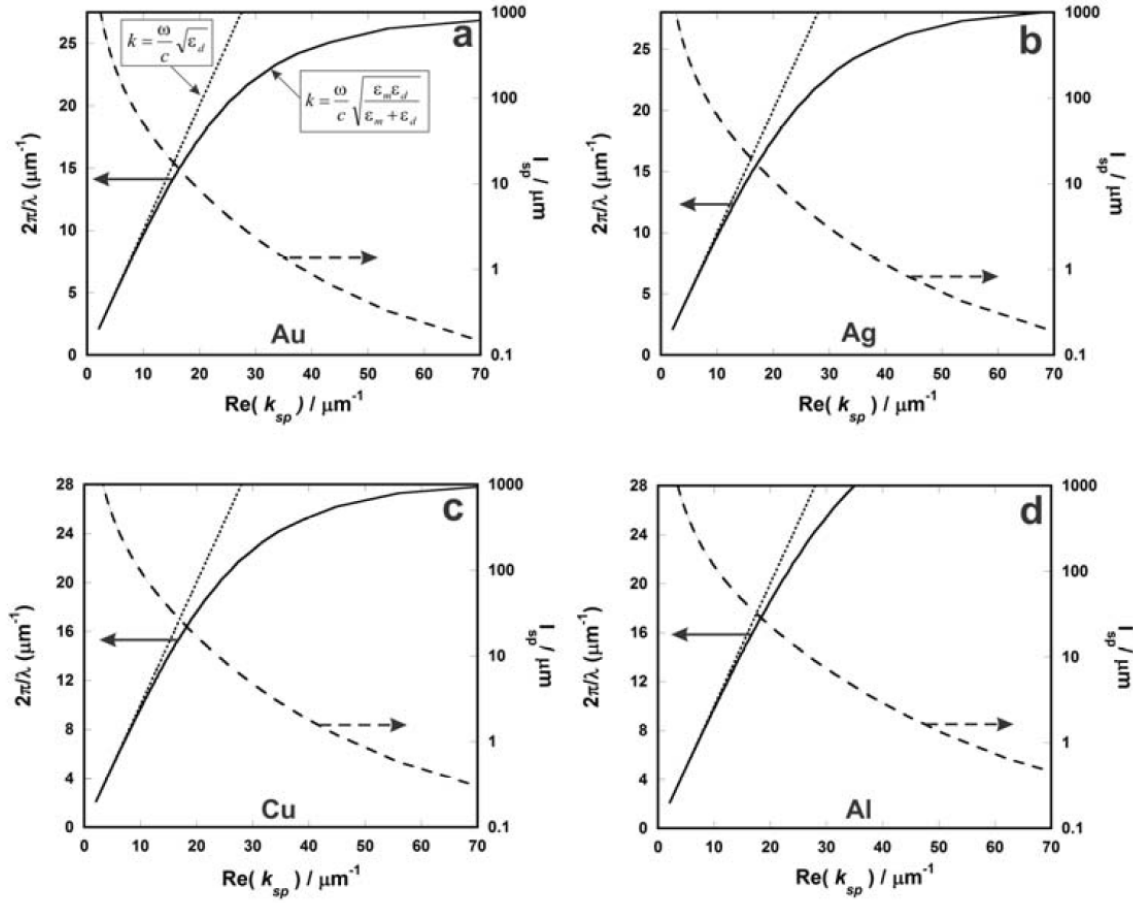
Figure 2-7: Dispersion relation (solid line) and the propagating length (dashed line) of a surface plasmon on (a) gold-air (b) silver-air (c) copper-air and (d) aluminum-air interface according to the Drude model. The propagation of light in free space is shown by dotted lines in each case.

The propagation length as l_{sp} in Figure 2-7 can be expressed by the following equation:[19]

$$l_{sp} = \frac{1}{2 \operatorname{Im}(k_{sp})} = \frac{2}{[\operatorname{Re}(k_{sp})]^3} \times \frac{[2\pi \operatorname{Re}(\varepsilon_m)]^2}{\lambda \operatorname{Im}(\varepsilon_m)} \qquad [2\text{-}12]$$

According to Figure 2-7 and Equation 2-12, the surface plasmon is less confined, decouples easily, and becomes a freely propagating EM wave, while $\operatorname{Re}(k_{sp})$ decreases. On the other hand, the localized surface plasmon and the decrease of propagation length would require an increase in $\operatorname{Re}(k_{sp})$.[19]

When the confinement of the surface plasmon occurs in the vicinity of a metallic nanostructure what has dimensions similar to the wavelength of the excited light, the surface plasmon is localized within the nanostructure and is coined "localized surface plasmon resonance".[14] In a nanostructure, collective oscillation will be excited by incident an EM field. The free electrons in metal will experience a change in momentum. The oscillation will cause the charges to accumulate in specific regions of the nanostructure. In addition, the coupling between two nearby nanoparticles will also enhance the electric field locally. This localized effect can be modeled by a Finite-difference time-domain method that allows quantifying localization of the field, evaluating possible enhancement of the electromagnetic field by the structure and provide wavelength of the resonance. Figure 2-8 shows an example of the localized surface plasmon resonance generated within gaps between gold nanotriangles.[20] In this example, the confinement of the electromagnetic field is expected to occur at the sharp apices of the triangles for a specific input polarization. It clearly shows that localized surface plasmon are also drastically anisotropic and depend not only on the chemical nature of the metal but also on its shape.
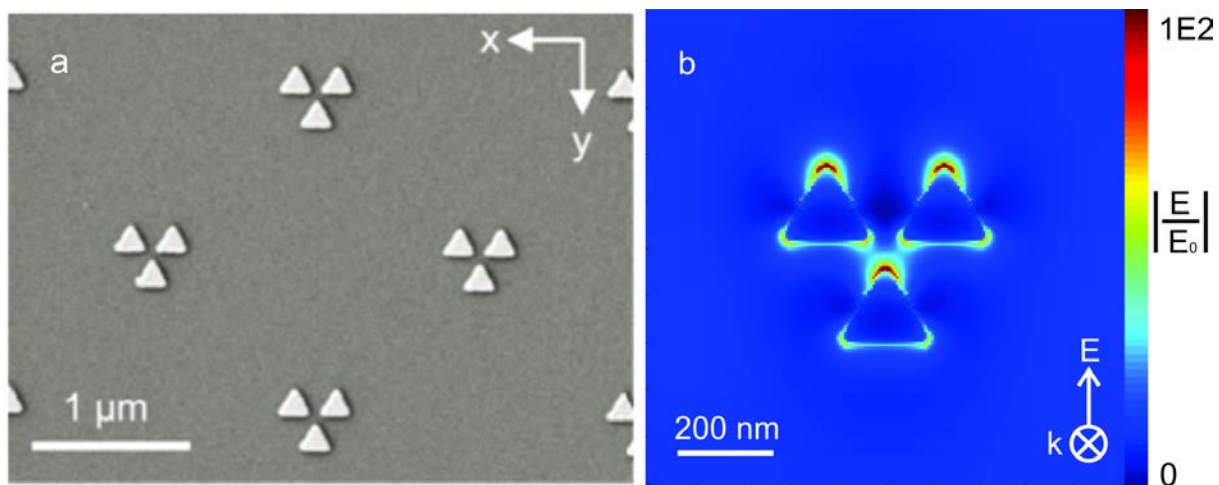
Figure 2-8: Illustration of localized surface plasmon in metal nanostructures (a) SEM image of arrays of gold nanotriangles fabricated by electron beam lithography over the glass surface (b) FDTD simulation of a single set of three triangles showing the confinement of the electric field at the surface of the nanostructure and inside the gaps between the neighboring triangles for an excitation polarized along the y direction.

As shown in Figure 2-8, sharp features of metallic structures appear to strongly enhance the electric field. In the figure above the ratio of E/E_0 quantity is around 100. This means that the local electric field component is expected to be 100 times the electric field of the incoming light. However to reach such values, the incident electromagnetic field must be in resonance with the extinction of the metallic structure. To study how well the metallic nanostructure is interacting with the incident EM wave, the extinction spectrum can be measured using different methods. For example, for a spherical particle, the Mie's solution to Maxwell's equations in the scattering and absorption of light can be utilized for characterization of LSPR.[21] In Mie's theory, for small spherical particles with d<<λ, the scattering (σ_{sca}), extinction (σ_{ext}) and absorption (σ_{abs}) can be expressed as:[14,17,22,23]

$$\sigma_{ext} = \frac{18\pi \varepsilon_d^{3/2} V}{\lambda^4} \frac{\text{Im}(\varepsilon_m)}{[\text{Re}(\varepsilon_m)\chi \varepsilon_d]^2 + [\text{Im}(\varepsilon_m)]^2} \qquad \text{[2-13]}$$

$$\sigma_{sca} = \frac{32\pi^4 \varepsilon_d^2 V^2}{\lambda^4} \frac{[\text{Re}(\varepsilon_m) - \varepsilon_d]^2 + [\text{Im}(\varepsilon_m)]^2}{[\text{Re}(\varepsilon_m)\chi \varepsilon_d]^2 + [\text{Im}(\varepsilon_m)]^2} \qquad \text{[2-14]}$$

$$\sigma_{abs} = \sigma_{ext} - \sigma_{sca} \qquad \text{[2-15]}$$

The optical properties of metal nanospheres are a function of the dielectric constants of both the surrounding environment (air, liquid) and the conductor. In addition, the shape factor (χ) and the volume also have an influence on the extinction and scattering properties. The above equations can also be used to predict the LSPR response as a function of the incident wavelength. This theory can be used to model a selected structure and adjust the geometry, shape and inter-particle distance of a metallic structure to tune the plasmon resonance to a particular spectral range.[23,24]

2.3 Modeling the electromagnetic field with Finite-Difference Time-Domain (FDTD) methods.

In order to numerically describe the interaction between the electromagnetic field and nanostructure, finite-difference time-domain method was used. In this method, Maxwell's equations are discretized in time and space. Maxwell's equations describe the electric and

magnetic field in a medium, by considering two vector fields: the electric field $\boldsymbol{E}$ and the magnetic field $\boldsymbol{B}$. The equations can be expressed as a series of differential equations:

$$\nabla \cdot \boldsymbol{E} = \frac{\rho}{\varepsilon_0} \qquad\qquad \nabla \cdot \boldsymbol{B} = 0$$

$$\nabla \times \boldsymbol{E} = -\frac{\partial \boldsymbol{B}}{\partial t} \qquad \nabla \times \boldsymbol{B} = \mu_0 (\boldsymbol{J} + \varepsilon_0 \frac{\partial \boldsymbol{E}}{\partial t}) \qquad\qquad [2\text{-}16]$$

Where ρ and $\boldsymbol{J}$ stand for the charge and current density, respectively, while ε_0 and μ_0 are permittivity and permeability of free space.

If we divide the space into grids (Yee's cell,[25] Figure 2-9), so that each grid point of the space can be expressed as $(i, j, k) = (i\Delta x, j\Delta y, k\Delta z)$. Here, Δx, Δy and Δz represent the size of the grid in a Cartesian coordinate system. For any function of space and time, we put $F(i\Delta x, j\Delta y, k\Delta z, n\Delta t) = F^n(i, j, k)$ to describe the electric and magnetic fields in the (i, j, k) Yee's cell at time $n\Delta t$. To find out the relationship between neighboring grid or time frame, these Maxwell's equations can be rearranged in their transverse electric and transverse magnetic components:[25]

For transverse electric (TE) waves:

$$H_z^{n+\frac{1}{2}}\left(i + \frac{1}{2}, j + \frac{1}{2}\right) = H_z^{n-\frac{1}{2}}\left(i + \frac{1}{2}, j + \frac{1}{2}\right)$$

$$-\frac{1}{Z}\frac{\Delta\tau}{\Delta x}[E_y^n\left(i + 1, j + \frac{1}{2}\right) - E_y^n\left(i, j + \frac{1}{2}\right)]$$

$$+\frac{1}{Z}\frac{\Delta\tau}{\Delta y}[E_x^n\left(i + \frac{1}{2}, j + 1\right) - E_x^n\left(i + \frac{1}{2}, j\right)] \qquad\qquad [2\text{-}17]$$

$$E_x^{n+1}\left(i + \frac{1}{2}, j + \frac{1}{2}\right) = E_x^n\left(i + \frac{1}{2}, j\right)$$

$$+Z\frac{\Delta\tau}{\Delta y}[H_z^{n+1/2}\left(i + \frac{1}{2}, j + \frac{1}{2}\right) - H_z^{n+1/2}\left(i + \frac{1}{2}, j - \frac{1}{2}\right)] \qquad\qquad [2\text{-}18]$$

$$E_y^{n+1}\left(i, j + \frac{1}{2}\right) = -Z\frac{\Delta\tau}{\Delta x}[H_z^{n+1/2}\left(i + \frac{1}{2}, j + \frac{1}{2}\right) - H_z^{n+1/2}\left(i - \frac{1}{2}, j + \frac{1}{2}\right) \qquad [2\text{-}19]$$

For transverse magnetic (TM) waves:

$$E_z^{n+\frac{1}{2}}(i,j) = E_z^n(i,j)$$

$$+z\frac{\Delta\tau}{\Delta x}[H_y^{n+1/2}\left(i++\frac{1}{2},j\right) - H_y^{n+1/2}\left(i-\frac{1}{2},j\right)]$$

$$-Z\frac{\Delta\tau}{\Delta y}[H_x^{n+1/2}\left(i,j+\frac{1}{2}\right) - H_x^{n+1/2}\left(i,j-\frac{1}{2}\right)] \qquad [2\text{-}20]$$

$$H_x^{n+1/2}\left(i,j+\frac{1}{2}\right) = H_x^{n-1/2}\left(i,j+\frac{1}{2}\right)$$

$$-\frac{1}{Z}\frac{\Delta\tau}{\Delta y}[E_z^n(i,j+1) - E_z^n(i,j)] \qquad [2\text{-}21]$$

$$H_y^{n+1/2}\left(i+\frac{1}{2},j\right) = H_x^{n-1/2}\left(i+\frac{1}{2},j\right) + \frac{1}{Z}\frac{\Delta\tau}{\Delta x}[E_z^n(i+1,j) - E_z^n(i,j) \qquad [2\text{-}22]$$

With:

$$\tau = \sqrt{\frac{1}{\mu_0\varepsilon_0}}t \qquad\qquad Z = \sqrt{\frac{\mu_0}{\varepsilon_0}} = 376.7 \qquad [2\text{-}23]$$

Through solving Equations 2-17 to 2-23 the FDTD provides time-domain information, offering insight into electrodynamics of the system.[26] In FDTD calculation, the EM field and structures are defined as discrete meshes called Yee cells (Figure 2-9).
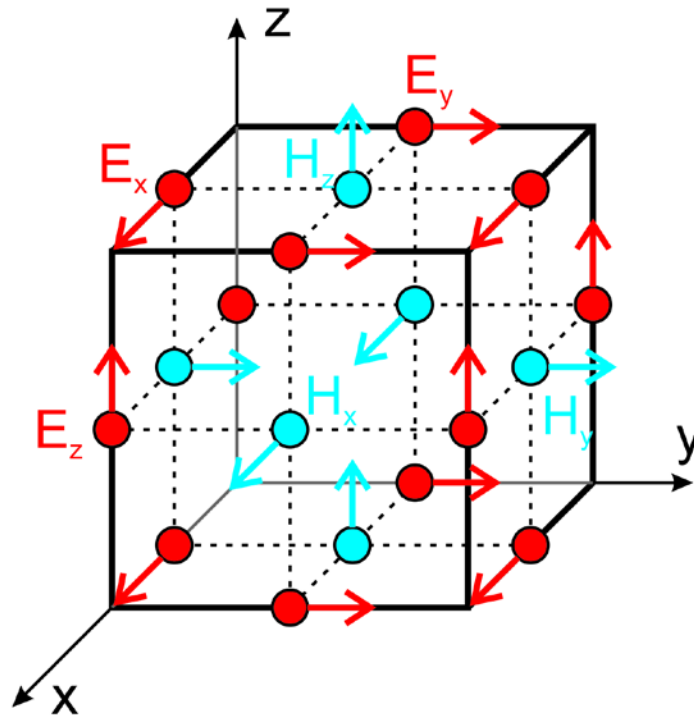
Figure 2-9: Illustration of standard Cartesian Yee cell used for FDTD. The electric (E_x, E_y, E_z) and magnetic (H_x, H_y, H_z) field components are distributed about this cell. The electric field components originate from the edges of the cube and the magnetic field components come out of the faces.

Figure 2-9 is an illustration of standard cartesian Yee cell used for FDTD. The electric (E_x, E_y, E_z) and magnetic (H_x, H_y, H_z) field components are distributed on the unit cell. The electric field components originate from the edges of the cubic lattice, while the magnetic field originate from the faces of the lattice. The electric/magnetic fields are calculated by time frame, for each Yee's cell. By choosing the size of Yee's cell, the balance between simulation time/memory requirements and precision of the simulation can be found.

2.4 Fundamentals of nonlinear optics

In a medium where only the linear susceptibility is considered, the resulting polarizability is defined as $\boldsymbol{P} = \varepsilon_0 \chi_e \boldsymbol{E}$ where ε_0 is the vacuum permittivity, χ_e the susceptibility and $\mathbf{E}$ the incident electromagnetic field.

In nonlinear optics (NLO), the higher order nonlinear terms must be considered. The use of an intense laser pulse makes these terms significant and measurable. The polarizability can be written as:

$$\boldsymbol{P} = \varepsilon_0 \chi_e \boldsymbol{E} + \varepsilon_0 \chi^{(2)} \boldsymbol{E}^2 + \varepsilon_0 \chi^{(3)} \boldsymbol{E}^3 + \cdots\cdots + \varepsilon_0 \chi^{(i)} \boldsymbol{E}^i \qquad [2\text{-}24]$$

In this equation, the lowest nonlinear term is the second order nonlinear term with respect to $\chi^{(2)}$ which is the second order nonlinear susceptibility:

$$\boldsymbol{P} = \varepsilon_0 \chi^{(2)} \boldsymbol{E}^2 \qquad [2\text{-}25]$$

Here, assuming that the electromagnetic excitation wave is a combination of two waves with distinct frequencies ω_1 and ω_2 , the incident EM field can be written as :

$$\boldsymbol{E} = \boldsymbol{E}_1 cos(\omega_1 t - \boldsymbol{k}_1 \boldsymbol{z}) + \boldsymbol{E}_2 cos(\omega_2 t - \boldsymbol{k}_2 \boldsymbol{z}) \qquad [2\text{-}26]$$

If we substitute Equation 2-26 into Equation 2-25, the $\mathbf{E}^2$ term becomes:

$$\varepsilon_0 \chi^{(2)} \boldsymbol{E}^2 = \varepsilon_0 \chi^{(2)} * [\boldsymbol{E}_1^2 cos^2(\omega_1 t - \boldsymbol{k}_1 \boldsymbol{z}) + \boldsymbol{E}_2^2 cos^2(\omega_2 t - \boldsymbol{k}_2 \boldsymbol{z}) + 2\boldsymbol{E}_1 \boldsymbol{E}_2 cos(\omega_1 t - \boldsymbol{k}_1 \boldsymbol{z}) cos(\omega_2 t - \boldsymbol{k}_2 \boldsymbol{z})] \qquad [2\text{-}27]$$

Equation 2-27 show that three terms can be differentiated:

$$P^{(0)} = {}^1\!/_2\, \varepsilon_0 \chi^{(2)}(\boldsymbol{E}_1^2 + \boldsymbol{E}_2^2) \qquad [2\text{-}28]$$

$$P^{(2\omega_i)} = {}^1\!/_2\, \varepsilon_0 \chi^{(2)} \boldsymbol{E}_i^2 cos[2(\omega_i t - \boldsymbol{k}_i \boldsymbol{z})], \text{ where } i = 1,2 \qquad [2\text{-}29]$$

$$P^{(\omega_1 + \omega_2)} = {}^1\!/_2\, \varepsilon_0 \chi^{(2)} \boldsymbol{E}_1 \boldsymbol{E}_2 cos[(\omega_1 t \pm \boldsymbol{k}_1 \boldsymbol{z}) + (\omega_2 t \pm \boldsymbol{k}_2 \boldsymbol{z})] \qquad [2\text{-}30]$$

The above three equations describe distinct second-order nonlinear phenomena: optical rectification (Equation 2-28), second harmonic generation (Equation 2-29) and sum/difference frequency generation (Equation 2-30). Here, in this thesis we will focus on second harmonic generation that occurs when two incident photons with the same frequency recombine to yield a new photon with twice the incident frequency (half the incident wavelength). In second-order nonlinear optical processes, the input optical field interacts with a medium. A second harmonic

polarization **P** will be induced. The intensity of this second harmonic will be proportional to the square of the input field:

$$\boldsymbol{E}_{2\omega} \propto \chi_D{}^{(2)} \boldsymbol{E}_\omega{}^2 \qquad \text{[2-31]}$$

where $\chi_D{}^{(2)}$ represents the dipole contribution to the second-order nonlinear susceptibility tensor for the medium. If the medium is symmetric, and this process is assumed to exist in the bulk, $\chi_D{}^{(2)}$ should be invariant upon the inversion operation. However, both $\boldsymbol{E}_{2\omega}$ and $\boldsymbol{E}_\omega$ will change sign under inversion since they are vectors. Thus, the only possibility is that $\chi_D{}^{(2)} = 0$, or vanishes in a inversion symmetry medium, under this dipole approximation. At the interface, however the inversion symmetry is necessarily broken, so the $\chi_D{}^{(2)}$ will not vanish. That is the reason SHG is surface sensitive.

The $\chi_D{}^{(2)}$ can also be tuned at the interface, by introducing a layer of adsorbents. The total interface nonlinear susceptibility tensor can be expressed as:

$$\chi_I{}^{(2)} = \chi_B{}^{(2)} + \chi_A{}^{(2)} + \chi_{Int}{}^{(2)}$$

with $\chi_B{}^{(2)}$, $\chi_A{}^{(2)}$ and $\chi_{Int}{}^{(2)}$ denoting contributions from the bare interface, the adsorbed layer, and the interaction between the adsorbed layer and the substrate. The dominant term among the three will depend on the material system. If the molecules or atoms adsorbed are small and the surface is made of metal or semiconductor, $\chi_A{}^{(2)}$ is usually negligible and the main effect is a modification of $\chi_B{}^{(2)}$ by $\chi_{Int}{}^{(2)}$. On the other hand, if the molecules are asymmetric with a large second-order nonlinear polarizability adsorbed on a dielectric substrate, $\chi_A{}^{(2)}$ becomes the dominant term.

To study the second order nonlinear optical effects when introducing a molecule, the molecular hyper-polarizability β_{ijk} is needed. Similar to Equation 2-31, the second order molecular hyper-polarizability β_{ijk} vanishes by symmetry in a molecule with a center of inversion.[27-30]

Last, the symmetry of a metastructure such as a plasmonic substrate with a geometry that does not show any inversion center can also yield SHG activity. This work is extensively detailed in Chapters 4-7.

2.5 References

(1) Redel, E.; Wang, Z.; Walheim, S.; Liu, J.; Gliemann, H.; Wöll, C. *Appl. Phys. Lett.* **2013**, *103*, 091903.

(2) Wang, T.; Li, P.; Hauer, B.; Chigrin, D. N.; Taubner, T. *Nano Lett.* **2013**, *13*, 5051-5055.

(3) Yun, J.-H.; Cho, H.-S.; Bae, K.-B.; Sudhakar, S.; Kang, Y. S.; Lee, J.-S.; Polyakov, A. Y.; Lee, I.-H. *Appl. Phys Express.* **2015**, *8*, 092002.

(4) Choeiprathum, W.; Suvichakorn, A.; Google Patents: 2015.

(5) Ho, M.-S.; Natansohn, A.; Barrett, C.; Rochon, P. *Can. J. Chem.* **1995**, *73*, 1773-1778.

(6) Liang, Y.; Mauran, D.; Prud'Homme, R. E.; Pellerin, C. *Appl. Spectrosc.* **2008**, *62*, 941-947.

(7) Wilson, P. T.; Richter, L. J.; Wallace, W. E.; Briggman, K. A.; Stephenson, J. C. *Chem. Phys. Lett.* **2002**, *363*, 161-168.

(8) Perkin-Elmer. *Clinical Science* **1957**, *16*.

(9) Griffiths, P. R. *Science.* **1983**, *222*, 297-302.

(10) Buffeteau, T.; Lagugné-Labarthet, F.; Pézolet, M.; Sourisseau, C. *Macromolecules.* **1998**, *31*, 7312-7320.

(11) Buffeteau, T.; Pézolet, M. *Appl. Spectrosc.* **1996**, *50*, 948-955.

(12) Buffeteau, T.; Desbat, B.; Pézolet, M.; Turlet, J. *J. Chim. Phys. Phys.- Chim. Biol.* **1993**, *90*, 1467-1489.

(13) Buffeteau, T.; Desbat, B.; Besbes, S.; Nafati, M.; Bokobza, L. *Polymer.* **1994**, *35*, 2538-2541.

(14) Mayer, K. M.; Hafner, J. H. *Chem. Rev.* **2011**, *111*, 3828-3857.

(15) Barnes, W. L.; Dereux, A.; Ebbesen, T. W. *Nature.* **2003**, *424*, 824-830.

(16) Banholzer, M. J.; Millstone, J. E.; Qin, L.; Mirkin, C. A. *Chem. Soc. Rev.* **2008**, *37*, 885-897.

(17) Willets, K. A.; Van Duyne, R. P. *Annu. Rev. Phys. Chem.* **2007**, *58*, 267-297.

(18) Novotny, L.; Cambridge University Press, Cambridge: 2006.

(19) Ebbesen, T. W.; Genet, C.; Bozhevolnyi, S. I. *Phys. Today.* **2008**, *61*, 44.

(20) Hou, R.; Shynkar, V.; Lafargue, C.; Kolkowski, R.; Zyss, J.; Lagugné-Labarthet, F. *PCCP.* **2016**, *18*, 7956-7965.

(21) Mie, G. *Annalen der physik.* **1908**, *330*, 377-445.

(22) Bohren, C. F.; Huffman, D. R. *Absorption and scattering of light by small particles*; John Wiley & Sons, 2008.

(23) Moskovits, M. *J. Raman Spectrosc.* **2005**, *36*, 485-496.

(24) Hohenau, A.; Leitner, A.; Aussenegg, F. R. In *Surface Plasmon Nanophotonics*; Springer: 2007, p 11-25.

(25) Yee, K. S. *IEEE Trans. Antennas Propag.* **1966**, *14*, 302-307.

(26) Galarreta, B. C.; Rupar, I.; Young, A.; Lagugné-Labarthet, F. *J. Phys. Chem. C.* **2011**, *115*, 15318-15323.

(27) Lalama, S. J.; Garito, A. F. *Phys. Rev. A.* **1979**, *20*, 1179.

(28) Oudar, J.-L.; Chemla, D. *J. Chem. Phys.* **1977**, *66*, 2664-2668.

(29) Blanchard-Desce, M.; Runser, C.; Fort, A.; Barzoukas, M.; Lehn, J.-M.; Bloy, V.; Alain, V. *Chem. Phys.* **1995**, *199*, 253-261.

(30) Levine, B. *Chem. Phys. Lett.* **1976**, *37*, 516-520.

Chapter 3

3 Enhanced Rates of Photoinduced Molecular Orientation in a Series of Molecular Glassy Thin Films

Photoinduced orientation in a series of molecular glasses made of small push-pull azo derivatives is dynamically investigated for the first time. Birefringence measurements at 632.8 nm are conducted with a temporal resolution of 100 ms in order to probe the fast rate of the azo orientation induced under polarized light and its temporal stability over several consecutive cycles. In order to better evaluate the influence of the azo chemical substituents and their electronic properties on the orientation of the whole molecule, a series of push-pull azo derivatives involving a triphenylaminoazo core substituted with distinct electron-withdrawing moieties is studied. All resulting thin films are probed using polarization modulation infrared spectroscopy that yields dynamical linear dichroism measurements during a cycle of orientation followed by relaxation. We show here in particular that the orientation rates of small molecule-based azo materials are systematically increased up to a seven-fold factor compared to those of a reference polymer counterpart. For specific compounds, the percentage of remnant orientation is also higher, which makes these materials of great interest and promising alternatives to azobenzene-containing polymers for a variety of applications requiring a fast response and absolute control over the molecular weight.

3.1 Introduction.

Photochromic organic materials are of particular interest for potential applications varying from photoresponsive glasses to active materials in photonic devices, such as diffraction gratings for light coupling, high-speed optical switches, light waveguides and optical data storage.[1-5] Among the organic photochromic materials, azobenzene-containing materials are well known to undergo selective, reversible and stable *E-Z* isomerization upon irradiation with appropriate wavelengths.[6,7] The low fatigability of the isomerization reaction over more than 10^6 cycles has led to intense activity in the past two decades in the field through the fabrication of a variety of devices encompassing surface relief gratings with linear and nonlinear optical properties,[8-11] mechanical actuators,[12-14] sensors,[15-17] media for optical data-storage,[5,18] and other photonic devices such as waveguides,[19,20] distributed feedback lasers[21,22] and nanoplasmonic assemblies.[23]

Azopolymers present the particular advantage to be easily processed in thin films and to yield a high and stable degree of orientation upon selective irradiation with polarized light.[24] However, key parameters such as the response time, the degree of photoinduced orientation and the remnant orientation can significantly be improved to reach faster dynamics, larger and more stable orientation, thus opening new applications where these parameters are critical such as optical data storage media.[5,25] Up to now, most of the orientation studies have been devoted to side-chain amorphous and liquid-crystalline azopolymers where cooperative side chain effects and entanglement from the polymer backbone prominently rule the dynamics of the molecular rearrangement upon light excitation. To enable a higher level of photoinduced orientation, a variety of optimized molecular structures of low molecular-weight copolymers have been developed by several groups to enhance the cooperative molecular motion between a photoactive unit and a non-photoactive non-absorbing unit[26,27] or between two distinct mesogenic units that serve as antenna for the incident light.[28,29] Levels of birefringence as high as 0.2 were reported in liquid-crystalline polymers enabling a vivid interest for data storage applications, although the molecular orientation rates were too slow for high throughput applications. Entanglement from the polymer backbone is a critical parameter that is presumably responsible for an inhomogeneous distribution of the orientation and relaxation rates of the photoactive units thus slowing down the orientation dynamics of the azo chromophores. Such effects have been investigated at a molecular level using polarization modulation infrared spectroscopy linear dichroism on amorphous, semi-crystalline and liquid-crystalline polymers.[30-32] In these pump-probe experiments, the photoinduced linear dichroism was investigated during cycles of orientation and relaxation. Since PM-IRLD provides a quantitative information on each IR active vibrational mode, it was possible to investigate dynamically the orientation of the individual vibrations. Quantification of the ordering of vibrational modes with defined symmetry could be performed and was used to determine cooperative effects between the side groups of the azopolymers chains. For modes with rather undefined symmetry, PM-IRLD was key to provide clues about their involvements in the molecular orientation process showing in particular that the backbone of the polymer conserves an isotropic conformation while it affects the rate of molecular orientation.

In this context, molecular materials made of small organic molecules offer a very interesting alternative to polymer materials since there is no need of dilution of the photochromes within a
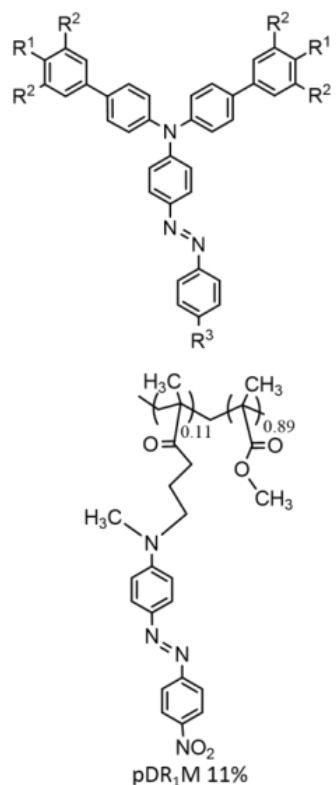
polymer binder to avoid crystallization or aggregation of the molecules.[33] These small molecules can form pristine amorphous glasses and thin films, and, due to the absence of polymer-chain entanglement, faster photo induced dynamics are observed as reported for the fabrication of surface relief gratings.[34-37] Such materials are often based on a bulky electron-donor group such as triphenylamine, diaminobiphenyl or triarylamine have been investigated in a varies of applications such as electroluminescent devices,[38,39] organic electronic memory device[40,41] and optical glasses with nonlinear optical properties.[42]

Herein, we report on the dynamical study of a series of nine push-pull azo derivatives whose structure, based on a triarylaminoazo core, has been substituted with various electron-withdrawing groups to assess the effect of the substituent onto the molecular orientation capability in glassy thin films. The photoinduced birefringence was dynamically measured over several cycles of irradiation and thermal relaxation. To complement the macroscopic response provided by the birefringence measurements, the molecular orientation of the individual chemical groups was dynamically recorded for the nine compounds with PM-IRLD giving a clearer view on the orientation of the triphenylaminoazo molecules. All birefringence and PM-IRLD measurements were compared against thin films of poly[4'-(((2-(methacryloyloxy)ethyl)ethyl)-amino)-4-nitroazobenzene-co-Methyl methacrylate] with DR1M mole fraction of 0.11 and thus referred as pDR1M-11% or more simply pDR1M in this manuscript. This compound is considered as the archetype of push-pull azo dye and subjected to numerous fundamental and applied studies.[10,43-47] The rates of orientation and relaxation, as well as the degree of orientation were systematically determined by fitting the birefringence evolution using bi-exponential laws and compared against those obtained from pDR1M thin films. We show that the rate of orientation in some compounds can be enhanced by a 7-fold factor. The degree of orientation is however smaller than for azopolymers, yet with a higher residual orientation upon relaxation, in particular for the compounds substituted with bulkier groups like carbazolyl ones. These materials with faster response can be valued for a variety of applications where faster switching time is an essential criterion.

3.2 Experimental Methods.

3.2.1   Preparation of thin films.

The solutions were prepared using a 2% solution of the azo compound (Figure 3-1) in chloroform. The solution was filtered using Micropores filters (0.2 μm-large pores) and spin-coated onto glass slides and NaCl plates for birefringence and infrared experiments, respectively. Typical thicknesses varied between 300 to 500 nm and were systematically measured by atomic force microscopy (AFM). The properties of the thin films are reported in Table 3-1 (Page 40).

Compound	R^1	R^2	R^3
tBuNO$_2$	tBu	H	NO$_2$
tBuCN	tBu	H	CN
tBuCO$_2$Me	tBu	H	CO$_2$Me
CF$_3$NO$_2$	H	CF$_3$	NO$_2$
CF$_3$CN	H	CF$_3$	CN
CF$_3$CO$_2$Me	H	CF$_3$	CO$_2$Me
CarbNO$_2$		H	NO$_2$
CarbCN		H	CN
CarbCO$_2$Me		H	CO$_2$Me

Figure 3-1: Series of push-pull triphenylaminoazo derivatives (top-left) and azo polymer pDR1M 11 % (bottom-left).

3.2.2   Birefringence.

The setup is described in Figure 3-2A. The probe beam consisted in a He-Ne laser at 632.8 nm (1 mW) and its incidence was set normal to the sample. The pump beam was set at 532 nm with an irradiance of 80 mW/cm^2 and with an incidence of 15 degrees with respect to the sample normal

direction. A fast photodiode was used to detect the phase shift $\Delta\varphi$ between the two main axes of the film, with a temporal resolution of about 100 ms. The phase shift was calibrated with a Babinet-Soleil compensator and the absolute birefringence was determined knowing the probe wavelength, λ and the thickness, d of the thin films using:

$$\Delta n = n_{//} - n_{\perp} = \frac{2\pi d\,\Delta\varphi}{\lambda} \qquad\qquad [3\text{-}1]$$

where $n_{//}$ and $n_{\perp}$ are the refractive indices in the planes parallel and perpendicular to the pump beam polarization direction, respectively. Experiments were done in triplicates on different films.

3.2.3   Polarization Modulation Infrared Linear Dichroism Spectroscopy.

The setup is described in Figure 3-2B and the underlying principles are detailed in Chapter 2. A mid-IR source from a Fourier-Transform spectrometer is directed outside the spectrometer and modulated between two orthogonal polarization directions noted // and $\perp$ at a frequency of 74 kHz using a photoelastic modulator (Hinds). The signal detected by an MCT-A detector is electronically filtered and amplified using a lock-in amplifier and, after processing, is equal to the dichroic spectrum, namely $\Delta A = A_{//} - A_{\perp}$ where A_i refers to the i-polarized absorbance (parallel or perpendicular). The *in-situ* irradiation of the sample was performed using a 532 nm laser source enabling the recording of photoinduced dichroic spectra during several cycles of orientation followed by relaxation. Dichroism erasure was performed by adding a quarter-waveplate on the beam path. Sixty spectra were recorded for a single measurement yielding a temporal averaged resolution of 1 spectrum/min. Calibration and normalization of the resulting linear dichroism ΔA were done for each spectrum that was integrated over distinct spectral domains corresponding to the different vibrational bands.[48]
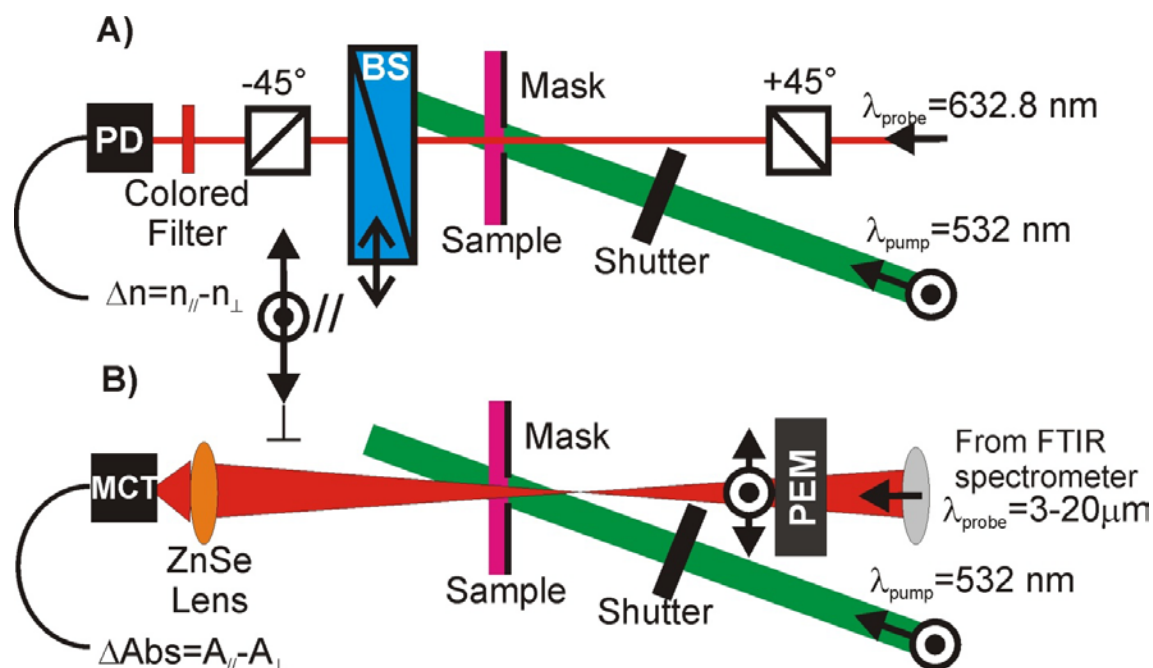
Figure 3-2: (A) Birefringence setup and (B) polarization modulation infrared linear dichroism setup for the study of photoinduced anisotropy in thin films.

3.3 Results and discussion

The syntheses and characterizations of the investigated series of glass-forming push-pull azo derivatives were previously reported.[49] A modular approach was used, leading to the fabrication of nine azo compounds containing various bulky groups (3,5-bis(trifluoromethyl)phenyl (CF_3),4-*tert*-butylphenyl (tBu) and 4-bis*(4-tert*-butyl)carbazolylphenyl (Carb) and electron-withdrawing units such as the NO_2, CN and CO_2Me groups (Figure 3-1). The push-pull structure along the azo core provides a large charge transfer from the amino group in the triarylamine to the electron-accepting group, thereby yielding an electronic transition located in the visible range which is a superposition of π-π* and n-π* transitions. For the present series, the maximum absorption wavelengths of the thin films vary between 450 nm to 500 nm as summarized in Table 3-1. In order to trigger the photoinduced isomerization, resonant light is generally used. In the present study, a 532 nm excitation light that was linearly polarized was used. This excitation wavelength is resonant or pre-resonant with most of the electronic transitions of the push-pull azo compounds. Nevertheless for CF_3CO_2Me, weaker interactions are expected due to the large difference between absorption (445 nm) and excitation (532 nm). Beside the photoisomerization

process that has been thoroughly investigated in toluene solution,[49] a stable angular reorientation of the azo molecules occurs in thin films. This angular hole-burning is a consequence of the molecular reorientation of the azo compounds through a rotation around the N=N bond upon excitation with polarized light.[50,51] Such phenomenon is of particular interest in thin films since it yields large anisotropic properties, which can be probed using polarized light. Here below, we have thus investigated the response of such thin films subjected to irradiation with a polarized light set at 532 nm.

3.3.1 Birefringence measurements during an orientation and a relaxation cycle.

In order to probe the macroscopic response of the azo series under irradiation at 532 nm, birefringence measurements were performed at 632.8 nm for all nine triphenylaminoazo compounds as well as for the reference pDR1M thin film (Fig. 2A-D). The absolute values of the measured birefringence $|\Delta n|$ were shown in Figure 3-3. The dynamics of orientation and relaxation are reported on the same figure for a selected electron-donating group and various electron acceptors. Figure 3-3A-C report the dynamics within a series of azo derivatives containing the same bulky substituents (tBu, CF_3 and Carb, respectively) while Figure 3-3D features the dynamics for the reference pDR1M thin film. All figures are drawn with the same scales, emphasizing that both the maximum birefringence $|\Delta n|_{max}$ upon irradiation and the remnant one $|\Delta n|_{\infty}$ after relaxation are higher for a pDR1M thin film compared to the triphenylamino series.
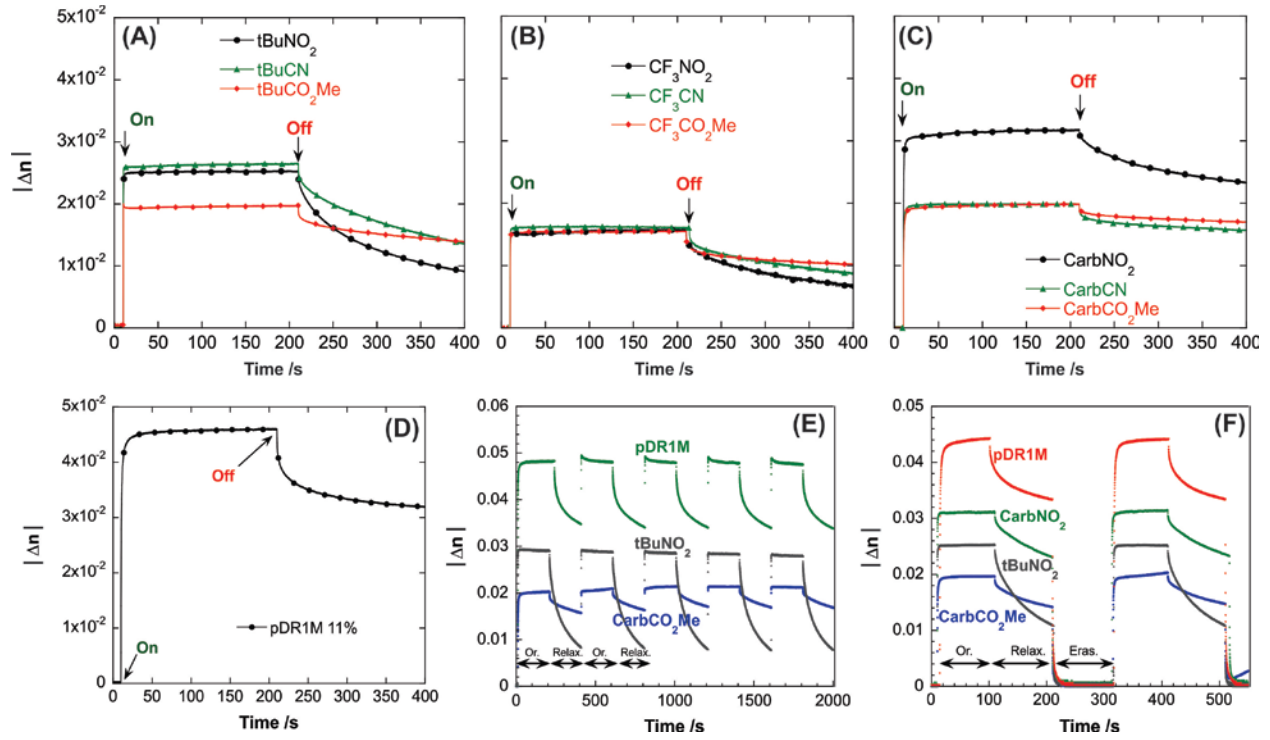
Figure 3-3: Birefringence dynamics during a cycle of orientation (pump on), relaxation (pump off) and erasure for the tBu series (A), CF₃ series (B), Carb series (C) and pDR1M (D) processed as thin films. Cycles of orientation/relaxation for selected azo thin films of tBuNO₂, CarbCO₂Me and pDR1M polymer (E). Cycles of orientation, relaxation, erasure for selected azo thin films of CarbNO₂, tBuNO₂, CarbCO₂Me and pDR1M (F).

In order to extract the rate constants k_i associated with the dynamics of the birefringence measurements during both the orientation and relaxation processes, bi-exponential fitting laws were used as already reported for the photochromic studies in thin films.[35,49,52] The orientation processes are described by Equation 3-2,

$$y_{orientation}(t) = m_1^{or} e^{-k_1^{or}t} + m_2^{or} e^{-k_2^{or}t} + m_3^{or} \qquad [3\text{-}2]$$

while the relaxation is described by Equation 3-3.

$$y_{relaxation.}(t) = m_1^{rel}\left(1 - e^{-k_1^{rel}t}\right) + m_2^{rel}\left(1 - e^{-k_2^{rel}t}\right) + m_3^{rel} \qquad [3\text{-}3]$$

Such bi-exponential models are particularly well adapted to describe the dynamic orientation in azo materials where k_1^{or} and k_1^{rel} are the fast rate constants associated with the E-Z and Z-E isomerization processes respectively, and are convoluted with the mechanical and thermal responses of the matrix. k_2^{or} and k_2^{rel} are the slow rate constants associated with the angular redistribution of the E species at longer time during the orientation and the relaxation processes. In thin films, both $k_1^{or,rel}$ and $k_2^{or,rel}$ depend on the inhomogeneity effects from the matrix. In addition to the rate constants, $m_3^{or,rel}$ is a fitting variable that can be used to appreciate the level of birefringence at the plateau value during the orientation or the remnant birefringence upon relaxation while the values of $m_1^{or,rel}$ and $m_2^{or,rel}$ provide the weight of the fast and slow rate constants during the dynamics.

The fitting parameters for the orientation and relaxation processes associated with the birefringence curves shown in Figure 3-3A-D are reported in Table 3-1 and Table 3-2, for the orientation and relaxation processes, respectively. The maximum level of photoinduced birefringence can be measured for tBuCN and CarbNO$_2$ with $|\Delta n| = 0.0283$ and $|\Delta n| = 0.0317$, respectively. These values have to be compared with $|\Delta n| = 0.0458$ for pDR1M. It is noteworthy that tBuNO$_2$ is also among the materials yielding the largest birefringence with $|\Delta n| = 0.0252$. Importantly, the rate constant k_1^{or} associated with the faster contribution is significantly larger for tBuCN and tBuNO$_2$ as compared to pDR1M, with an increase by a factor of 5.7 and 7 respectively. This indicates that the photoisomerization reaction is facilitated in the molecular thin films made of the triphenylamino azo derivatives as compared to polymer thin films where the movement of azo units is hindered by the polymer backbone. In agreement with the faster orientation reported for tBuCN and tBuNO$_2$ during the orientation cycle, the remnant birefringence is also found among the smallest one for tBuCN and tBuNO$_2$. This implies that a material that shows faster photoinduced anisotropy also loses its anisotropy more readily. Nevertheless, it is difficult to observe a trend on the dominant rate constant during the relaxation process. For the polymer sample, the weights of the two rate constants are close to each other ($m_1^{rel} = 46.2$ % while $m_2^{rel} = 53.8$ %) while in the molecular thin films of the triphenylamino azo

compounds the slow rate constant is at least 3 times larger than the fast rate constant. This indicates that the relaxation process is mainly driven by the angular redistribution of the E isomers when the irradiation light is switched off. This is different from the orientation cycle where all dynamics are mainly driven by the fast rate constant for both types of materials.

Other compounds that are poorly absorbing of 532 nm radiation such as CF_3CN also show faster orientational rate constant ($k_1^{or} = 8.450$ s^{-1}) even though the induction of the photoisoimerization reaction is not optimized in terms of excitation-absorption match. This trend shows clearly that when the rate of photoisomerization is improved, its relaxation will also be facilitated yielding a weaker residual birefringence. This emphasizes that an ideal azo-containing material that presents a fast response time, a high degree of photoinduced birefringence and a high residual birefringence must display a subtle balance between its surrounding free volume, its associated glass transition temperature and its absorption coefficient at the excitation wavelength. Mixtures or doped systems may be a valuable approach to improve both rates and level of photoinduced orientation. The proper selection of a material for a given application is also critical. For example, one may not need a very high level of birefringence (i.e. $|\Delta n| = 0.2$) in optical data storage application since the optical read-out can be done with high sensitivity with a much lower intrinsic birefringence but the speed (rate) of the induced birefringence is the most critical for high-density storage. The triphenylaminoazo compounds such as tBuCN or tBuNO$_2$ can therefore be valued for their response time significantly faster than that for the pDR1M polymer. The degree of birefringence is still large and can be detected easily making molecular thin films interesting organic systems for fast optical switching.

Table 3-1: Summary of the properties of the azo polymer and triphenylaminoazo compounds processed as thin films on glass substrates. Fit parameters obtained from modeling the photoinduced birefringence curves in thin films recorded at a wavelength of 632.8 nm during an irradiation cycle (λ_{irr}= 532 nm, irradiance of 80 mW/cm^2). R is the correlation coefficient of the fit. Error on the rate constant are reported in brackets.

				Orientation cycle			$y_{orientation}\left(t\right) = m_1^{or}e^{-k_1^{or}t} + m_2^{or}e^{-k_2^{or}t} + m_3^{or}$				
Compound	T_g °C	λ_{max}(abs) / nm	Film thickness / nm	m_1^{or}	k_1^{or} /s^{-1} fast	m_2^{or}	k_2^{or} /s^{-1} slow	m_3^{or} $\left|\Delta n_{max}\right|$	m_1^{or} %	m_2^{or} %	R
pDR1M-11%	110	492	470	-0.04619(19)	1.337(10)	-0.00435(8)	0.0712(15)	0.0458(1)	91.4	8.6	0.993
tBuNO$_2$	118	508	450	-0.02437(8)	7.641(51)	-0.00044(1)	0.0333(13)	0.0252(1)	98.2	1.8	0.992
tBuCN	117	482	580	-0.02796(7)	9.400(50)	-0.00063(1)	0.0115(4)	0.0283(1)	97.8	2.2	0.995
tBuCO$_2$Me	112	468	520	-0.02100(21)	5.229(91)	-0.00128(120)	0.0017(18)	0.0206(12)	94.5	5.5	0.941
CarbNO$_2$	202	508	480	-0.03214(14)	2.535(19)	-0.00171(2)	0.0225(6)	0.0317(1)	94.9	5.1	0.990
CarbCN	201	482	375	-0.01455(10)	5.550(80)	-0.00494(8)	0.5364(86)	0.0198(1)	74.7	25.3	0.992
CarbCO$_2$Me	187	468	550	-0.01898(10)	1.712(15)	-0.00104(2)	0.0254(8)	0.0198(1)	94.8	5.2	0.986
CF$_3$NO$_2$	62	477	300	-0.01740(16)	4.328(68)	-0.00096(4)	0.0079(8)	0.0159(1)	94.8	5.2	0.958
CF$_3$CN	68	457	450	-0.01602(8)	8.450(89)	-0.00037(2)	0.1284(96)	0.0162(1)	97.7	2.3	0.983
CF$_3$CO$_2$Me	65	445	350	-0.01534(6)	6.863(51)	-0.00044(2)	0.0884(35)	0.0154(1)	97.2	2.8	0.991

Table 3-2: Fit parameters obtained from modeling the birefringence relaxation curves recorded at a wavelength of 632.8 nm. R is the correlation coefficient of the fit. Error on the rate constant are reported in brackets.

				Relaxation cycle				
			$y_{relaxation.}(t) = m_1^{rel}\left(1-e^{-k_1^{rel}t}\right) + m_2^{rel}\left(1-e^{-k_2^{rel}t}\right) + m_3^{rel}$					
Compound	m_1^{rel}	k_1^{rel}/s^{-1} fast	m_2^{rel}	k_2^{rel}/s^{-1} slow	$m_1^{rel}+m_2^{rel}+m_3^{rel}$ $\|\Delta n_{residual}\|$ (% residual birefringence)	% (m_1)	% (m_2)	R
pDR1M	-0.00558(5)	0.276(5)	-0.00650(2)	0.015322(123)	0.0316(12) (68.9%)	46.2	53.8	0.997
tBuNO$_2$	-0.00409(4)	0.685(1)	-0.01299(2)	0.008517(62)	0.0066(8) (26.2%)	24.0	76.0	0.999
tBuCN	-0.00206(2)	0.132(3)	-0.01359(4)	0.005864(41)	0.0092(8) (32.5%)	13.1	86.9	0.999
tBuCO$_2$Me	-0.00132(2)	0.107(3)	-0.00523(6)	0.004600(98)	0.0117(10) (56.7%)	20.1	79.9	0.998
CarbNO$_2$	-0.00173(3)	0.070(2)	-0.00772(2)	0.007509(92)	0.0215(7) (67.8%)	18.3	81.7	0.999
CarbCN	-0.00125(2)	0.171(5)	-0.00258(3)	0.006020(142)	0.0148(7) (74.7%)	32.7	67.3	0.996
CarbCO$_2$Me	-0.00071(1)	0.146(5)	-0.00221(4)	0.004609(134)	0.0161(6) (81.1%)	24.3	75.7	0.996
CF$_3$NO$_2$	-0.00172(4)	0.131(5)	-0.00757(4)	0.007459(110)	0.0049(11) (30.8%)	18.5	81.5	0.998
CF$_3$CN	-0.00369(4)	0.187(4)	-0.00724(9)	0.005013(114)	0.0059(17) (36.4%)	33.8	66.2	0.997
CF$_3$CO$_2$Me	-0.00183(3)	0.263(6)	-0.00260(1)	0.009661(124)	0.0098(7) (63.6%)	41.4	58.6	0.996

3.3.2   Birefringence Stability to Cycling.

Further birefringence experiments were conducted to evaluate the behavior of the nine compounds when subjected to several cycles of irradiation. The results are reported in Figure 3-3E for tBuNO$_2$ and CarbCO$_2$Me molecular thin films that were selected due to their faster orientation. The response over five cycles is consistent for both the orientation and relaxation processes. The compound CarbCO$_2$Me shows a birefringence of Δn= -0.0192 and a residual birefringence of Δn = -0.0168 after 250 s of relaxation, which yields 81 % of remnant birefringence that is higher than that of any other compounds of this study. Remarkably, all Carb compounds have a high degree of residual anisotropy ranging from 68 % (CarbNO$_2$), which is comparable to that for pDR1M (68.9 %), to 81% (CarbCO$_2$Me) as summarized in Table 3-2. This emphasizes again that even though a smaller degree of order is induced, our materials have a faster response time compared to pDR1M and yet can have the same level of residual birefringence. The ability of these compounds to yield reversible and erasable photoinduced anisotropy was investigated using circularly polarized light. After a cycle of orientation-relaxation, the residual anisotropy was erased using a circularly polarized 532 nm beam for 100 s. The results are shown in Figure 3-3F for two consecutive cycles for tBuNO$_2$, CarbNO$_2$ and CarbCO$_2$Me. For all compounds, the anisotropy was erased completely to zero and after a second irradiation the induction of anisotropy is comparable to the initial cycle. One can however notice a slight continuous increase in the plateau of birefringence for CarbCO$_2$Me after each irradiation cycle, which lets us suggest progressive plasticization of the thin films. Rotation of the Carb azo units operates in one block and requires enough space due to the bulky Carb units, which can thus be achieved only after repetitive cycles of orientation and relaxation.

3.3.3 Polarization-modulation linear dichroism infrared spectroscopy.

In order to investigate the photoinduced orientation at the molecular level during a cycle of orientation-relaxation, we have investigated the linear dichroism of irradiated thin films in the mid-infrared range using PM-IRLD spectroscopy. This powerful method with monolayer sensitivity has already been used successfully for the study of azobenzene-containing materials such as liquid crystalline materials as well as doped and functionalized polymer thin films.[30,32] It allows the motions of photoactive and non-photoactive units to be dynamically disentangled, thereby yielding a better appreciation of both the polarity and the steric effects associated with molecular motions.[43] The determination of the linear dichroism value $\Delta A = A_{//} - A_{\perp}$ is therefore a critical parameter to assess the orientational behavior of the azo compounds by following the evolution of their individual vibrational normal modes. This sheds light on the part of the molecule that undergoes molecular reorientation upon irradiation with linearly polarized light. $A_{//}$ and $A_{\perp}$ refer to the polarized absorbances parallel and perpendicular to the direction of the polarized pump laser, respectively. Therefore, upon irradiation, a vibrational mode with an initial dominant component along the $//$ direction will experience an angular reorientation along the $\perp$ direction, yielding a negative value for ΔA. Conversely, a mode with a dominant component initially oriented along $\perp$ direction will have a positive ΔA. To obtain a quantitative information about the time-dependent behavior of the different vibrational bands associated with the triphenylaminoazo derivatives, a distribution function, F_{θ}, is usually defined. F_{θ} is proportional to the normalized dichroism ratio $\Delta A/3A_0$ where A_0 designates the absorbance prior to irradiation for a given vibrational mode such as defined in Equation 3-4. In azo materials the distribution function is model-dependent so that both uniaxial and biaxial models can be used to accurately quantify the level of photoinduced orientation.[31] In uniaxial orientation models, the molecular orientation can be described using a single angle θ that describes the orientation of the long molecular axis of the chromophore with respect to the polarized excitation. This model implies that rod-like molecules can orient perpendicularly to the excitation light within the plane of the film or out-of-the-plane direction (i.e. along the beam propagation

direction) with the same probability. In bi-axial models, the orientation is more complex to describe since the rod-like molecules do not have the same probability to orient along the plane and out-of-plane directions. Therefore, two angles θ and ϕ must be used to define the orientational parameters associated with such anisotropic molecular orientation.[53] Based on previous studies performed in azo polymers containing a low concentration of dyes, an uniaxial model is generally appropriate, while for higher dye concentrations, biaxial models provide more accurate description of the molecular orientation. In the present study, separated measurements of polarized $A_{//}$ and $A_{\perp}$ were initially performed (Figure A-1) confirming that the chromophore orientation can be accurately described by an uniaxial model for the study of vibrational modes with well-defined symmetry such as symmetric stretching mode of NO_2 (Figure A-1). Although the high density of azo molecules would be in favor of a biaxial-type orientation, the large size of the chromophores together with a larger free volume around each individual chromophore are presumably the critical parameters that yield an uniaxial orientation. Therefore, in the present study the uniaxial model is valid for the present molecular materials and the distribution function can be described by:

$$F_\theta = \frac{A_{//} - A_{\perp}}{3A_0} = \frac{\Delta A}{3A_0}$$ [3-4]

Using the uniaxial distribution, the F_θ parameter is equivalent to the second order Legendre polynomial also defined as the second order parameter $\langle P_2 \rangle = 1/2 \langle 3\cos^2\theta - 1 \rangle$. In the case of a uniaxial distribution function, the limit values are $F_\theta = 1$ for a perfect alignment along the // direction ($\theta = 0$) and $F_\theta = -0.5$ for a perfect alignment in the $\perp$ direction ($\theta = \frac{\pi}{2}$) while $F_\theta = 0$ indicates an isotropic material.
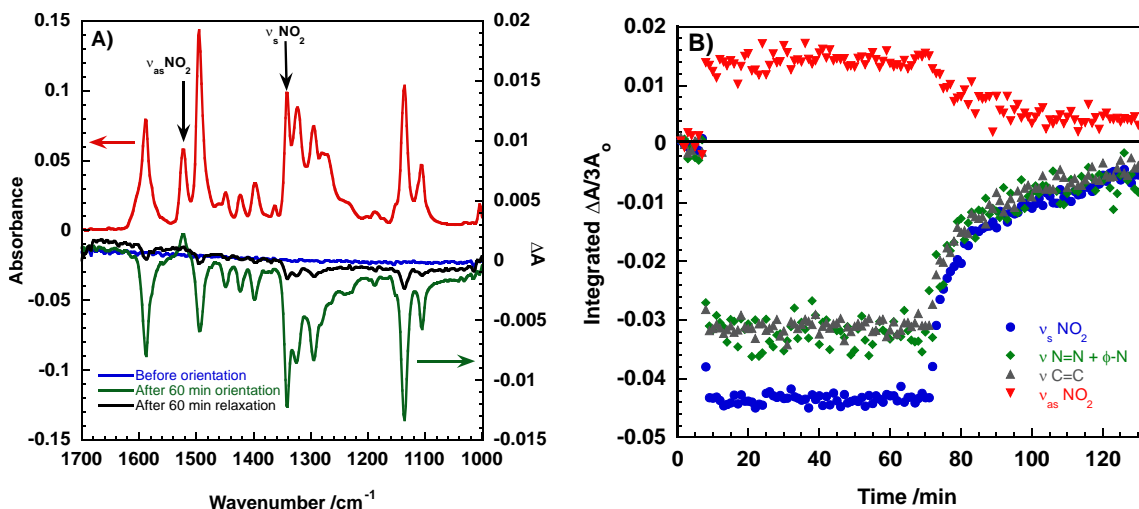
Figure 3-4: (A) Infrared spectrum of tBuNO$_2$ molecular thin films and photoinduced linear dichroism at t = 0 min., after 60 min. of orientation and after 60 min. of relaxation. (B) Dynamics of selected vibrational modes such as symmetric (ν_s, 1343 cm^{-1}) and antisymmetric (ν_{as}, 1516 cm^{-1}) stretching modes of NO$_2$, stretching phenyl modes ν_{8a}, ν_{8b} (1600 cm^{-1} and 1588 cm^{-1}) and coupled $\nu_{N=N}+\nu_{Ph-N}$ mode (1395 cm^{-1}) during irradiation and relaxation cycles.

Here below, we have measured the photoinduced anisotropy for the nine azo triphenylamino compounds and the azo reference polymer. Selected dynamics for tBuNO$_2$ and CarbNO$_2$ are shown in Figure 3-4 and Figure 3-5 while the measurements for all other compounds and pDR1M thin films are shown in the appendices sections (Figure A-2 to Figure A-9) for selected vibrational modes. The vibrational assignments are summarized in the appendices section (Table A-1). Because of the high amount of aromatic cycles and the overall geometry of the molecules, the vibrational modes associated with the aromatic cycles such as the deformation modes C-H of the phenyl rings, (1107 and 1136 cm^{-1}), and the elongation modes of the C=C, ν_{8a} (1600 cm^{-1}) and ν_{8b} (1588 cm^{-1}), do not present a well-defined symmetry and are therefore not ideal probe groups to estimate a clear-cut molecular orientation. Nevertheless this observation is also true for azopolymer studies where a limited number of groups on the donor side or the polymer backbone had a well defined symmetry and could be exploited to provide information about the electron donor group orientation. Generally the degree of

orientation of the $\nu_{8a} + \nu_{8b}$ phenyl elongation modes are very close in magnitude to the symmetric stretching mode of the nitro group as shown in the appendices for pDR1M (Figure A-9). Such observation can be used as a reference to evaluate the influence of the bulky donor group. Other modes display better defined symmetry in particular on the electron-accepting side of the chromophore. For example, the symmetric ν_S (1343 cm^{-1}) and antisymmetric ν_{as} (1516 cm^{-1}) modes of the nitro group are perpendicular to each other and should therefore show different signs in anisotropic systems. The symmetric mode of NO_2 is oriented along the long axis of the chromophore and can be efficiently used to follow the orientational dynamics of the chromophore. Also, modes such as νPh-N (1294 cm^{-1}) or coupled modes νN-N + Ph-N (1395 cm^{-1}) also present a larger net dipolar moment along the main molecular axis. For the series containing a cyano group, the stretching mode νC≡N (2227 cm^{-1}) is also of interest. Although the trifluoromethyl groups $-CF_3$ show a clear spectral signature with an elongation normal mode ν_{as}(C-F) at 1054 cm^{-1}, these groups cannot be used to probe the electron donor side of the chromophores due to their relative orientation devoid of unidirectionality.

As shown for CF_3CN (Figure A-6) and CF_3NO_2 (Figure A-8), the symmetric and antisymmetric -CF_3 modes are clearly observable on the IR spectra but only very weak net molecular orientation of these two modes can be measured. The four CF3 groups located on the donor side have a large range of angular net contributions and the average of their orientation appears to yield very little dichroism. Alternatively, if CF_3 was substituted in the R^1 position rather than R^2 (Figure 3-1) larger dichroism could presumably be observed since the angular distribution would be narrower.
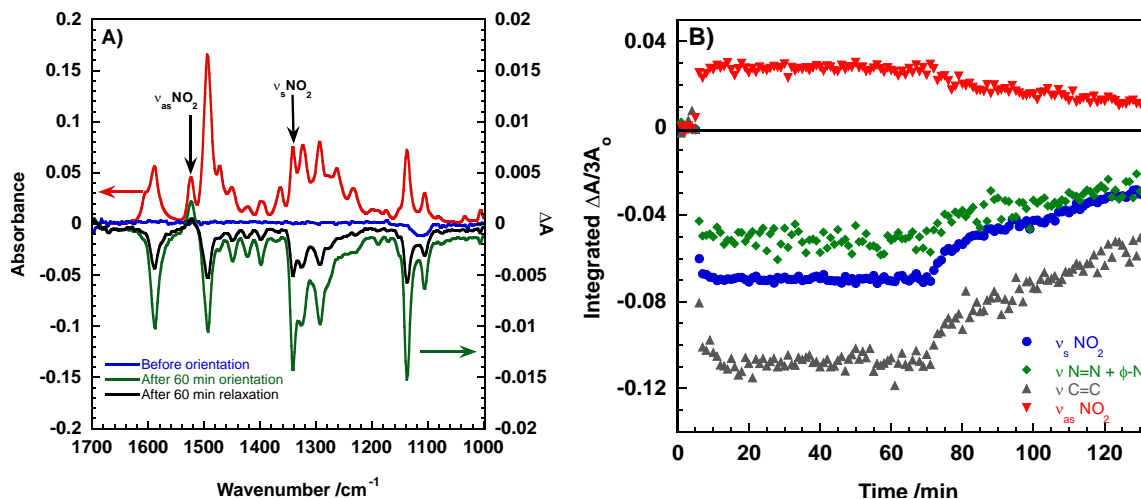
Figure 3-5: (A) Infrared spectrum of CarbNO$_2$ molecular thin films and photoinduced linear dichroism at t = 0 min., after 60 min. of orientation and after 60 min. of relaxation. (B) Dynamics of selected vibrational modes such as symmetric (v$_s$, 1343 cm^{-1}) and antisymmetric (v$_{as}$, 1516 cm^{-1}) stretching modes of NO$_2$, stretching phenyl modes v$_{8a}$, v$_{8b}$ (1600 cm^{-1} and 1588 cm^{-1}) and coupled v$_{N=N}$+v$_{Ph-N}$ mode (1395 cm^{-1}) during irradiation and relaxation cycles.

The linear dichroic spectra (ΔA) in the [1000-1700] cm^{-1} spectral range prior to irradiation, at the orientation plateau upon light exposure and after a long relaxation time are presented in Figure 3-5 and Figure 3-6 for tBuNO$_2$ and CarbNO$_2$, respectively (Figure 3-4A and Figure 3-5A), along with the corresponding time-evolution of the amplitude of selected modes (Figure 3-4B and Figure 3-5B). The ΔA spectra are superimposed with the reference absorption spectrum recorded on the same sample area prior to irradiation. In the case of tBuNO$_2$ thin films (Figure 3-4A), most vibrational modes are negative indicative of an angular orientation of the vibrational mode perpendicular to the irradiation polarization direction. This also highlights that most vibrational modes have a strong contribution of their dipole moment along the long axis of the molecule such as v$_s$NO$_2$. Concomitantly, vibrational modes that have a neat vibrational symmetry oriented perpendicularly to the long molecular axis have a positive linear dichroism such as v$_{as}$NO$_2$ which is the only mode exhibiting a positive anisotropy as seen in Figure 3-4A and Figure 3-5A. From Figure 3-4B and Figure 3-5B, the orientational dynamics can be investigated. We thus can clearly see that the plateau of orientation is reached within the

first 1-3 minutes of irradiation for both compounds. The level of induced linear dichroism yields values of $F_\theta = -0.045$ and $F_\theta = -0.07$ for tBuNO$_2$ and CarbNO$_2$, respectively, while for the pDR1M thin film, the value is larger with $F_\theta = -0.13$. It is noteworthy that for CarbNO$_2$, the C=C vibrations experience the most anisotropy. This indicates clearly that the electron-accepting group and the electron-donating group that holds the carbazole units undergo simultaneous angular reorientations. The donor unit being very bulky, this confirms that a larger free volume occupied by the donor unit has been created during the angular reorientation of the azo unit facilitating the orientation of the surrounding units and thus explaining the faster orientation and relaxation rates. This also confirm that the position of the carbazole groups on R^1 (Figure 3-1) yields a larger dichroism as pointed out earlier than for the -CF$_3$ groups positioned on R^2. This observation corroborates the fact that the chromophore orients as a whole unit in the perpendicular direction to the impinging polarization direction. The remnant linear dichroism confirms the birefringence measurements previously recorded and shows that for fast-responsive azo chromophores, the induced dichroism is lower while the decay of dichroism is faster due to the increased amount of free volume induced by the bulky donor substituent. Interestingly, in the case of the CarbNO2, the relaxation never reaches a steady state even after one hour of relaxation. This indicates that there is a large distribution of free volume that are involved during the relaxation which is presumably due to the position of the carbazole groups with respect to the phenyl group to which they are attached in R^1.
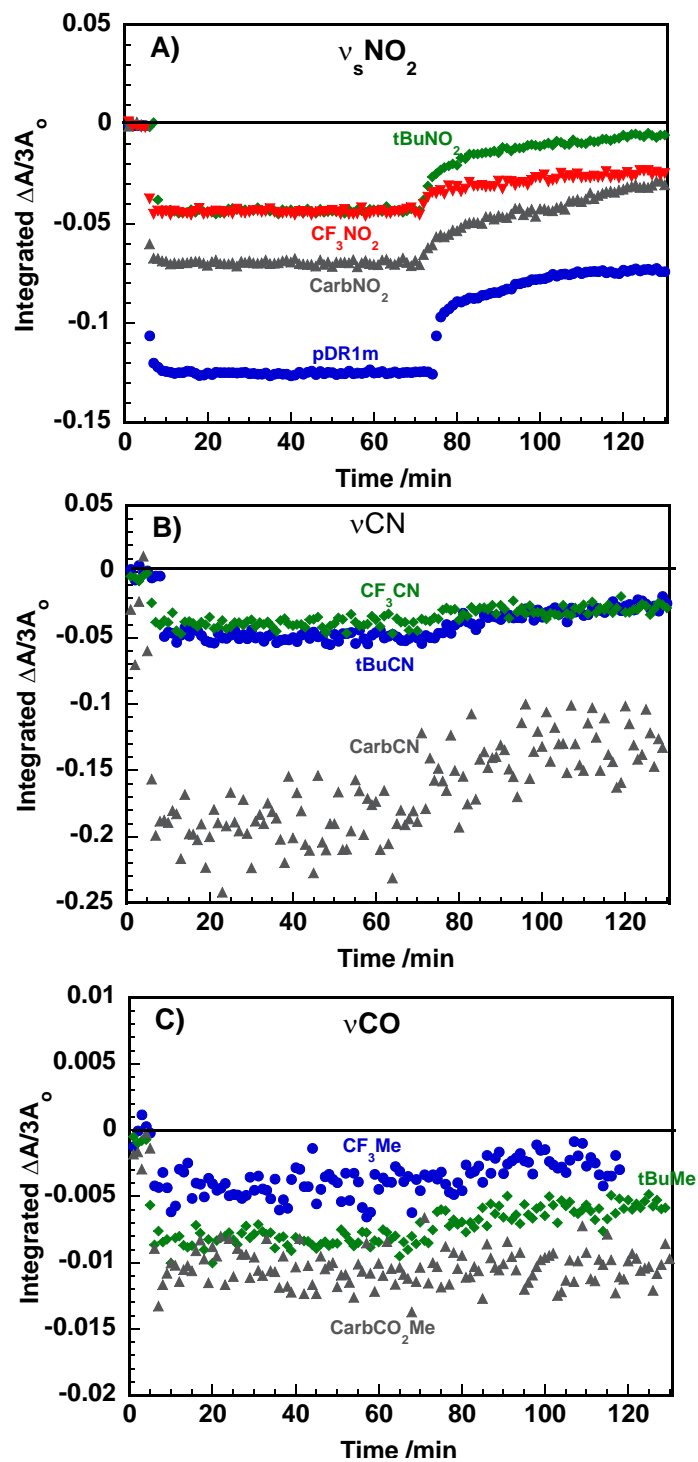
Figure 3-6: (A) Dynamics of orientation of the nitro symmetric stretching modes of tBuNO₂, CF₃NO₂, CarbNO₂ and pDR1M thin films. (B) Dynamics of orientation of the CN symmetric stretching modes of tBuCN, CF₃CN, CarbCN.

In Figure 3-6A, we have reported the linear dichroism dynamics of the NO_2 band for the three triphenylaminoazo compounds together with pDR1M. Several factors such as the glass transition temperatures T_g and the absorption cross sections of the material must be carefully examined for comparison. For the four compounds, the maximum absorption wavelengths are about 490 ± 20 nm and their molar absorption coefficients in solution exhibit very similar values of 27.0×10^3, 30.5×10^3 and 24.6×10^3 $mol^{-1}.L.cm^{-1}$ for tBuNO$_2$, CarbNO$_2$ and CF$_3$NO$_2$, respectively and 30×10^3 for pDR1M thin film. The glass transition temperatures T_g are however very distinct for the three triphenylaminoazo compounds ranging from 62 ºC for CF$_3$NO$_2$ to 202 ºC for CarbNO$_2$ while tBuNO$_2$ and pDR1M have a T_g around 110 ºC. The comparative experiments carried out on this series show no direct correlation between T_g: indeed pDR1M shows the highest degree of orientation while tBuNO$_2$ shows the smallest orientation that is comparable to the CF$_3$NO$_2$ one. Conversely, CarbNO$_2$ shows an intermediate level of anisotropy as observed in birefringence measurements even though it has a higher glass transition temperature. This shows again the importance of microscopic free volume accessible in the triphenylaminoazo derivatives highlighting the fact that angular reorientation can be very effective even for high T_g materials endowed with bulky substituents as already demonstrated for the formation of surface relief gratings.[8,49] Figure 3-6B shows the series of azo molecules substituted with a CN group as an electron acceptor. Here again the same trend is observed: the CarbCN compound (T_g = 201 ºC) shows a highest level of anisotropy compared to those of tBuCN (T_g = 117 ºC; Figure A-2) and CF$_3$NO$_2$ (T_g = 68 ºC; Figure A-8). Figure 3-6C shows the anisotropy associated with the C=O stretching mode (ν_s C=O, 1731 cm^{-1}) of the azo ester molecules containing the methoxycarbonyl group –CO$_2$Me as an electron-withdrawing substituent. A poor level of anisotropy and noisy signals are due to the weak band intensity but the trend is again the same, namely bulkier substituents yield larger anisotropy.

3.4   Conclusion

In conclusion, we have probed the dynamics associated with the angular reorientation of triphenylaminoazo dyes using birefringence and polarization modulation infrared spectroscopy. These complementary approaches provided valuable set of macroscopic

and molecular information during the angular photoinduced molecular reorientation. The fast rate constants associated with the photoinduced anisotropy are enhanced for the whole series of compounds compared to a reference azopolymer. This indicates that the dynamics within molecular glassy thin films can be significantly improved by tuning the size of the electron donor group with substituents of varying bulkiness. Several candidates of the series show improved properties like the carbazole series that exhibit a higher level of photoinduced and remnant anisotropy whereas their glass transition temperature is above 200 ºC. The tBu series shows an enhanced orientation rate by a factor of 7 despite similar glass transition temperatures to the reference azopolymer. This study shows clear evidence the present series of small molecule-based thin films of azo compounds exhibit switching dynamics that are faster than those of polymers doped with azobenzene groups and than a reference functionalized polymer (pDR1M). This study highlights that molecular functional materials display larger orientational rates with regard to those of their polymer analogues, which can impact considerably the choice for polymer- or small molecule-based technologies encountered in the field of organic electronics and photonics.

3.5 References

(1) Priimagi, A.; Lindfors, K.; Rochon, P. *ACS Appl. Mater. Interfaces.* **2009**, *1*, 1183-1189.

(2) Delaire, J. A.; Nakatani, K. *Chem. Rev.* **2000**, *100*, 1817-1846.

(3) Gust, D.; Andréasson, J.; Pischel, U.; Moore, T. A.; Moore, A. L. *Chem. Commun.* **2012**, *48*, 1947-1957.

(4) Matharu, A. S.; Jeeva, S.; Ramanujam, P. S. *Chem. Soc. Rev.* **2007**, *36*, 1868-1880.

(5) Hagen, R.; Bieringer, T. *Adv. Mater.* **2001**, *13*, 1805-1810.

(6) Neporent, B. S.; Stolbova, O. V. *Opt. Spektrosk.* **1963**, *14*, 624-633.

(7) Makushenko, A. M.; Neporent, B. S.; Stolbova, O. V. *Opt. Spektrosk.* **1971**, *31*, 741-748.

(8) Ishow, E.; Camacho-Aguilera, R.; Guerin, J.; Brosseau, A.; Nakatani, K. *Adv. Funct. Mater.* **2009**, *19*, 796-804.

(9) Di Florio, G.; Brundermann, E.; Yadavalli, N. S.; Santer, S.; Havenith, M. *Nano Lett.* **2014**, *14*, 5754-5760.

(10) Lagugné-Labarthet, F.; Buffeteau, T.; Sourisseau, C. *Phys. Chem. Chem. Phys.* **2002**, *4*, 4020-4029.

(11) R. D. Schaller, R. J. S., Y. R. Shen, F. Lagugné-Labarthet. *Opt. Lett.* **2003**, *28*, 1296-1298.

(12) Yu, Y.; Nakano, M.; Ikeda, T. *Nature.* **2003**, *425*, 145.

(13) Yamada, M.; Kondo, M.; Mamiya, J.; Yu, Y.; Kinoshita, M.; Barrett, C. J.; Ikeda, T. *Angew. Chem. Int. Edit.* **2008**, *47*, 4986-4988.

(14) Liu, Z.-X.; Feng, Y.; Yan, Z. C.; He, Y.-M.; Liu, C.-Y.; Fan, Q.-H. *Chem. Mater.* **2012**, *24*, 3751-3757.

(15) Mermut, O.; Barrett, C. J. *Analyst.* **2001**, *126*, 1861-1865.

(16) Zakrevskyy, Y.; Stumpe, J.; Faul, C. F. *Adv. Mater.* **2006**, *18*, 2133-2136.

(17) Joshi, G. K.; Blodgett, K. N.; Muhoberac, B. B.; Johnson, M. A.; Smith, K. A.; Sardar, R. *Nano Lett.* **2014**, *14*, 532-540.

(18) Holme, N. C. R.; Ramanujam, P. S.; Hvilsted, S. *Opt. Lett.* **1996**, *21*, 902-904.

(19) Stockermans, R. J.; Rochon, P. L. *Appl. Opt.* **1999**, *38*, 3714-3719.

(20) Priimagi, A.; Shevchenko, A. *J. Polym. Sci., Part B: Polym. Phys.* **2014**, *3*, 163-182.

(21) Goldenberg, L. M.; Lisinetskii, V.; Gritsai, Y.; Stumpe, J.; Schrader, S. *Adv. Mater.* **2012**, *24*, 3339-3343.

(22) Goldenberg, L. M.; Lisinetskii, V.; Ryabchun, A.; Bobrovsky, A.; A., S. *ACS Photonics.* **2014**, *1*, 885-893.

(23) Snell, K. E.; Mevellec, J.-Y.; Humbert, B.; Lagugné-Labarthet, F.; Ishow, E. *ACS Appl. Mater. Interfaces.* **2015**, *7*, 1932-1942.

(24) Shimamura, A.; Priimagi, A.; Mamiya, J.-I.; Ikeda, T.; Yu, Y.; Barrett, C. J.; A., S. *ACS Appl. Mater. Interfaces.* **2011**, *3*, 4190-4196.

(25) Zhao, Y.; Ikeda, T. *Smart light-responsive materials: Azobenzene-Containing Polymers and Liquid Crystals*; John Wiley & Sons: Hoboken, NJ, USA, 2009.

(26) Natansohn, A.; Rochon, P.; Pézolet, M.; Audet, P.; Brown, D.; To, S. *Macromolecules.* **1994**, *27*, 2580-2586.

(27) Yoneyama, S.; Yamamoto, T.; Tsutsumi, O.; Kanazawa, A.; Shiono, T.; Ikeda, T. *Macromolecules.* **2002**, *35*, 8751-8758.

(28) Zilker, S. J.; Huber, M. R.; Bieringer, T.; Haarer, D. *Appl. Phys. B.* **1999**, *68*, 893-897.

(29) Zilker, S. J.; Bieringer, T.; Haarer, D.; Stein, R. S.; van Egmond, J. W.; Kostromine, S. *Adv. Mater.* **1998**, *10*, 855-859.

(30) Buffeteau, T.; Natansohn, A.; Rochon, P.; Pézolet, M. *Macromolecules.* **1996**, *29*, 8783-8790.

(31) Buffeteau, T.; Pézolet, M. *Macromolecules.* **1998**, *31*, 2631-2635.

(32) Lagugné-Labarthet, F.; Freiberg, S.; Pellerin, C.; Pézolet, M.; Natansohn, A.; Rochon, P. *Macromolecules.* **2000**, *33*, 6815-6823.

(33) Tanino, T.; Yoshikawa, S.; Ujike, T.; Nagahama, D.; Moriwaki, K.; Takahashi, T.; Kotani, Y.; Nakano, H.; Shirota, Y. *J. Mater. Chem.* **2007**, *17*, 4953-4963.

(34) Kim, M.-J.; Seo, E.-M.; Vak, D.; Kim, D.-Y. *Chem. Mater.* **2003**, *15*, 4021-4027.

(35) Nakano, H.; Takahashi, T.; Kadota, T.; Shirota, Y. *Adv. Mater.* **2002**, *14*, 1157-1160.

(36) Nakano, H.; Tanino, T.; Takahashi, T.; Ando, H.; Shirota, Y. *J. Mater. Chem.* **2008**, *18*, 242-246.

(37) Fuhrmann, T.; Tsutsui, T. *Chem. Mater.* **1999**, *11*, 2226-2232.

(38) Feng, S.; Duan, L.; Hou, L.; Qiao, J.; Zhang, D.; Dong, G.; Wang, L.; Qiu, Y. *J. Phys. Chem. C.* **2011**, *115*, 14278-14234.

(39) Duan, L.; Hou, L.; Lee, T.-W.; Qiao, J.; Zhang, D.; Dong, G.; Wanga, L.; Qiu, Y. *J. Mater. Chem.* **2010**, *20*, 6392-6407.

(40) Zhuang, H.; Zhang, Q.; Zhu, Y.; Xu, X.; Liu, H.; Li, N.; Xu, Q.; Li, H.; Lu, J.; Wang, L. *J. Mater. Chem. C.* **2013**, *1*, 3816-3824.

(41) Miao, S.; Zhu, Y.; Zhuang, H.; Xiaping, X., Li, Hua, Sun, R.; Li, N.; Ji, S.; Lu, J. *J. Mater. Chem. C.* **2013**, *1*, 2320-2327.

(42) Ishow, E.; Bellaïche, C.; Bouteiller, L.; Nakatani, K.; Delaire, J. A. *J. Am. Chem. Soc.* **2003**, *125*, 15744-15745.

(43) Natansohn, A.; Rochon, P.; Meng, X.; Barrett, C. J.; Buffeteau, T.; Bonenfant, S.; Pézolet, M. *Macromolecules.* **1998**, *31*, 1155-1161.

(44) Ho, M.-S.; Natansohn, A.; Barrett, C. J.; Rochon, P. *Can. J. Chem.* **1995**, *73*, 1773-1778.

(45) Karageorgiev, P.; Neher, D.; Schultz, B.; Stiller, B.; Pietsch, U.; Giersig, U.; Brehmer, L. *Nat. Mater.* **2005**, *4*, 699-703.

(46) Natansohn, A.; Rochon, P.; Gosselin, J.; Xie, S. *Macromolecules.* **1992**, *25*, 2268-2273.

(47) Rodriguez, V.; Adamietz, F.; Sanguinet, L.; Buffeteau, T.; Sourisseau, C. *J. Phys. Chem. B.* **2003**, *107*, 9736-9743.

(48) Buffeteau, T.; Lagugné-Labarthet, F.; Pézolet, M.; Sourisseau, C. *Macromolecules.* **2001**, *34*, 7514-7521.

(49) Snell, K. E.; Stéphan, N.; Pansu, R. B.; Audibert, J.-F.; Lagugné-Labarthet, F.; Ishow, E. *Langmuir.* **2014**, *30*, 2926-2935.

(50) Lagugné-Labarthet, F.; Sourisseau, C. *New J. Chem.* **1997**, *21*, 879-887.

(51) Fischer, M.; El Osman, A.; Blanche, P.-A.; Dumont, M. *Synth. Met.* **2000**, *115*, 139-144.

(52) Ishow, E.; Lebon, B.; He, Y.; Wang, X.; Bouteiller, L.; Galmiche, L.; Nakatani, K. *Chem. Mater.* **2006**, *18*, 1261-1267.

(53) Buffeteau, T.; Lagugné-Labarthet, F.; Sourisseau, C.; Kostromine, S.; Bieringer, T. *Macromolecules.* **2004**, *37*, 2880-2889.

Chapter 4

4 Second harmonic generation from gold meta-molecules with three-fold symmetry

The unique optical properties of arrays of metallic nanoparticles are of great interest for many applications such as in optical data storage, sensing applications, optoelectronic devices or as platforms to increase the detection limit in spectroscopic measurements. Nonlinear optical phenomena can also be altered by metallic nanostructures opening new possible applications. In this work, arrays composed of non-centrosymmetric individual structures with three fold axial symmetry made of gold are designed and fabricated using electron beam lithography. The nonlinear optical properties of these structures are investigated using second-harmonic generation microscopy (SHGM) with a femtosecond excitation source set near the plasmon resonance frequency. Modeling of the electromagnetic field distribution around the metallic structures is performed using finite-difference time-domain (FDTD) method, highlighting the confinement of the SHG signal and its polarization dependence. Polarization-resolved measurements are conducted to correlate the SHG signal with the structure and symmetry of the individual nanostructures. Since both two-photon induced photoluminescence (TPPL) and SHG signals are produced upon the excitation of these structures, lifetime measurements are performed to further evaluate the magnitude of these two effects.

4.1 Introduction

In the past two decades, metallic nanostructures have been developed for a variety of applications such as in optical data storage,[1-5] biosensing,[6,7] biomarkers,[8-11] and high-sensitivity single molecule spectroscopy.[12-15] Nanoparticles, such as gold spheres,[16] pyramids,[17] and triangular prisms,[18] have wisely been selected according to their opto-geometric parameters and the resulting localized surface plasmon resonances (LSPR). For a given metal, the LSPR can be tuned from visible to near-infrared region by changing the size, geometry or periodicity of the individual nano-particles.[19] Plasmonic properties of nanostructures are keys to many applications aiming at signal enhancement and low threshold sensing. For example, the fluorescence signal from a variety of

fluorophores was enhanced,[20] thus facilitating its detection and allowing one to use weaker light intensity or significantly reduced acquisition time. Applications in chiral sensing have been demonstrated and involve the use of metallic chiral structures, such as star-shaped chiral gold nanostructures that interact differently depending on the parity of the circularly (left or right) polarized light.[21-23] In another example, periodical silver nano-disk arrays fabricated by electron-beam lithography have been used for sensing bacteria, which provides an elegant approach for low cost and high yield detection of specific bacteria species.[24]

Among the variety of optical properties affected by the morphology of metallic nano-structures, nonlinear optical (NLO) properties, observed under excitation by pulsed lasers, are of particular interest due to the high local energy concentration required for a significant NLO response generation that can be further confined in the vicinity of the metal surface through electromagnetic local field enhancement.[25-27] This local energy confinement due to the induced localized oscillations of the free electrons[28] on nanostructured surfaces can be probed in turn via NLO. Due to the symmetry breaking at the nanostructure surface, the most appropriate process in this perspective appears to be second-harmonic generation (SHG). Within the dipolar approximation, centro-symmetry breaking is a condition for SHG observation whereas higher order coupling, such as quadrupolar, are less efficient.[29] SHG appears indeed as an ideal nanostructure probing technique with extreme sensitivity to surface-specific properties of the nanoparticles, or more generally, to their geometry either as individual entities, or in assemblies. Denoting the nonlinear susceptibility tensor of the material of the studied structures as $\chi^{(2)}$, the second order nonlinear polarization $P_i^{2\omega}$ can be expressed as:

$$P_i^{2\omega} = \sum_{j,k} \chi_{ijk}^{(2)} E_j(\omega) E_k(\omega) \qquad \text{[4-1]}$$

where ω is the fundamental frequency of the input laser beam. According to this expression, SHG can be enhanced by increasing the power of the laser beam or by modifying the elements of the susceptibility tensor intrinsic to the material or nanostructure. Since increase in the excitation power is always limited by the photo-damage to the sample, optimizing the second order NLO properties of the material through its $\chi_{ijk}^{(2)}$ susceptibility tensor by advanced nanofabrication technology is a

promising way for surpassing the current limitations of SHG structures. More specifically, the possibility to fully control the composition, size, symmetry, shape, 2D and 3D arrangement of an ensemble of individual nanoparticles allows for the fine tuning of the NLO properties of meta-materials.[5,16,30]

The conception and design of the nano-structure template are crucial for obtaining the targeted result. Gold is known to be a stable plasmonic material with quadrupolar resonance in the visible range and dipolar resonance in the near-infrared range.[31] In the case of silver, the stability of the thin structure is very sensitive to oxidation and diffusion effects. Thus, surface roughness can change over time as micro-size grains appear at the surface. This yields a SHG signal originating from the rough metal interface convoluted with the SHG response from the ideal non-centrosymmetric features. Therefore, the built-in chemical surface stability of gold often makes it a material of choice in plasmonic applications. Beside its chemical surface stability, another advantage of gold is its aptitude towards surface functionalization and non-toxicity for living organisms, which makes it a material of choice for biological applications.[32-35] The excitation of gold structures with femtosecond light pulses yields both TPPL, as was shown on gold nanoplates,[36] and SH, generated by gold structures due to surface centro-symmetry breaking.[37] While the quantum yield of bulk gold fluorescence is extremely weak,[38] the second harmonic (SH) signal is even more difficult to detect here due to the isotropic property of bulk gold with eventual defects as its sole source. However, both phenomena are drastically enhanced, when the excitation light matches the conditions for surface plasmon resonance in the investigated nanostructures.

Motivated by the possibility to create and control SHG with perspectives of biological applications, we designed and fabricated by means of electron-beam lithography a series of three-fold triangular gold nanoprisms with variable inter-prism distances (Figure 4-1). The proposed design is based on the general template of octupolar molecules exhibiting three-fold symmetry, which had been proposed in the realm of molecular engineering and has been more recently up-scaled to meta-molecules as a new template allowing one to extend over the earlier dipolar model with specific advantages.[39-43] Here, metamolecules refer to the individual building blocks with three-fold symmetry that constitute a meta-

material or a metasurface. Compared to other known gold nano-prism structures, those proposed here are less dependent on the incident light polarization due to C_3 symmetry, which is important for further biological sensing applications to avoid the intensity variations in the detected signal due to the polarization effects as opposed to molecular interactions. This is a generic advantage in the many instances where polarization control of the incoming fundamental cannot be ensured, for example at the output of an optical fiber, which is one of the diverse configurations of relevance for remote device operation. Moreover, the selected structures and associated fabrication method can be implemented over large surfaces, which is an important prerequisite to the industrial development of plasmonic sensors.

The investigation of three-fold triangular nano-prisms structure was meant to complement our earlier work on nano-cavities with triangular shapes abiding to 3-fold symmetry carved by focused ion beam into a thin film of silver[41] and of gold[42,43] or following a pyramidal recess shape etched in a semiconductor substrate[38]. The purpose is to compare both types of structures in terms of their potential for SHG and nano-NLO. It was shown,[43] based on analysis of the SHG polarization diagram, that individual nano-cavities are interacting by exchange of propagative plasmon-polaritons through the surrounding gold surface, thus validating the building-up of nonlinear meta-molecules from adequate arrangements of nano-cavities. However, a similar investigation for nano-particles, known to interact at a smaller scale, had not been undertaken.

Herein, we report on SHG measurements from 2D arrays of non-centrosymmetric gold structures using nonlinear microscopy and spectroscopy techniques. We explore the influence of the prism geometry and the inter-prism gap width on the localized surface plasmon resonances and their coupling and, as a consequence, on the magnitude of the enhanced SHG signal mediated by coupling with localized surface plasmons. By controlling the gap distances between the adjacent gold nanostructures, a plasmon-mediated optical coupling can be further tuned. The SHG polarization-resolved microscopy measurements were correlated with electromagnetic field modeling to evaluate such optical coupling effect. A strong enhancement of the SHG signal from

nanoprisms was demonstrated for fundamental waves resonant or pre-resonant with the localized surface plasmons.

4.2   Experimental Methods

4.2.1   Electron beam lithography

Electron beam lithography (EBL) was used to produce the arrays of gold nanostructures, offering high reproducibility down to a 20 nm spatial resolution.[44] Glass cover-slips were first cleaned with a plasma cleaner. A positive photoresist (ZEP 520A, Zeon) thin film was spin-coated on the coverslip. A thin conductive layer (AquaSAVE, Mitsubishi Rayon America) was then spin-coated over the photoresist to avoid charging effects and loss of the resolution due to electrons flowing out of the irradiated area. The nanoscale structures were designed using a CAD software and then inscribed on the coverslip/photoresist surface using a LEO 1530 Field Emission scanning electron microscope (SEM) combined with a high precision interferometric stage. The conductive layer was dissolved and the underlying photoresist was developed. Thin films of 5 nm titanium and 50 nm gold layers were deposited by e-beam evaporation.
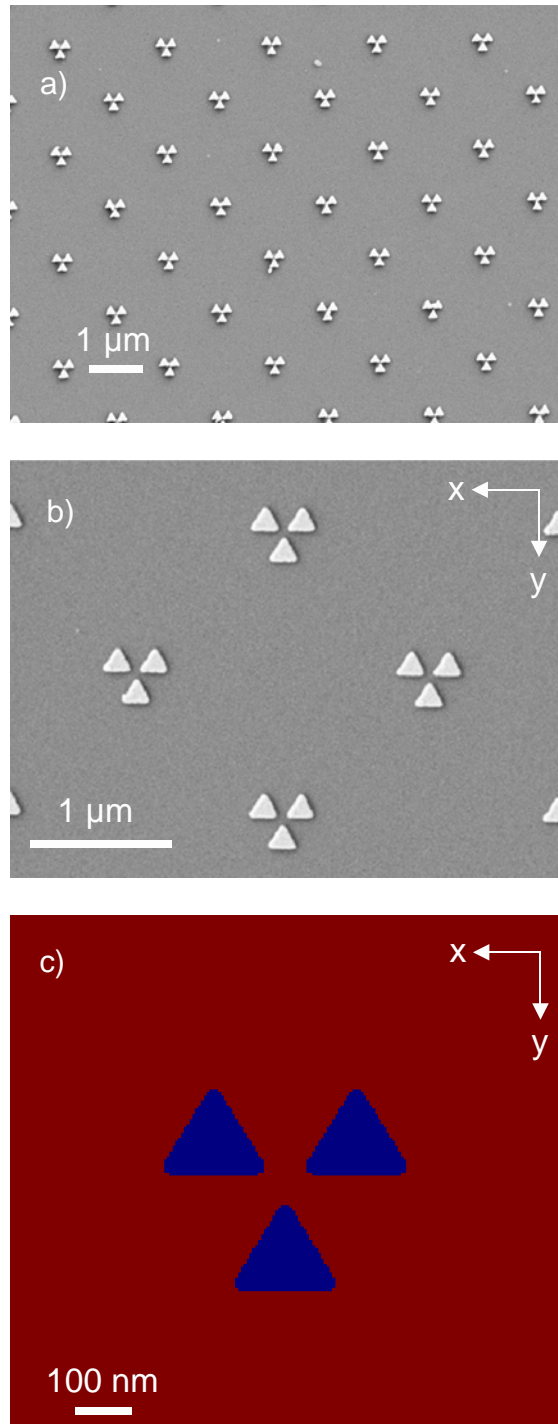
Figure 4-1: (a)(b)SEM image of triangular gold prisms sets inscribed on a glass coverslip. In this specific sample, the inter-triangle gap is set to (a) 0 nm and (b) 50 nm. (c) Refractive index of the FDTD simulated region. The gold is displayed as blue while red represents for vacuum.

The titanium served as an adhesion layer for gold. Finally, a lift-off procedure was used to remove the remnant photoresist and to obtain the desirable patterns. Figure 4-1 shows a typical SEM micrograph of the EBL fabricated sample. Each individual set of three triangular prisms were placed 2 µm away from each other excluding any interaction between the individual sets. The three equilateral triangular prisms form a 3-fold rotational symmetry (C_3) pattern. The gap, or the distance between each of the prisms, has been increased from 0 nm to 100 nm, with a step size of 25 nm yielding a series of 5 prisms sets with different gap-size. In Figure 4-1b, the side-length of each triangle is 200 nm, and the gap between a set of 3 triangles is set to 50 nm.

4.2.2   Extinction spectrum

Extinction measurements were performed using a modified microscope (Olympus IX 71) allowing one to measure the absorbance spectra in the visible range from selected (50×50) µm^2 surface. A halogen light source coupled to an optical fiber was collimated onto this surface with a (10x) microscope objective. Visible photons transmitted through the sample were collected with a second microscope objective (10x) and spectrally analyzed with a 150 grooves/mm grating prior to detection with a liquid nitrogen cooled CCD camera.

4.2.3   Finite-Difference Time-Domain (FDTD) simulation

The full-vector set of Maxwell equations for the studied gold triangular nanoprisms were numerically solved by the finite-difference time-domain (FDTD) method, of common use for solving electromagnetic problems such as waveguiding,[45] absorption,[46] nano-antenna properties,[30] and other design guidelines for optics.[47] The modeling of second harmonic generation requires a numerical module that considers the nonlinear optical properties of the material or structure of interest, which is accounted for by the second order susceptibility $\chi^{(2)}$. Lumerical FDTD Solutions (Vancouver, Canada) was used as the modeling software solution. The structures were assembled in 2D arrays with a

periodicity length of 2 μm. The non-centrosymmetric structures were defined as triangles with base length of 200 nm and composed of a 5 nm thick Ti layer to mimic the adhesion layer over a glass substrate, followed by a 50 nm thick gold layer similar to the fabricated platforms.[48] One set of 3 triangular prisms was selected and apices of the prisms were rounded with a 15 nm radius of curvature to match the geometry of the samples made by electron beam lithography (EBL). The input light source (λ=850, 780 nm) was set to short pulses of 150 fs width. The amplitude of the input field was set to 10^9 V.m^{-1}. The linear property of the defined structure was based on the properties of isotropic gold, while surface $\chi^{(2)}$ was set to a constant value of 3×10^{-20} m.V^{-1}.[49,50] The boundary conditions were chosen to be periodic along the x and y directions, while a perfect matching layer was used along the z direction. A mesh size of 5 nm was selected and the simulation was run via the Shared Hierarchical Academic Research Computing Network (SHARCNET; www.sharcnet.ca). The SHG signal was calculated at twice the frequency of the fundamental, i.e. λ=425nm and 390 nm, respectively. The input polarization was selected along the x or y direction as depicted in Figure 4-1. The output SHG was averaged over the x,y,z directions.

4.2.4   Second harmonic generation microscopy

The nonlinear optical response from gold nano-prisms was measured using the second-harmonic generation microscopy set-up depicted in Figure 4-2.[51,52] The setup is based on a Nikon Eclipse TE2000-U inverted microscope, equipped with a 3D Piezosystem Jena 84641 scanner for image acquisition. The localized surface plasmon resonances were excited with a Spectra-Physics Mai-Tai Ti:Sa oscillator, emitting 100 fs pulses at 80 MHz repetition rate with a tunable fundamental wavelength ranging from 680 to 1020 nm.
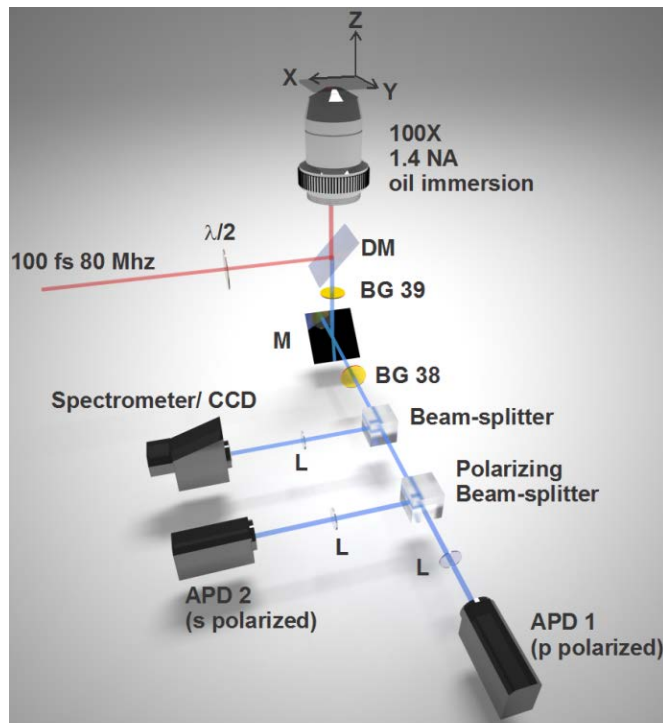
Figure 4-2: Experimental setup used for the polarized SHG measurements. APD (1 and 2): avalanche photodiodes; M: mirror; BG (38 and 39): interference filters; DM: Dichroic mirror; λ/2: half-wavelength plate at 800 nm

The laser beam was focused on the gold nano-prisms arrays by a high numerical aperture oil-immersion objective (Nikon 100x IR, N.A.=1.4), providing a diffraction-limited spatial resolution. The second harmonic generated photons were collected along the epi-direction through the same objective and separated spectrally from the NIR excitation beam using a dichroic mirror (AHF with a cut-off wavelength at 700 nm) and a short-pass filter (AHF, multiphoton-emitter HC 770/SP), as well as from eventual two-photon excited luminescence by a set of band-pass fluorescence filters. Polarization analysis was achieved by precise rotation of the achromatic half-wave plate in the excitation optical path. In the detection channel, the SHG signal is decomposed into s and p polarization components by a polarizing beam splitter, and detected by two silicon avalanche photodiodes (APD, Laser Components, Blue Counts) operating in the photon counting regime. The emission spectrum was obtained with an Oriel Multispec 7740 spectrometer (160 nm narrow slit), equipped with an Andor Technology DV420-OE CCD camera. The

raw data was duly corrected by the laser output power and the transmission characteristics of all optical components of the setup, as well as by the quantum efficiency of the APDs.

4.2.5 Lifetime imaging

Time-Correlated Single-Photon Counting (TCSPC) technique was used to discriminate SHG from TPPL, both emitted by the gold structures.[37,53] The setup for TCSPC was distinct from that of SHG microscopy and was based on a Leica SP2 microscope coupled to a single-photon counting module (PicoQuant-PicoHarp 300). The excitation source was a Ti:Sa laser emitting 150 fs pulses. The input polarization was fixed and set to the y direction with respect to the structures. The excitation wavelength was set to 800 nm. The temporal distribution of the counted photons at 400 nm of the emission wavelength was fitted by a single exponential function, $I_t = I_0 \exp(-t/\tau)$, where τ stands for the time constant associated with the lifetime of the excited state. For TPPL measurements a low-pass filter was used to eliminate all photons with wavelengths above 750 nm, while for SHG measurements a narrow band-pass filter centered at 400 nm (bandwidth 10 nm) was added.

4.3 Results and discussion

The SEM images shown in Figure 4-1 represent the sets of triangular gold nanoprisms used in this study. The experimental normalized and non-polarized extinction spectra of the investigated structures for gap distance varying from 0 nm to 100 nm are shown in Figure 4-3a. We clearly see from this figure that the extinction spectrum maximum shifts to the blue spectral range with increasing distances between gold nanoprisms from 0 nm to 100 nm by 25 nm step, which is a signature of the localized surface plasmon (LSP) coupling. The large spectral widths of the collected spectra are mainly due to the very short lifetime of plasmon excitations that results from very large ohmic losses. In the case of gold, these losses are larger at shorter wavelengths due to the interband transitions. Inhomogenous effects due to the variability of the structure geometry is also a source of spectral broadening.

To better understand the origin of our experimental observations, we performed FDTD simulations of the extinction spectra for the same gold triangular prism configurations with the same gap distances for an excitation wavelength spectral range varying from 500 nm to 900 nm (Figure 4-3b).
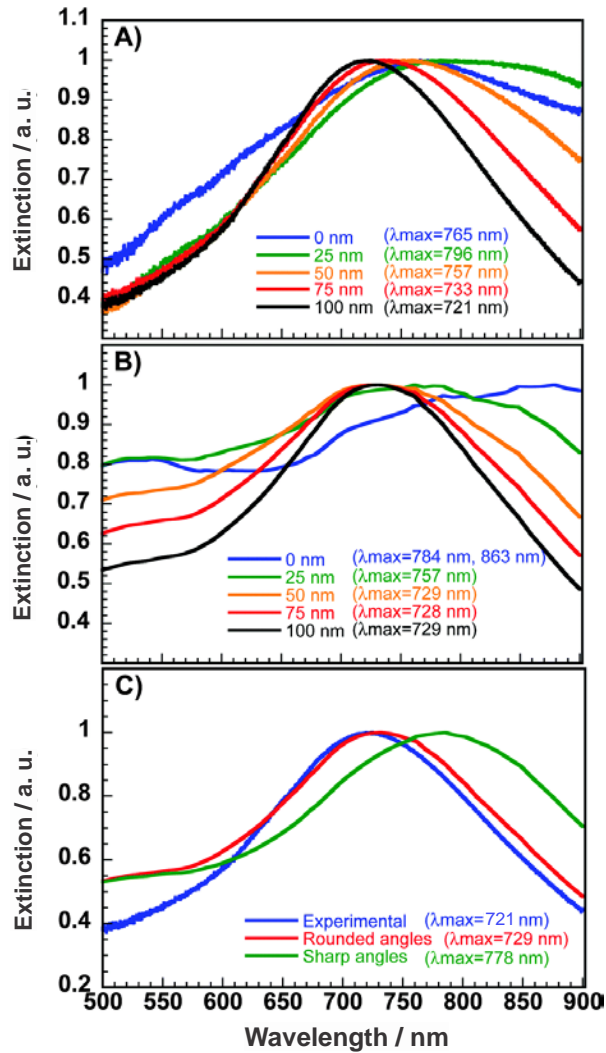
Figure 4-3: Normalized measured (a) and calculated (b) extinction spectra of the triangle patterns shown in colors for different gap distances. (c) Effect of the angle rounding on the calculated extinction spectra for patterns with a 100 nm gap.

The simulated results show good agreement with the experimental results, the same extinction spectrum maximum blue shift and similar spectrum profiles, except for the structure with no gap. In the case of gap-less structures, the discrepancy between the real

fabricated structure and idealized ones used for simulations is at its highest. In both experimental measurements and theoretical simulations, we observe the spectral broadening with decrease of the gap size between nanoprisms due to the coupling of plasmon resonances between single individual prisms. The absence of such spectral broadening at the blue spectral edge of the experimental extinction spectra is probably linked to experimental conditions: lower optical transmission in the visible spectral range as well as a lower detector sensitivity in this range. The observed tendency of the extinction spectrum change, namely a red shift, emitted intensity increase and spectrum broadening with decrease of the gap, results from an increase of the local free electron density concentration. Further consequences are lower plasmon resonance frequencies and higher emitted intensity due to the increased number of emitting oscillators. The broadening of the spectrum is then a result of the increased probability of involvement of higher order oscillating modes.[54] In FDTD calculations, it was crucial to round-off the apices of the individual triangles as shown in Figure 4-1 to closely reproduce the features of the e-beam fabricated samples. The impact of apices rounding is demonstrated in Figure 4-3c for nanoprisms structures with a 100 nm gap. The experimental result (red line) corresponds well to the simulated one for the cases of rounded angles (blue line). The simulated extinction curve for the case of the sharp angles (green line) is red-shifted by 66 nm with respect to the experimental curve (λ_{max}=720 nm). The results of simulation for sharp angles give the maximum of extinction spectrum at λ_{max}=786 nm while after rounding the apices, the extinction spectrum maximum shifts to λ_{max}=732 nm. Both, the experimental and the simulation results demonstrate the location of the extinction maximum in the 700-800 nm spectral region that varies in function of the gap width between the triangular nanoprisms. The obtained results clearly define the region of LSPRs that are important towards further structure investigation with methods of nonlinear optical spectroscopy and microscopy. These results evidence a strong dependence on sample geometry and on the distance between the investigated triangular nano-prisms.

To further probe the structures comprising three gold triangular nano prisms with variable gap sizes, second-harmonic generation measurements were performed using a tunable

femtosecond laser excitation. The second harmonic generation signal emitted from these structures was collected for an excitation wavelength varying between 750 and 960 nm and detected with two calibrated APDs assigned to the detection of the *p* and *s* polarized SHG as depicted in Figure 4-2 and further detailed in the experimental methods section. The integrated SHG signal was collected by raster-scanning a defined surface and then averaging the collected signal.

The variation of SHG intensity as a function of the excitation wavelength is shown in Figure 4-4 for a 100 nm gap distance. When approaching the LSPR maximum at 720 nm the SHG emission is strongly enhanced and is already one order of magnitude higher at 770 nm as compared to the SH intensity at 900 nm.
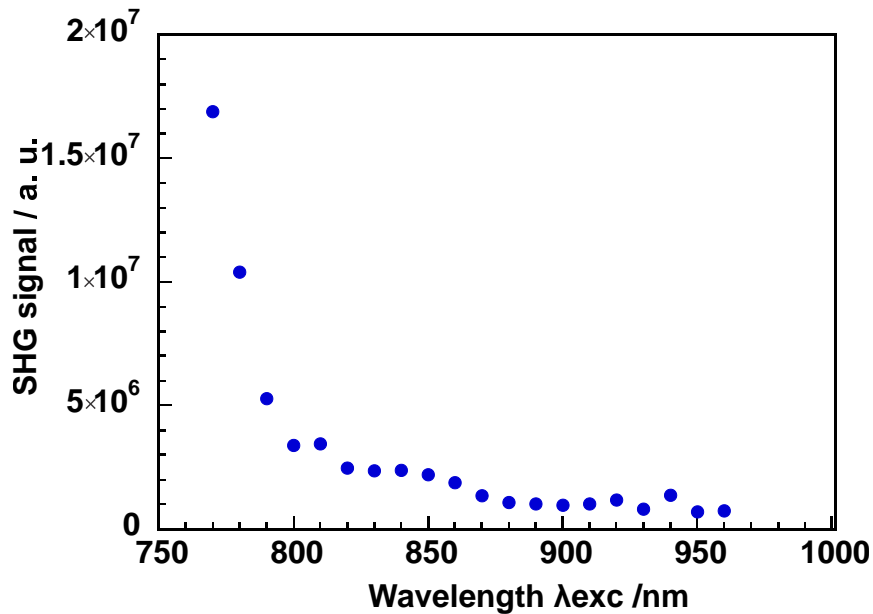
Figure 4-4: SHG spectrum of the set of three triangular gold nanoprisms with a 100 nm gap. The average excitation power was kept constant (50 μW) at the entrance of the microscope. The laser beam polarization was kept linear along the x-axis as depicted in Figure 4-1. The SHG spectrum was obtained by averaging the signal collected over a selected area. The SHG spectrum was corrected for the output optics transmission and for the APD's quantum efficiency.

It clearly points-out that the largest SHG response is obtained when the fundamental wavelength is matching the LSPR wavelength. Noticeably a weaker resonance is also observed for an excitation at 850 nm. This later resonance appears critical for the polar measurements performed on these structures. These measurements provide strong evidence for the coupling of second harmonic generation with localized surface plasmon excitation, opening the way to generating the desired SH signal by tailoring of the sample structure.

In order to investigate the nonlinear properties, polarization resolved two-photon confocal microscopy was used to spatially map the SHG response and measure the polarized patterns from individual nano-prisms.[51,52] Such mapping is done using point-by-point scanning with 20 nm steps along the x and y directions with image reconstruction based on the number of photons collected by the APDs. Examples of SHG images collected at 390 nm of some of the studied samples are shown in Figure 4-5 a-d. The nonlinear optical microscopy experiment provides enhanced spatial resolution that allows to distinguish signals from the individual triangular prisms as shown in Figure 4-5 a-d for small gaps with dimensions below 100 nm.[55] For a low excitation average power of 50 µW (λ=780 nm) at the sample, the signal originates from regions where SHG is enhanced through plasmon coupling. Such regions are characterized by their higher free electron density which increases the local electric field and therefore accounts for the onset of local peaks in the emitted SHG intensity. Both sets of prisms in Figure 4-5a clearly show three spots that confirm that the signal originates from triangle apexes.
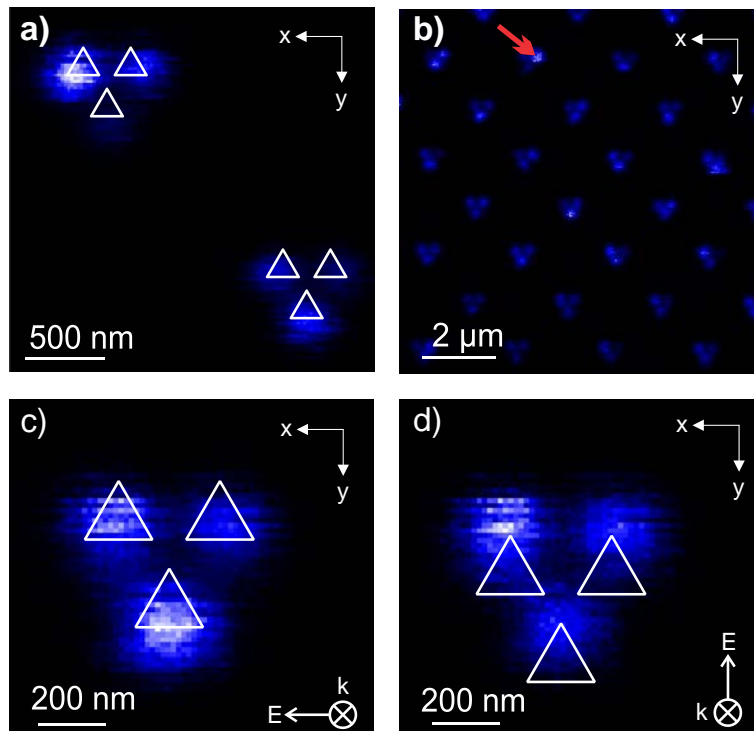
Figure 4-5: a) SHG image of two sets of non-centrosymmetric gold structures. For each set of three triangular nanoprisms (200 nm base dimension), the gap between the individual prisms was 100 nm. b) A larger region of sets of the triangular gold nanoprisms with 50 nm gap between nanoprisms. Each triangular nanoprism is distinguishable. The red arrow points-out at a significantly enhanced spot that may result from unexpected surface roughness. c, d) SHG images of the same set of three triangular gold nanoprisms obtained with x- and y- polarized excitation. The typical intensity at the sample was 50 μW at 780 nm.

It is noteworthy that the SHG intensities of the structures can vary from structure to structure due to a probable inhomogeneous distribution of the apex dimensions of the prisms.

As highlighted in Figure 4-5b, some prisms shows SHG confinement while others appear SHG inactive. Polarized measurements are represented in Figure 4-5c,d for horizontal (x) and vertical (y) polarization inputs, respectively. The detected SHG is the sum of the two APDs with polarization analyses along the x (s) and y (p) directions. In Figure 4-5 c,d are shown the SHG spatially resolved maps for both input polarization, and the triangular

structures have been depicted to scale to indicate the location of SHG activity. For a horizontal input polarization (Figure 4-5c), three SHG spots are observed and correspond to the bases of the prisms. For some structures, coupling between the bases of the two upper prisms yields a more elongated SHG activity along the x direction. When the excitation is switched to a vertical polarization, the three SHG spots correspond to the apices of the triangles as shown in Figure 4-5d.

Electromagnetic modeling on the same sets of nanoprisms for Horizontal and Vertical polarizations of input laser beam are shown in Figure 4-6 a-d and e-h for excitations wavelength set at 780 and 850 nm respectively.

Figure 4-6 a, b and e, f display the normalized polarized electric field distributions over a single structure at 780 nm and 850 nm excitation wavelengths, respectively, while Figure 4-6 c, d and Figure 4-6 g, h show the polarized distributions at 390 and 425 nm, respectively. Control via polarization of the excitation allows to selectively excite localized plasmons at the distinct directions of the triangular structures (Figure 4-6 a, b, e, f,). For both polarizations and both fundamental wavelengths, an enhancement of the electric field by a factor of ~10 is observed in the vicinity of the apexes of the triangular nanoprisms. Confinement of the SHG at the apices of the triangles is also observed for the second harmonic at 390 and 425 nm, but interestingly the confinement of the SHG at the apices is more prominent at 425 nm (Figure 4-6 g, h) while delocalization of the SHG is observed along the edges of the prisms at 390 nm. Furthermore, the control over the polarization of the excitation allows one to control the position of the resonance at the base of the triangle (x-polarized input) or at the upper apex (y-polarized input) thus yielding distinctive spatial plasmon coupling of the individual structures for both selected polarizations. Remarkably, the obtained images of the electric near-field distribution demonstrate excellent correlation between the observed SHG images reported in Figure 4-5 c, d and the electric charges distribution. It can be inferred therefrom that for a vertical polarization, charges are accumulating in the apices of triangles, whereas for a horizontal one, they concentrate in the base angles.

Indeed, calculations for the electric field performed at 390 nm (Figure 4-6 c, d) and 425 nm (Figure 4-6 g, h) confirm the agreement between the observed SHG and LSPR generation. Here again, SHG localization is expected to take place at the apices of the triangles and depends on the input polarization.

Note that in Figure 4-6 c, d, g, h, the non-normalized SHG emission can be correlated with the location of the LSP at 780 and 850 nm. The excitation of the LSP of a metallic feature deprived of centre of symmetry yields efficient SHG that is originating from the same local area as that of the fundamental LSP resonance. The deviations in our observed SHG images from predictions of simulations can be accounted for by the deviation of the real sample geometry from its ideal shape, whereas the observed surface heterogeneities could be ascribed to the surface roughness.
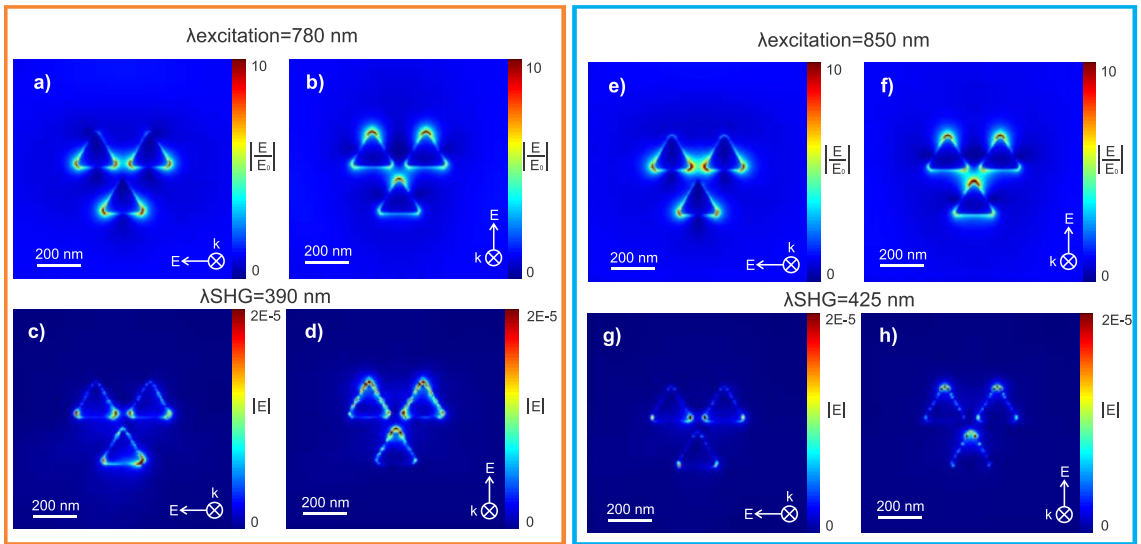
Figure 4-6: Calculations of the electric field distributions in the vicinity of the gold nanostructures using FDTD calculations. a) Normalized electrical field $|E/E_0|$ at $\lambda_{excitation}$=780 nm with x-polarized input. b) Normalized electrical field $|E/E_0|$ at $\lambda_{excitation}$=780 nm with y-polarized input. Non-normalized SHG electrical field $|E|$ calculated at 390 nm for x- (c) and y- (d) polarizations. e) Normalized electrical field $|E/E_0|$ at $\lambda_{excitation}$ =850 nm with x-polarized input. f) Normalized electrical field $|E/E_0|$ at $\lambda_{excitation}$ =850 nm with y-polarized input. Non-normalized SHG electrical field $|E|$ calculated at 425 nm for x- (g) and y- (h) polarizations.

Even though EBL provides good homogeneity for nanofabrication, some individual structures appear to be more active presumably due to some local defects responsible for further free electron density increase, thereby enhancing the SHG response. Another possible explanation is the role of the surface roughness associated with the electron-beam evaporation of gold. A measured roughness of 1 nm RMS may be responsible for surface effects that can yield hot-spot areas. A similar phenomenon was reported earlier.[41]

4.3.1 Second harmonic generation and two-photon photo-luminescence.

As was mentioned in our introduction, SHG on gold nanostructures is not the only effect enhanced by LSPRs. In particular, two-photon photo-luminescence produced a strong signal (Figure 4-7a). This figure shows a strong TPPL overall signal, which could be used for nanostructure visualization and LSPR distribution analysis. An interesting feature is the strong TPPL increase in the longer wavelength part of the spectrum. When SHG was measured, the then spurious TPPL signal was cut off by the band-pass filter.
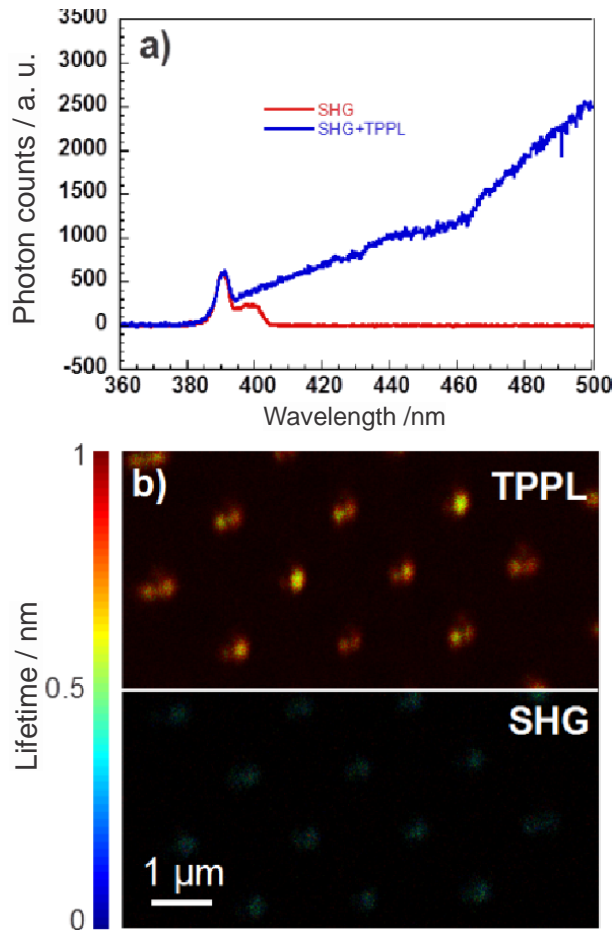
Figure 4-7: a) SHG spectrum (in red) obtained with a band-pass filter and the convolved spectrum of the SHG and TPPL (in blue) obtained without band-pass filter. b) Combined lifetime images of TPPL signal (upper half) and SHG signal (lower half) from three touching triangular gold nanoprisms (0 nm gap distance). The color-coded lifetime values of the two signals differ drastically highlighting the distinct nature of both phenomena. The input light polarization was set along the y-axis while no analyzer was used.

The two complementary SHG and TPPL signals could be temporally separated and analyzed in parallel channels, so as to combine the respective information and identify the excited LSPR. Lifetime imaging maps associated with the TPPL and SHG processes are displayed in Figure 4-7b for gap-less triangular gold nano-prisms set. The color-

coded maps present the distribution of lifetimes associated with TPPL and SHG. As expected the lifetimes associated with TPPL is much longer than those for SHG. TPPL is a resonant absorption process yielding incoherent emission with a typical lifetime of 10^{-9} s while SHG is a coherent process occurring quasi-instantly within a few fs.[56] Analysis of the collected lifetimes resulted in $\tau=0.8$ ns for the TPPL decay while the signal measured at short time was associated with SHG and could not be resolved dynamically due to limited instrumental response. The strength of the signal is much weaker for SHG compared to TPPL as seen in Figure 4-7b. The TPPL intensity appears to surpass that of SHG by two orders of magnitude. The TPPL and SHG maps do not provide sufficient spatial resolution to directly correlate the topographical features with measured signals. The two processes are both occurring under femtosecond irradiation and it is therefore critical to ensure their separation via adequate detection.

4.3.2   Nonlinear polarization properties of nano-prisms.

In order to provide information on the symmetry and tensor properties of the fabricated nanostructures, nonlinear polarization measurements were performed. The sample was excited by linearly polarized 850 nm and 780 nm femtosecond laser pulses, at an average incident power of 2 mW, and the SH emissions at 425 nm and 390 nm, respectively, acquired along the x and y orthogonal directions by a set of two avalanche photodiodes. The 425 nm generated harmonic wavelength can be considered as off resonance with the gold plasmon, conversely to the 390 nm harmonic wavelength which is partially resonant. A 0.2 low NA objective of x10 magnification was used, so as to minimize the longitudinal z axis contributions, and mainly probe the in-plane susceptibility tensor components, thus facilitating the recognition of the basic three-fold symmetry features of the nanostructure from the characteristic cross-shape of the polarized SHG plots along X and Y. Measurements were performed for individual structures with a gap size of 25 nm at locations well within the array (e.g. at a few tens of microns away from the edge corner of the array). The excitation polarization was rotated over a full 360° period, yielding the two simultaneously acquired X and Y polar plots. As can be seen from Figure 4-8a and 8b for the X and Y polarization directions the SHG polar plots measured at 425 nm

clearly feature four-lobes patterns for the three different gap sizes, which are indicative of three-fold symmetry.[36,37,52] These are more pronounced for the X harmonic polarization than for the Y one, which may be ascribed to a minor built-in fabrication asymmetry, such as would correspond to a slight symmetry lowering from full equilateral triangle features symmetry onto a isosceles-like deformation. Indeed, one cannot guarantee the perfect symmetry for the central 25 nm edge-to-edge gap which is due to play a highly sensitive role in the plasmonic mode spatial distribution by providing coupling space to the sub-unit localized modes. In addition, one cannot rule-out a minor off-axis centering along the Y axis that would also lead to a small deviation from the expected four-fold pattern of the Y polarized emission. Finally, another cause for this asymmetry could be the spatial averaging of near-field fluctuations of the LSPR[57] which can occur over the time-scale of SHG emission.[58]

We also show on Figure 4-8c and 8d SHG polarization plots now measured at 390 nm, that are in partially resonant conditions under excitation at 780 nm (see Figure 4-4). The four-fold symmetry pattern disappears, letting way to a lower symmetry plot that features only two lobes pointing towards opposite directions at 30° and 210°. This symmetry lowering effect may be linked to additional susceptibility terms which do not abide to Kleinman index permutation due to resonant and thus dispersive contributions to the susceptibility tensor, such as $\chi^{(2)}_{yxx} \neq \chi^{(2)}_{xyx}$.
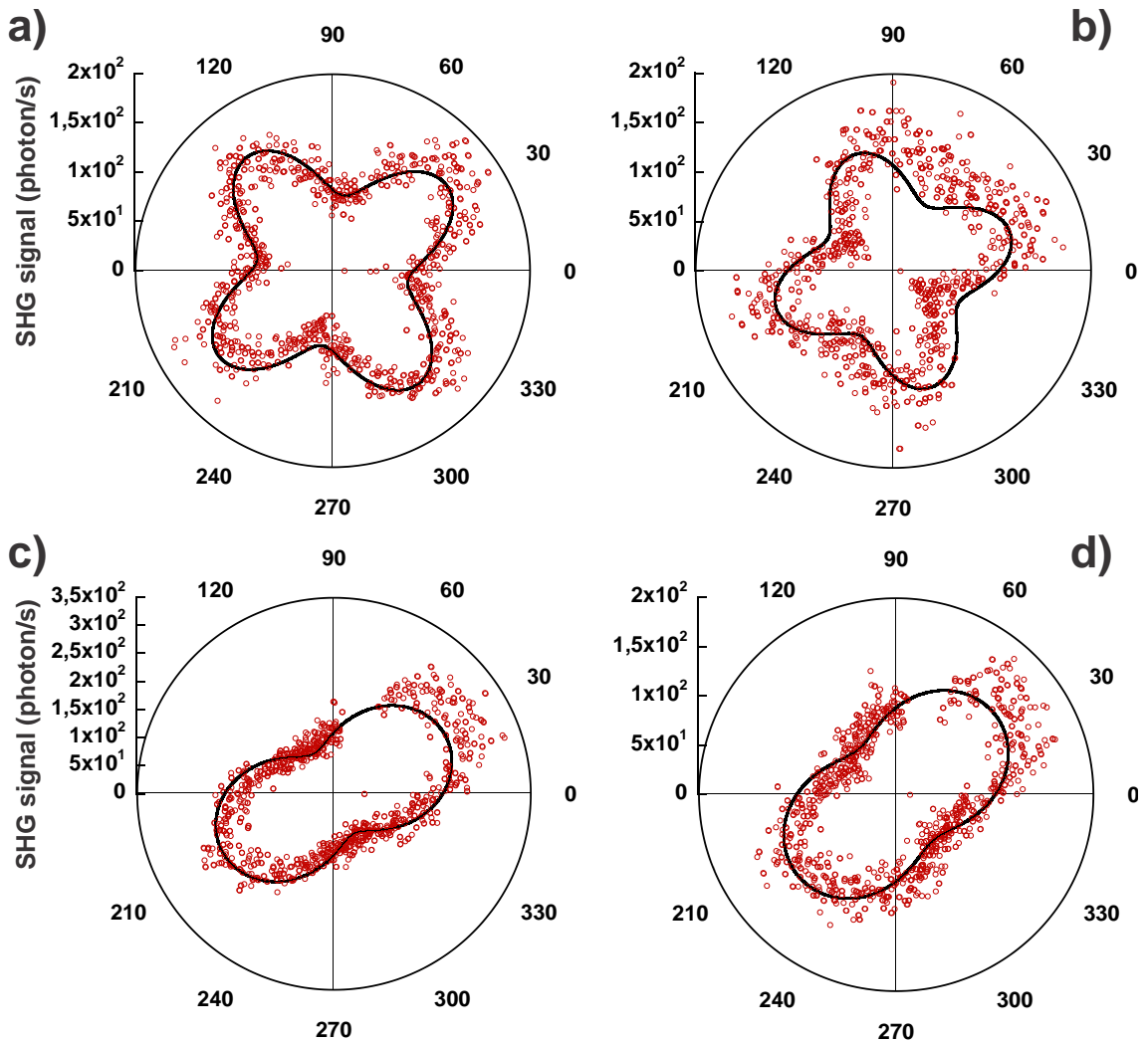
Figure 4-8: Polar representations of the experimental polarization-resolved SHG response analyzed along the X and Y directions corresponding to s and p polarizations in the detection plane for three-fold gold structures with an inter-triangle distance of 25 nm. (a,b) fundamental wavelength : 850 nm in non-resonant conditions, featuring well resolved cross-like patterns characteristic of the incidence on SHG of structural 3-fold symmetry, when analyzed along x- (a) and y- (b) in-plane directions. (c,d) fundamental wavelength: 780 nm closer to resonance conditions and thus losing pronounced symmetry features associated to Kleinman index permutation symmetry. SHG is analyzed along the x-(c) and y-(d) in-plane directions. The solid curves are guides to the eyes.

To the best of our knowledge, such feature and its analysis have not been reported before and are currently under further investigation from the different perspective of nonlinear spectroscopy of plasmonic nanostructures, complementary to the structural investigation reported herein where off-resonance conditions are being preferred. As far as structural studies are considered, while being accessible, the precision required to ensure reproducibility of e-beam fabrication process remains a technological challenge in particular with features in the 10-20 nm range.

4.4   Conclusions

We have investigated the gap dependent variations of quadratic nonlinear properties in newly designed non-centrosymmetric arrangements of triangular gold nano-particles. The nonlinear properties of these meta-molecules were investigated by second-harmonic microscopy and confronted to electromagnetic simulations. The role of the underlying localized resonances and of the attached localized reinforcement spots for the fundamental and harmonic fields could be identified. Polarization dependence of the SHG response reveals typical four-lobes patterns which can be assigned to structures with three-fold symmetry, thus highlighting the symmetry-dependence of the collected SH signal. Time-dependent photon counting measurements lead to a longer life-time for two-photon fluorescence as compared to SHG, respectively in the nano-second versus femtosecond range, in-keeping with an effective excited state population for TPPL. Finally, meta-molecules in the 500 nm overall dimension range clearly exhibit the underlying individual nano-triangles in the form of well separate entities, in keeping with a SHG imaging set-up close to diffraction limit. More work will be needed to clearly evidence the optimal distance between individual nano-triangles, eventually leading to a maximal SHG efficiency. This will require further developing fabrication steps allowing for the control of gaps between nano-triangles, in a critical range-in-between 20 nm and a few nanometers. Whereas nano-cavities exhibit optimal coupling distances in the range of a few 100 nm,[40,43] nanoparticles need to be in closer vicinity to allow for optimal Van-Der-Waals-like coupling between localized plasmons, in the absence of propagative modes in-between. Therefore, combining nano-cavities for long distance interaction (e.g. in the few 100 nm range) with nano-particles tailored for evanescent gap coupling (e.g. in

the few nm range) might lead in the future to more advanced meta-entity coupling schemes, whereby short distance coupling would be ensured by meta-molecular gathering of nano-particle building blocks, whereas longer distance interactions would be sustained by molecular assemblies now based on nano-cavities. Such multi-scale design rules could be advantageous applied in novel nano-plasmonic based biochips, towards sensitive and specific (e.g. local) detection of traces of targeted biomolecules. The sensitive detection part could be ensured by nano-particle based meta-molecules, playing on the small gap in-between nano-building blocks, whereas further propagation of the signal would be ensured by nano-cavity based entities with a longer interaction range.

4.5 References

(1) Park, S.; Won Hahn, J. *Opt. Express.* **2009**, *17*, 20203-20210.

(2) Mansuripur, M.; Zakharian, A. R.; Lesuffleur, A.; Oh, S. H.; Jones, R. J.; Lindquist, N. C.; Im, H.; Kobyakov, A.; Moloney, J. V. *Opt. Express.* **2009**, *17*, 14001-14014.

(3) Li, X. P.; Lan, T. H.; Tien, C. H.; Gu, M. *Nat. Commun.* **2012**, *3*, 998.

(4) Guo, Y. G.; Hu, J. S.; Wan, L. J. *Adv. Mater.* **2008**, *20*, 4384-4384.

(5) Zijlstra, P.; Chon, J. W. M.; Gu, M. *Nature.* **2009**, *459*, 410-413.

(6) Large, N.; Aizpurua, J.; Lin, V. K.; Teo, S. L.; Marty, R.; Tripathy, S.; Mlayah, A. *Opt. Express.* **2011**, *19*, 5587-5595.

(7) El-Sayed, I. H.; Huang, X. H.; El-Sayed, M. A. *Nano Lett.* **2005**, *5*, 829-834.

(8) Loo, C.; Hirsch, L.; Lee, M.-H.; Chang, E.; West, J.; Halas, N.; Drezek, R. *Opt. Lett.* **2005**, *30*, 1012-1014.

(9) Gobin, A. M.; Lee, M. H.; Halas, N. J.; James, W. D.; Drezek, R. A.; West, J. L. *Nano Lett.* **2007**, *7*, 1929-1934.

(10) Halas, N. J.; Lal, S.; Chang, W.-S.; Link, S.; Nordlander, P. *Chem. Rev.* **2011**, *111*, 3913-3961.

(11) Prodan, E.; Radloff, C.; Halas, N.; Nordlander, P. *Science.* **2003**, *302*, 419-422.

(12) Ko, K. D.; Kumar, A.; Fung, K. H.; Ambekar, R.; Liu, G. L.; Fang, N. X.; Toussaint, K. C. *Nano Lett.* **2011**, *11*, 61-65.

(13) Benedetti, A.; Centini, M.; Bertolotti, M.; Sibilia, C. *Opt. Express.* **2011**, *19*, 26752-26767.

(14) Kim, S.; Piao, L.; Han, D.; Kim, B. J.; Chung, T. D. *Adv. Mater.* **2013**, *25*, 2056-2061.

(15) Kim, T.; Jeon, K. S.; Heo, K.; Kim, H. M.; Park, J.; Suh, Y. D.; Hong, S. *Analyst.* **2013**, *138*, 5588-5593.

(16) Chen, C. Y.; Wang, J. Y.; Tsai, F. J.; Lu, Y. C.; Kiang, Y. W.; Yang, C. C. *Opt. Express.* **2009**, *17*, 14186-14198.

(17) Cui, B.; Clime, L.; Li, K.; Veres, T. *Nanotechnology.* **2008**, *19*, 145302.

(18) Moran, A. M.; Sung, J.; Hicks, E. M.; Van Duyne, R. P.; Spears, K. G. *J. Phys. Chem. B.* **2005**, *109*, 4501-4506.

(19) Merlen, A.; Lagugné-Labarthet, F. *Appl. Spectrosc.* **2014**, *68*, 1307-1326.

(20) Ray, A.; Lee, Y. E.; Kim, G.; Kopelman, R. *Small.* **2012**, *8*, 2213-2221.

(21) Zhang, S.; Park, Y. S.; Li, J.; Lu, X.; Zhang, W.; Zhang, X. *Phys. Rev. Lett.* **2009**, *102*, 023901.

(22) Valev, V. K.; Clercq, B. D.; Zheng, X.; Denkova, D.; Osley, E. J.; Vandendriessche, S.; Silhanek, A. V.; Volskiy, V.; Warburton, P. A.; Vandenbosch, G. A.; Ameloot, M.; Moshchalkov, V. V.; Verbiest, T. *Opt. Express.* **2012**, *20*, 256-264.

(23) Kolkowski, R.; Petti, L.; Rippa, M.; Lafargue, C.; Zyss, J. *ACS Photonics.* **2015**, *2*, 899-906.

(24) Cinel, N. A.; Butun, S.; Ozbay, E. *Opt. Express.* **2012**, *20*, 2587-2597.

(25) Schrof, W.; Rozouvan, S.; Keuren, E. V.; Horn, D.; Schmitt, J.; Decher, G. *Adv. Mater.* **1998**, *10*, 338-341.

(26) Butet, J.; Brevet, P.-F.; Martin, O. J. F. *ACS Nano.* **2015**, *9*, 10545-10562.

(27) Bouhelier, A.; Beverluis, M.; Hartschuh, A.; Novotny, L. *Phys. Rev. Lett.* **2003**, *90*, 013903.

(28) Ropers, C.; Solli, D. R.; Schulz, C. P.; Lienau, C.; Elsaesser, T. *Phys. Rev. Lett.* **2007**, *98*, 043907.

(29) Shen, Y.-R. *The principles of nonlinear optics*; Wiley-Interscience: New York, 1984.

(30) Ahmadi, A.; Ghadarghadr, S.; Mosallaei, H. *Opt. Express.* **2010**, *18*, 123-133.

(31) Tabatabaei, M.; Sangar, A.; Kazemi-Zanjani, N.; Torchio, P.; Merlen, A.; Lagugné-Labarthet, F. *J. Phys. Chem. C.* **2013**, *117*, 14778-14786.

(32) Bar-Ilan, O.; Albrecht, R. M.; Fako, V. E.; Furgeson, D. Y. *Small.* **2009**, *5*, 1897-1910.

(33) Liu, N.; Pucci, A. *Nat. Mater.* **2012**, *11*, 9-10.

(34) Yanik, A. A.; Huang, M.; Kamohara, O.; Artar, A.; Geisbert, T. W.; Connor, J. H.; Altug, H. *Nano Lett.* **2010**, *10*, 4962-4969.

(35) Alkilany, A. M.; Murphy, C. J. *J. Nanopart. Res.* **2010**, *12*, 2313-2333.

(36) Viarbitskaya, S.; Teulle, A.; Marty, R.; Sharma, J.; Girard, C.; Arbouet, E.; Dujardin, E. *Nat. Mater.* **2013**, *12*, 462-463.

(37) Deng, H. D.; Li, G. C.; Dai, Q. F.; Ouyang, M.; Lan, S.; Trofimov, V. A.; Lysak, T. M. *Nanotechnology.* **2013**, *24*, 075201.

(38) Mooradian, A. *Phys. Rev. Lett.* **1969**, *22*, 185-187.

(39) Zyss, J. *J. Chem. Phys.* **1993**, *98*, 6583-6599.

(40) Kolkowski, R.; Szeszko, J.; Dwir, B.; Kapon, E.; Zyss, J. *Opt. Express.* **2014**, *22*, 30592-30606.

(41) Salomon, A.; Zielinski, M.; Kolkowski, R.; Zyss, J.; Prior, Y. *J. Phys. Chem. C.* **2013**, *117*, 22377-22382.

(42) Schön, P.; Bonod, N.; Devaux, E.; Wenger, J.; Rigneault, H.; Ebbesen, T. W.; Brasselet, S. *Opt. Lett.* **2010**, *35*, 4063-4065.

(43) Salomon, A.; Prior, Y.; Fedoruk, M.; Feldmann, J.; Kolkowski, R.; Zyss, J. *J. Opt.* **2014**, *114012*.

(44) Manheller, M.; Trellenkamp, S.; Waser, R.; Karthauser, S. *Nanotechnology.* **2012**, *23*.

(45) Papadopoulos, A. D.; Glytsis, E. N. *Appl. Optics.* **2010**, *49*, 5787-5798.

(46) Kim, R. S.; Zhu, J.; Park, J. H.; Li, L.; Yu, Z.; Shen, H.; Xue, M.; Wang, K. L.; Park, G.; Anderson, T. J.; Pei, Q. *Opt. Express.* **2012**, *20*, 12649-12657.

(47) Raulot, V.; Gerard, P.; Serio, B.; Flury, M.; Kress, B.; Meyrueis, P. *Opt. Express.* **2010**, *18*, 17974-17982.

(48) Wang, F. X.; Rodriguez, F. J.; Albers, W. M.; Ahorinta, R.; Sipe, J. E.; Kauranen, M. *Phys. Rev. B.* **2009**, *80*, 233402.

(49) Krause, D.; Teplin, C. W.; Rogers, C. T. *J. Appl. Phys.* **2004**, *96*, 3626-3634.

(50) Berline, I.; Fiorini-Debuisschert, C.; Royal, C.; Douillard, L.; Charra, F. *J. Appl. Phys.* **2008**, *104*, 103113.

(51) Brasselet, S.; Le Floc'h, V.; Treussart, F.; Roch, J.-F.; Zyss, J.; Botzung-Appert, E.; Ibanez, A. *Phys. Rev. Lett.* **2004**, *92*, 207401.

(52) Le Floc'h, V.; Brasselet, S.; Roch, J.-F.; Zyss, J. *J. Phys. Chem. B.* **2003**, *107*, 12403-12410.

(53) Wang, T. Y.; Halaney, D.; Ho, D.; Feldman, M. D.; Milner, T. E. *Biomedical Optics Express.* **2013**, *4*, 584-595.

(54) Morarescu, R.; Shen, H.; Vallée, R. A. L.; Maes, B.; Kolaric, B.; Damman, P. *J. Mater. Chem.* **2012**, *22*, 11537-11542.

(55) Lagugné-Labarthet, F.; Shen, Y. R. In *Optical Imaging and Microscopy*; Török, P., Kao, F.-J., Eds.; Springer: Berlin Heidelberg, 2007; Vol. 87, p 237-268.

(56) Imura, K.; Nagahara, T.; Okamoto, H. *J. Phys. Chem. B.* **2005**, *109*, 13214-13220.

(57) Anceau, C.; Brasselet, S.; Zyss, J.; Gadenne, P. *Opt. Lett.* **2003**, *28*, 713-715.

(58) Stockman, M.; Bergman, D.; Brasselet, S.; Zyss, J. *Phys. Rev. Lett.* **2004**, *92*, 57402.

Chapter 5

5 Construction of a Second Harmonic Generation (SHG) microscopy Apparatus

Second harmonic generation microscopy (SHGM) is of great interest due to its sensitivity to surface anisotropy and non-centrosymmetric materials, i.e. materials with crystalline structures that do not have center of inversion. In this thesis, we have made use of a tunable home built SHG microscope developed at Ecole Normale Supérieure de Cachan in the group of Professor J. Zyss. The results using this setup were published and are summarized in chapter 4 of this thesis. From this first series of experiments, the Lagugné's group wished to pursue such experiments and to build a SHG microscope enabling more flexibility regarding the control over the excitation and collection polarizations. Building our own setup together with the associated software will permit to carefully select the parameters of choice to run a SHG map together with full control of the polarization parameters.

In this chapter, we focus on the details of the design and the construction of a SHG microscope now running in the Lagugné's group. The specifications of hardware as well as the software are provided with for future maintenance and use by members of the Lagugné's group.

5.1   SHG microscope : Design and Components

The expertise of Lagugné's group in optical microscopy and its combination with spectroscopy methods has led us towards the full design and fabrication of a SHG microscope. Before starting this project, the starting elements in our possession were a femtosecond light source (tunable between 700 to 900 nm), a series of high end microscopes objective, and two avalanche photodiodes. These are essential elements of microscopy optical measurements and probably the most costly elements. The addition of a precise sample stage, a series of optical components such as beam splitters, polarizers, dichroic mirrors, filters and observation camera was thus necessary to finalize our

project. The setup was based on the setup used at ENS Cachan although we made the choice of avoiding using a commercial microscope body and building it ourselves.
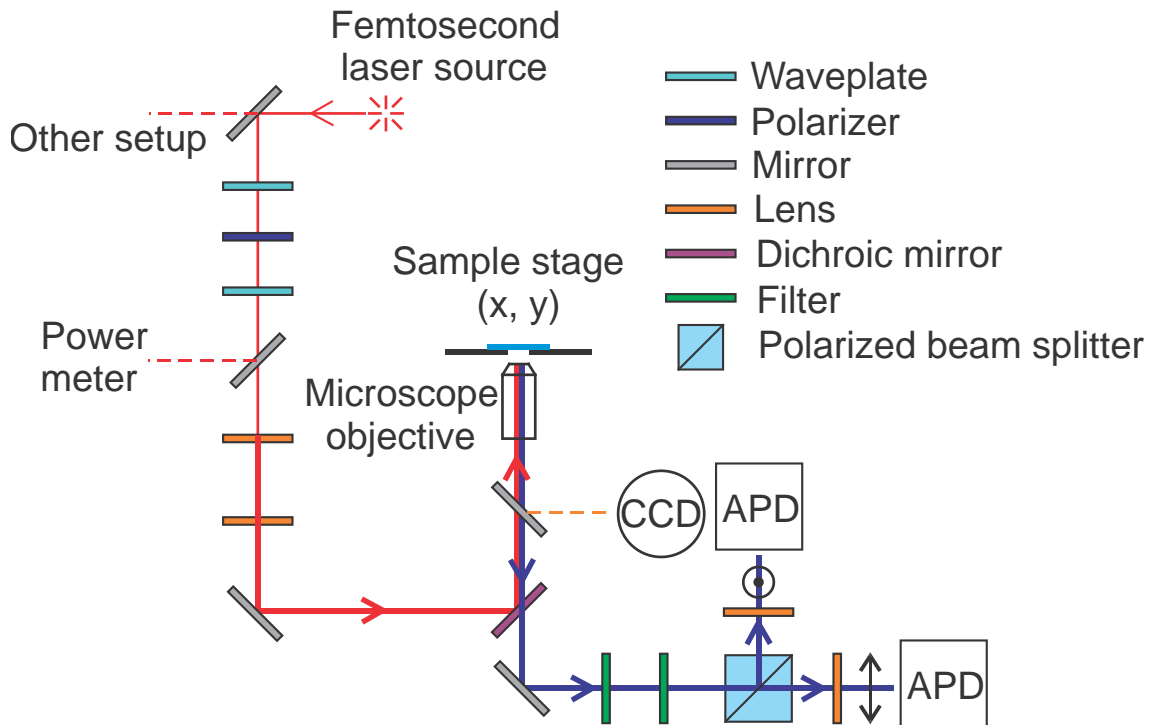
Figure 5-1: Schematic of the optical layout of the SHG microscope.

The basic principle of second harmonic generation microscope is simple: an excitation laser is focused onto the sample and the collected signal is collected by the same microscope objective, filtered through a dichroic mirror and detected. However, as mentioned in the previous chapter, SHG is a weak process which requires optimization of every optical component and optomechanical components for sake of optical stability. In order to achieve a spatial resolution close to the Abbe's criterion, i.e. the spatial resolution is limited to $\lambda/2$ where λ is the incoming light, the quality of the optical components and resulting alignment are critical. The signal/noise ratio can also be significantly improved in terms of the laser source, signal separation and detection. Figure 5-1 represents the general schematic of the SHG microscope initially designed. The whole system can be broken down to three parts: the laser excitation and polarization control, sample irradiation and signal collection and acquisition.

5.1.1　Laser excitation

The purpose of this part is to tune the fundamental wave. The 800 nm fundamental needs to be adjusted to the right intensity or power. The polarization is also a parameter needs to be considered and controlled, as well as the diameter of our fundamental wave.

The excitation source of this microscope is a commercial available Coherent Mira 900F (<200 fs pulse duration, 76 MHz repetition rate) Mode-locked Ti:Saphire laser (Figure 5-2a, Component 1). In this system the pump laser is a diode-pumped Coherent Verdi V-5. In the Verdi V-5, the 1064 nm emission is converted to 532 nm through frequency doubling by using a lithium triborate (LBO) crystal. The Mira 900F works at 800 nm wavelength with a tunable range from 700 to 980 nm. The beam diameter is 0.8 mm and maximum output power is 1W at the laser exit once the laser is stabilized.
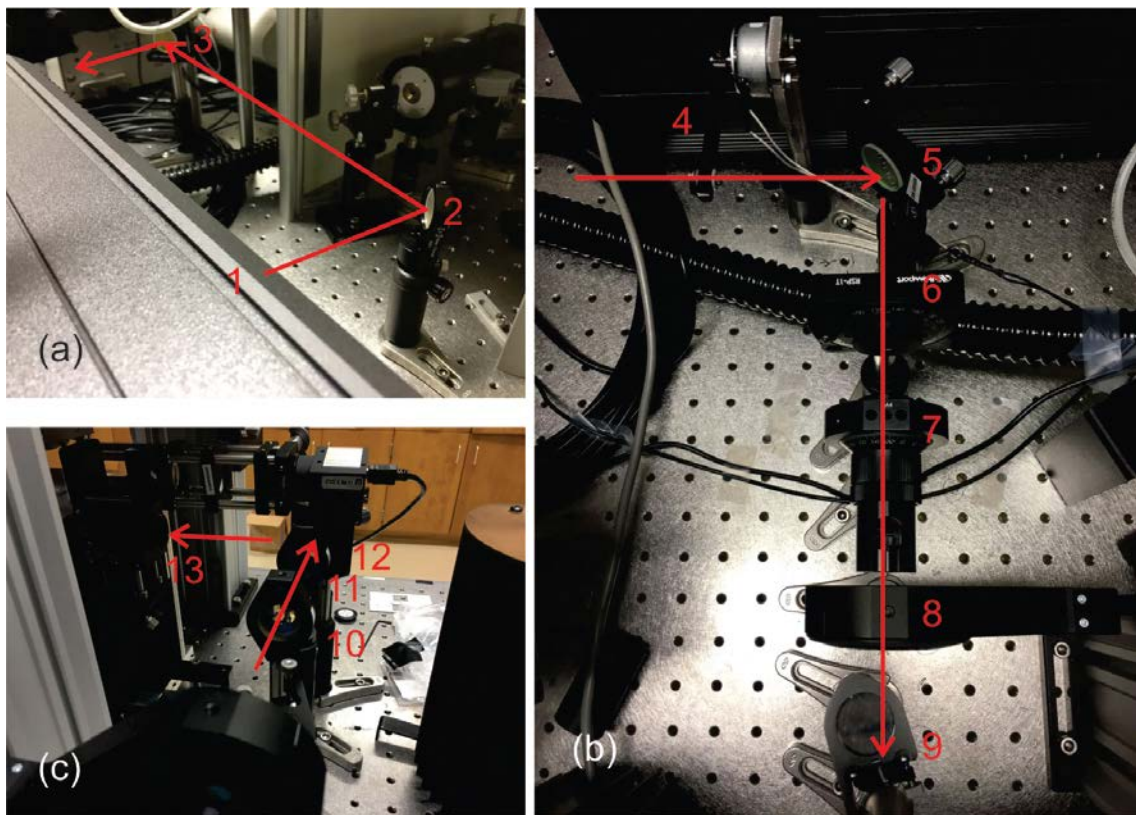
Figure 5-2: Photo of the laser intensity and polarization optical elements prior entrance to the SHG microscope

Dual Band 400 nm and 800 nm mirrors (Thorlabs, UFM10R, Component 2, 3, 5, 12 in Figure 5-2) were selected to guide the laser to the sample. The reflectance of such mirrors is >98% for any polarization at both 400 nm and 800 nm. The high reflectance and laser damage threshold (LDT) makes it a perfect mirror for reflecting the high intensity femto-second laser. The initial mirror was mounted on a flipper optic mount (Newport, 9891) in order to select one of the two microscope setup located on our optical table. The flipper mount ensures a safe and stable switch the laser path. When the mirror is up straight, the femto-second laser is introduced into the SHGM setup. By tilting two mirrors (Figure 5-2, Component 3 and 5), the height of the laser was raised from 120 mm to 153 mm, in order to match the proper height of our setup. After mirror 5, the laser is parallel to the optical table. A home-made shutter (Figure 5-2, Component 4) was used to block the laser. The shutter was connected to a BNC cable and could be manually or computer controlled. By providing a DC voltage above 1V, the shutter will be switched to ON state, meaning it will let laser go through. Normally the voltage was kept under 5V to ensure that there is no possible overloading of the circuits.

A combination of two half-wave plates and a polarizer is used to control the intensity and polarization of the 800 nm fundamental wave. The first wave-plate is a zero-order quartz half-wave plate (Newport, 05RP02-46, Component 6), optimized for 800 nm. This zero-order wave plate is constructed of two quartz plates, air-spaced to allow for use with high-power lasers, in a standard 12.7 diameter housing. The wave-plate is mounted on a 360 degree continuous rotation stage (Newport, RSP-1T), which provides smooth and continuous angular position. This mount cannot be controlled electronically but only tuned by hand. Since the laser generated from the Mira 900F is linear polarized horizontally, this wave-plate will help rotate the polarization by 2α, once the waveplate is rotated by an angle of α. Glan-laser calcite polarizer (Newport, 10GL08AG.16, Component 7) was used to control the intensity of the laser. According to Malus' law, if the angle between the polarization and polarizer is θ, the intensity after the polarizer is described as $I = I_0 \cos^2 \theta$, while I_0 stands for the intensity before entering the polarizer. This Glan-laser calcite polarizer is optimized from 650 to 1000 nm. The damage threshold is 500 W/cm^2, or 2 J/cm^2 with 10 ns pulses. This polarizer is fixed at horizontally polarized, meaning the polarization of the fundamental wave is parallel to

optical table. The role of this first pair of waveplate/polarizer is to set the intensity of the laser to a desired value. In order to electronically control the polarization state of the input light, a second zero-order half-wave plate (Thorlabs, WPH05M808, Component 8) which mounted on a motorized optical mount (Thorlabs, PRM1Z8E) was used. The crystalline quartz wave-plate's AR coating is at 808 nm, which is not exactly 800 nm but it shows a 0.11% reflectance at 800 nm. The retardance is 0.5043 waves at 801.52 nm and LDT is 10 J/cm^2 for 810 nm, 10 ns pulse laser. The motorized precision rotation stage controlled with a Thorlabs T-Cube DC Servo Motor Controller (Thorlabs, TDC001), provides an ideal and smooth continuous motion of the half waveplate providing a full control of the input polarization that is further controlled via a LabVIEW interface which will be described later in this chapter.

Once the laser excitation is modified to the desired power and polarization, the power of the laser can be checked by a power meter. A silver coated mirror (Component 9) was mounted onto a flipper optical mount to lead the laser into a power meter.

Since the beam diameter is reported to be 0.8 mm for the femto-second laser, the laser beam needs to be expanded to make sure it fully fills the back entrance of our microscope objective. The beam expansion was achieved by using a pair of lens. A N-BK7 Plano-Concave lens (Newport, KPC043AR16, Component 10), with an effective focal length - 25 mm was used to diverge the laser beam. A similar convex lens (Newport, KPX094AR.16, Component 11) was placed exactly 75 mm after the concave lens, to create an expanded and parallel laser beam. Both of these two lenses have anti-reflection coating to operate in the 650-1000 nm spectral range with less than 0.5% reflectance per optical element at 800 nm. The laser is expanded to a diameter of ~0.9 cm. A shear plate was used to confirm that the beam is parallel after the convex lens. Since we've already optimized the fundamental laser beam at the perfect intensity, polarization and diameter, the laser was reflected by another dual band 400 nm and 800 nm mirror into the sample irradiation part explained in the following paragraph. Further, the beam width was controlled by an adjustable pinhole (Component 13).

5.1.2 Sample irradiation

After the fundamental beam is properly modified, an optomechanical system was designed to guide the fundamental wave and focus that onto the sample. Also, this part includes the control of a high-accuracy positioning stage to enable mapping of a given sample with high precision and reproducibility, but also to selectively focus the fundamental onto a single spot in a stable environment. A dichroic mirror was used to separate the fundamental and the second harmonic beams.
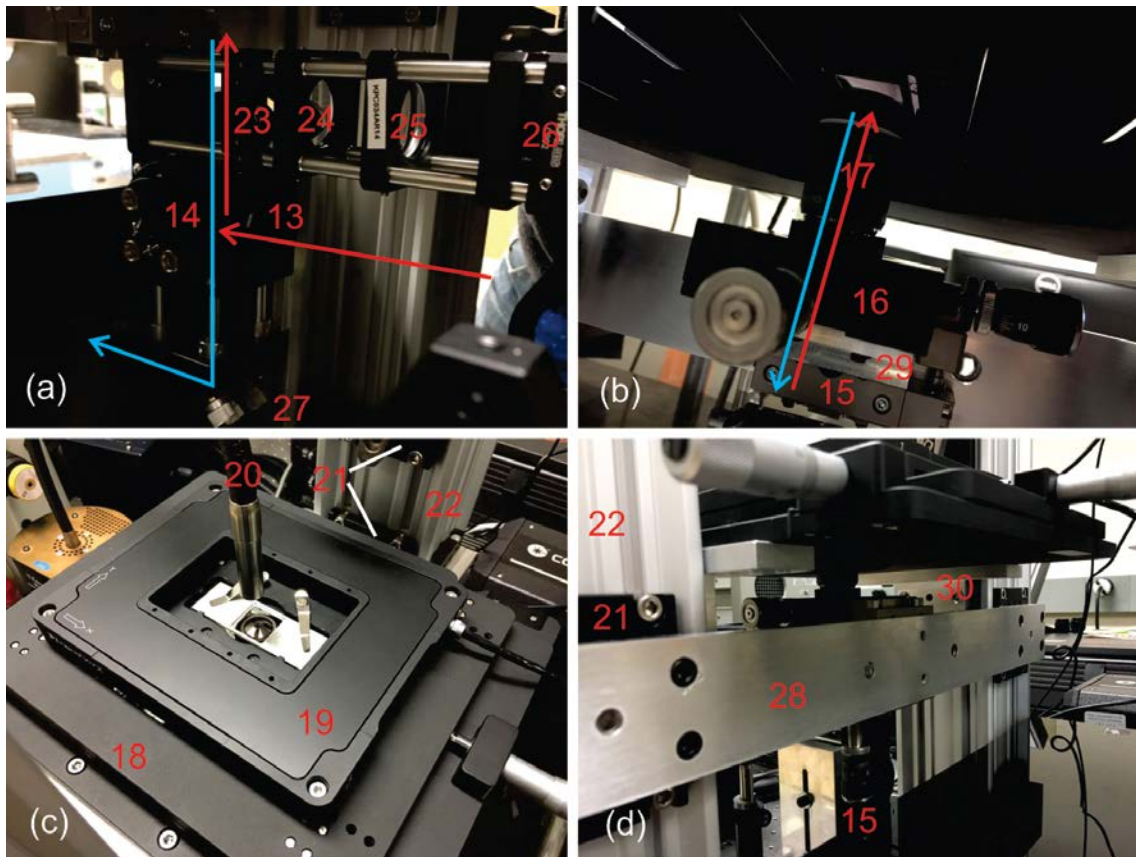
Figure 5-3: Sample irradiation part of second harmonic generation microscope

The dichroic mirror (Chroma, T680spxr, Component 14) provides a 99.96% reflection for the excitation beam at 800 nm, and a 97.62% transmission for the 400 nm second harmonic wave in our system. The dichroic mirror is expected to reflect the 800 nm upwards, while letting the direct downwards 400 nm go through, aiming at a good separation between our fundamental wave and second harmonic. This dichroic mirror is

installed in a 30 mm cage system (Thorlabs, C4W), to avoid vibration, disturbance and keep it in a clean environment. The dichroic mirror was mounted on a cage-compatible dichroic filter holder (Thorlabs, FFM1), fixed at a kinematic cage cube platform (Thorlabs, B4C). The whole connected cage system was fixed onto a self-designed bracket (Component 27), then fixed onto the floating optical table.

The dichroic mirror should direct the laser beam vertically straight up, which can be verified by using a mirror and a pinhole. A combination of two stages, connected by an adapter is used to control both the XY position of the objective, and the height. A TravelMax stage with differential drive (Thorlabs, LNR25D, Component 15) is fixed vertically onto a long aluminum bracket (Component 28). With a 25.4 mm travel range, this stage is able to control the vertical position of the supported objective in a relative large range. The differential drive helps to make fine control of the distance between the objective and the sample. The range of this fine drive is 250 μm, with a 0.5 μm graduation. Above this translation stage, an adapter (Component 29) is designed to connect with a 5 mm travel XY translation mount (Thorlabs, ST1XY-D, Component 16). This stage has a 0.4 mm per revolution coarse, a 25 μm per revolution fine control with 0.5 μm per graduation differential micrometers. Since this stage has a SM1 internal threads, two adapters were bought to connect different families of objectives. For a M25 external objective, a Thorlabs SM1A12 is used and for a Thorlabs SM1A3TS can be used to connect a RMS thread objective to this stage. A 100 x air objective (Olympus, MPLFLN 100x, Component 17) was used to focus the excitation light and collect the SHG signal. The numerical aperture is 0.95 and working distance is 3 mm. At the right position, this objective will focus the 800 nm fundamental beam to a 1-2 μm diameter point. The same objective collects back scattering 400 nm second harmonic, and guide that downwards, then separated by the dichroic mirror.

Sample will be placed onto the microscopy stage with an aluminum sample holder. The nano-positioning system that we have used is PInano ® XY Piezo Stage (PI, P-545.2C7, Component 19) and XY Microscope Stage (PI, M-545.2MO, Component 18) from PI (Physik Instrumente) that allows for coarse positioning.[1] The piezo-stage has two active axes along the X and Y directions and a closed-loop travel range of 200 μm for both axes.

The best close-loop spatial resolution of P-545 stage is less than 1 nm, which is more than enough for microscopic use. Importantly the piezo stage also provides repeatability of the positioning. A LabVIEW based software is responsible to drive the stage. The microscope stage onto which the piezo stage is mounted is manually controlled, providing a coarse 25 mm by 25 mm travel range. Above these two stages a light source (Component 20) is provided to illuminate the sample and collect the image of a large region in visible range. The image is reflected by a thin round cover-slip (Component 23), mounted unfixed between four cage assembly rods. Two lenses (Component 24, 25) are used to optimize the size of the image and direct that into a high resolution CCD camera (Thorlabs, DCU223C, Component 26).

To maximize the stability, the following design was used as the main microscope body. Two construction rails (Thorlabs, XT95-500, Component 22), with a length 500 mm were fixed onto the optical table vertically. The weight of these two rails are expected to minimize any possible vibration. A long aluminum bracket (Component 28) is responsible to connect the two rails, while further increased the stability. The connection between the aluminum bar and the rails is done by several rail plates (Thorlabs, XT95P12, Component 21). The aluminum bar is also used as an adapter to support the objective stage made of two translation stage, mentioned in the last paragraph. On the other side of the two trails, two other pieces of aluminum (Component 30) were cut into proper shape to provide a stable connection between the M-545 microscope stage and the two rails.

The generated second harmonic from loaded sample(s) is filtered by the dichroic mirror, to eliminate the fundamental wave, and other possible noises. Under that dichroic mirror, another dual band 400 nm and 800 nm mirror is fixed at 45 degree to direct the second harmonic towards the detection arm and data acquisition part of our SHGM, shown in Figure 5-3a. In Figure 5-3, the fundamental wave is shown as a red solid line and the second harmonic is shown in blue. The arrow indicates the direction of the laser/signal.

5.1.3   Signal Acquisition

The second harmonic collected by the objective is separated from the fundamental after the dichroic mirror. However, the second harmonic at 400 nm is very weak itself. Even without the fundamental, the signal can still be disturbed by any background noise. Here, the detection arm was designed to further filter the second harmonic, and eliminate the optical noise from the environment as much as possible. The Thorlabs 30 mm cage system was used along with 6 mm diameter cage assembly rod. Lens tubes were placed between the four assembly rods, to limit the optical noise from the room environment.
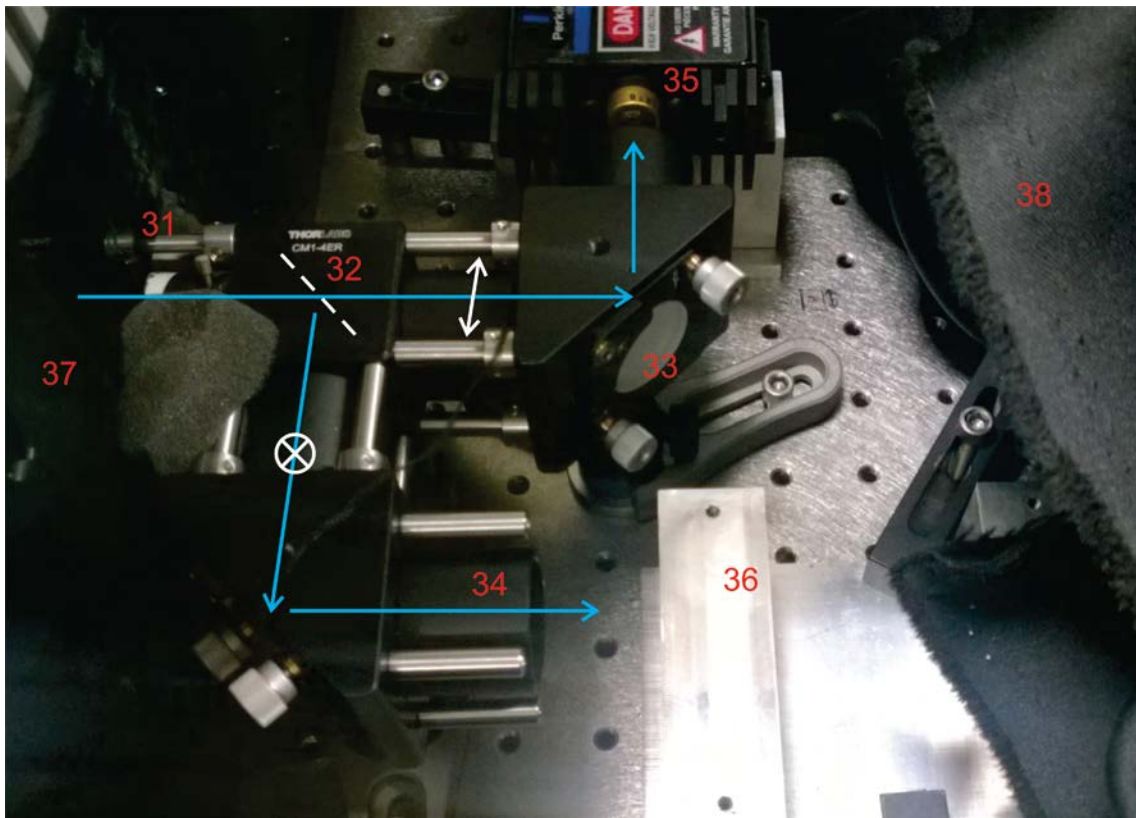
Figure 5-4: SHG detection section

The mirror under the dichroic mirror will direct any signal we are interested to the last part of SHGM hardware. Two filters (Component 31) are placed after the mirror, inside the black lens tube. A glass band-pass filter (Thorlabs, FGB39) with a region between

360 to 580 nm is used to further eliminate possible photons with the fundamental wavelength. This filter has a 0.0068% transmission at 800 nm, and 71.9% at 400 nm. The reason to use this filter is that the dichroic mirror cannot fully eliminate the fundamental thoroughly. It was noticed that the even the transmission of dichroic mirror we used is 0.1% at 800 nm, that still makes a difference and creating an unacceptable strong background on the detection part. There is a 100 times difference (0.10281% for P-polarization and 0.00092% for S-polarization) between the transmission of two perpendicular polarization at 800 nm. With this additional filter, the signal can be further purified. Another filter is located behind the first one to eliminate any other signal besides second harmonic, such as two photon photo-luminescence (TPPL). Usually the wavelength of TPPL is between second harmonic and fundamental so a proper band-pass filter is required. Here we select AHF F49-406, a 405/20 band-pass filter, which provides a 93.34% transmission from 385 to 425 nm while 0.0001% at 800 nm.

To further understand the polarization property of the second harmonic, we need to separate the signal into two perpendicular polarization components. A polarizing beam-splitter cube (Thorlabs, PBS251, Component 32) is selected. According to its specifications, this beam-splitter is designed to work over a spectral range between 420 to 680 nm. However, this cube has a 86.2% (p-polarized) and 0.11% (s-polarized) transmission at 400 nm which makes it a good choice for separating the second harmonic polarized signals. These cubes are designed to be used better with the transmitted beam, which offers an extinction ratio of Tp:Ts > 1000:1. The reflected beam will have an extinction ratio of roughly 100:1. A compact clamping prism cage cube (Thorlabs, CM1-4ER) contains the beam-splitter, and is connected with cage assembly rods. After the splitter, the signal is split to a horizontal polarized (parallel to optical table) branch, and a vertical polarized (perpendicular to optical table) branch, indicated in Figure 5-4.

The signal is subsequently separated into two identical channels. A dual band 400/800 nm mirror is responsible for reflecting the 400 nm signal into the avalanche photodiode detector (APD), through a convex lens. The mirror is mounted onto a right-angle kinematic mount (Thorlabs, KCB1, Component 33), which is designed for easy integration into a 30 mm cage system. This mount cube provides kinematic tip and tilt of

the mirror held in a mounting plate whose mean horizontal position is at a 45° angle. By adjusting this mount, the signal can be precisely focused on the APD active area. A convex lens (Newport, KPX079-C, Component 34) is hiding inside the black lens tube. This lens is coated with visible single-layer MgF_2, to have a <2.5% reflectance at 400 nm. Each channel includes a single photon counting module (SPCM) integrated with the APDs (Perkin Elmer, SPCM-AQR-15, Component 35). The SPCM sensitive areas are placed at the focal point of this convex lens, to obtain a maximum collection of the second harmonic. This SPCM are modules which detects single photons of light over the wavelength range from 400 nm to 1060 nm. The ideal dark count is 50 counts/s for the AQR-15 model. A TTL pulse of 2.5 Volts (minimum) peak with 50 Ω load and 30 ns wide, is output at the rear BNC connector for each photon detected. The working temperature is 5 ℃ to 40 ℃. The dead time for this series APD is 50 ns. If the signal is too strong (greater than 10 million counts per second), it will saturate the APD and may damage it. The APD is fixed onto a self-designed APD base (Component 36), which was clamped onto the floating optical table and cannot be adjusted. The peak photon detection efficiency is at 650 nm (70% typical), while at 400 nm the typical efficiency is only 5%. That makes it vital to provide a dark environment to avoid losing interesting signal. Three major measures were taken. The whole optical path was protected by black lens tubes. A piece of black cloth (Component 38) will cover the whole signal acquisition part. A black plastic box (Component 37) was also cut and installed on the optical table to provide a closed environment. Due to their extreme sensitiveness, the light of the room is supposed to turned off while the APD are turned on.

The TTL pulse generated from the two APDs collected with a data acquisition card (National Instruments, NI PCIe-6323), through a shielded connector block (National Instruments, NI BNC-2110). In Figure 5-4, one of the APD is removed. The leftover APD will only collect the y-polarized second harmonic from the sample surface. If the other APD is installed, that will measure the photon counts of x-polarized signal. The y-polarized signal will be guided by a BNC cable to PFI 0/P1.0/Trigger 1 port while the x-polarized will go to USER 2 port since PFI 12/P2.4 is not supported for a single BNC-2110 block. The USER 2 channel is connected to PFI8/P2.0 with a wire on the spring terminal block.

5.1.4   Summary

The construction of second harmonic generation microscope requires many components that we have wisely selected from several companies, such as Thorlabs, Newport, AHF, PI, Chroma and Perkin Elmer. The integration of these components is by itself a very interesting exercise to learn geometrical optics. It is important to highlight that due to the use of a very intense Class 4 laser with emission in the near-infrared range, laser safety measures must be undertaken at all times. Thanks to the machine shops in both Chemistry Department and Physics and Astronomy Department, Western University, several adapter(s)/base(s)/bracket(s) were also designed and manufactured.

Other strategies of designing a SHG microscope are possible. A galvanometric mirror system could have been used instead of the piezo stage. Both could have been combined as well. This would provide a clear advantage in terms of speed yielding mapping faster than when using the point-by-point piezo-enabled motions. However, this microscope was initially designed to study SHG from metallic nanoparticles requiring typical scanning area of less than (20×20) μm^2. Furthermore, the second harmonic generated from the particles is not strong enough to make a fast scan. Considering these factors, a piezo stage was finally selected to control the spatial position of a sample with superb resolution and reproducibility. It turns out that a resulting optical resolution down to 200 nm can be achieved, and minimum scan step can be set to 10 nm makes piezo stage a better choice in this situation. Another reason for not choosing galvanometric mirror is the back entrance of our objectives varies from 3 mm to 8 mm, depending of our objectives. For most of the galvanometric mirrors, they are designed to work with a small beam, such as Thorlabs small beam diameter galvanometer system (diameter less than 5 mm). Not fully filling the back entrance will be detrimental to the quality of imaging.

The detector used could have also been different. Liquid Nitrogen cooled single photon CCD camera could have been used. Despite the cost of one single photon CCD camera, it is still not recommended for this setup. To use this CCD it requires the fundamental wave covers a large area. Under that circumstances, the distribution of the second harmonic will be collected and imaged instantly by the CCD. However, as a nonlinear process, second harmonic is proportional to the square of the fundamental power. If the

fundamental wave is not focused, the shortage of intensity density will result in a drastic reduction of second harmonic.

In the signal acquisition part, cage system encloses efficiently protects the weak signal with black lens tubes, reflected and focused into the aperture of APDs. Another possibility is use optical fiber coupling. Fibers will give less noise while guiding the signal. Nevertheless while the light is propagating in a fiber, the polarization may be modified unless a single mode fiber was used. Fragile fibers need to be handled with extreme care. One important issue is due to the fiber coupler required to direct the signal into or out from a fiber. Not like other applications, this setup will collect a weak signal at near UV region. It is difficult to couple a signal which is almost impossible to see by eyes. However using a mirror/lens system will provide more freedom to control, and much easier to maintain. For the reasons mentioned above our approach was the most cost efficient and versatile to build a SHG microscope.

5.2   NI LabVIEW based Software

A software called *SHG Microscope_1.3.vi* was programmed to provide a versatile user interface in order to control this SHGM by LabVIEW.[2,3] The purpose of this software is to control every possible electronic device used in this setup and to perform some basic data analysis. This software is able to select the interested region and resolution/minimum step to the piezo stage.[4] While the stage is in motion, the signal from two APDs is collected for a certain acquisition time. Another main function is to control the polarization of the input laser beam, either set to a certain angle, or do a full circle while collect the signal simultaneously, to investigate the polarization response. In addition, the shutter can also be turned on/off both manually and automatically. The main part of this program will be displayed and explained in detail hereafter.

5.2.1 User interface
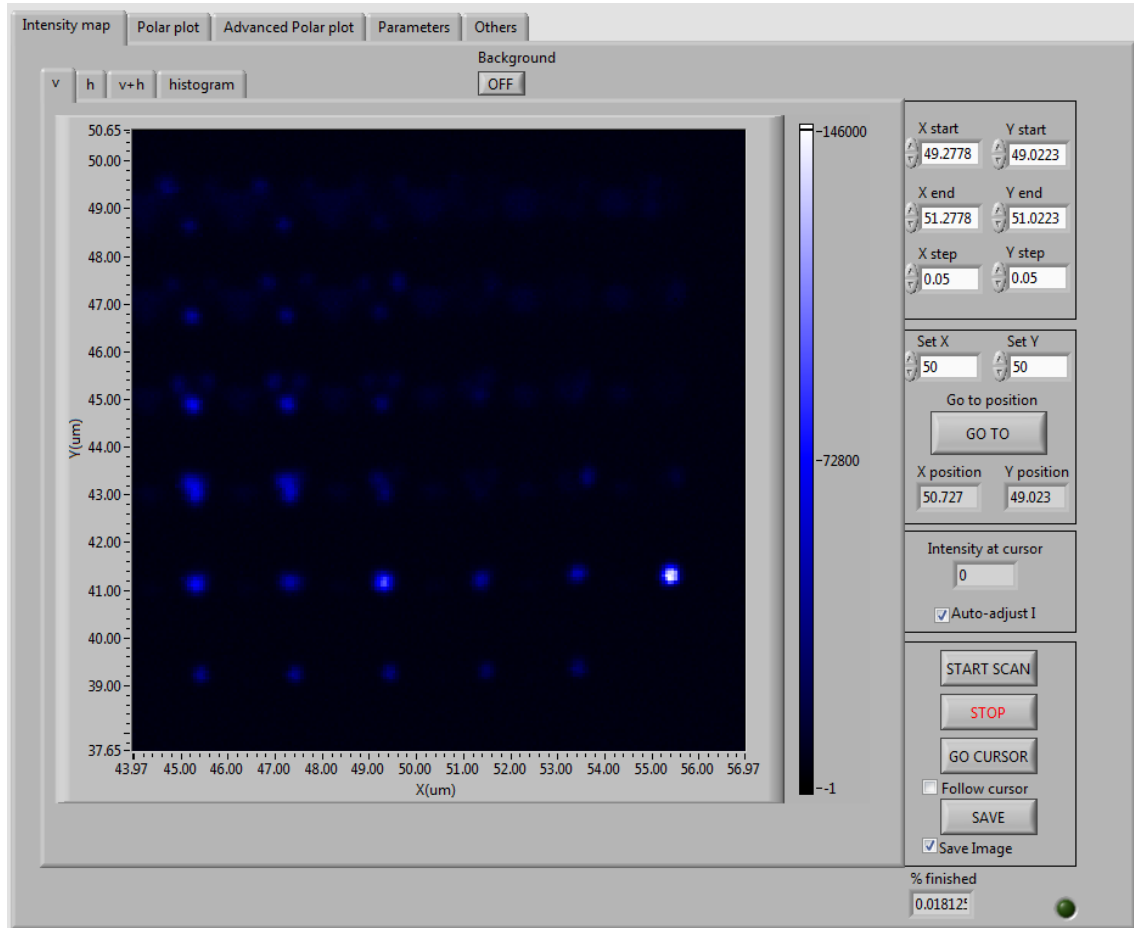
Figure 5-5: User interface of SHG Microscope_1.3.vi. This is the panel to conduct a 2D scan over sample surface.

At the top of this panel, several tabs are listed. The *Intensity map* will be used to plot a second harmonic intensity map of a selected region. The *Polar plot* panel can rotate the polarization of the fundamental by 360 degrees while collecting the signal, in order to do a polarization analysis on a single point. *Advanced polar plot* was later designed, aiming at a different, more accurate polarization analysis. *Parameters* display some variables used in this software, as well as a helping tool to tune the focus of the objective, which are further detailed in the standard operating protocol (in Appendices B). The last tab, *Others* will show additional information about the piezo stage control and the motorized

precision rotation stage to control the wave-plate that controls the input polarization direction.

As a microscope, this setup has to be able to scan the sample surface along the x and y directions and plot a map which shows an intensity spatial distribution of the measured second harmonic. The first panel, is designed to have a full control of the position and to conduct a continuous write/read motion while the scan is ongoing. The *v*, *h*, *v+h* contains the second harmonic intensity map for different polarization after each scan. The *h* tab shows horizontally polarized, or x-polarized polarized signal while *v* gives the distribution of a vertical polarization with respect to the optical table plane. The sum intensity of both polarization, is displayed in the *v+h* tab. After each scan, *histogram* will also give additional information of how strong the second harmonic is.

To enable a scan, the spatial limits of the scan area must first be defined. The scan region can be manually entered into the *X start, X end, Y start, Y end*, with a unit of µm. The resolution is defined by *X step* and *Y step*. The suggested best (minimum) step/resolution is 10 nm. The resolution of the defined scan will be $resolution = (end - start)/step$. For example, if *X start=Y start=40, X end=Y end=60, X step=Y step=0.1*, the scanning area will be from 40 µm to 60 µm with a minimum step 20 nm for both axes. In this case the resolution of this map will be 200 by 200 pixel.

The other way to define a scan region is to enter the size of the region and the number of pixels directly. To do so, the number needs to be entered in the dialog box beside (Figure 5-6).
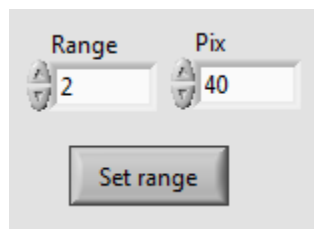
Figure 5-6: Additional choice to conduct a surface scan.

The range of this scan will be centered from current position, plus/minus *Range*/2. Resolution will be *Range/Pix*. In this case, the step size resolution is set to 50 nm. After the numbers are entered, the *Set range* button needs to be clicked so the start/end/step value will be calculated for both X and Y direction.

To move the piezo stage to a given position, the *Set X/Y* needs to be defined and click the *GO TO* button. Below that button is the current position, *X/Y position*. After the scan is finished, a cursor should be available on the map and the intensity at the cursor position can be read in *Intensity at cursor*. *Auto-adjust I* is normally activated to have a clear image in the left part. The color bar can be manually adjusted only if *Auto-adjust I* is inactivated.

After the scan region and step is defined, *START SCAN* starts a scan. Anytime, the *STOP* can be clicked to stop the current scan to reset the scan parameters or else. *GO CURSOR* will move the piezo stage to the current position of the cursor. It is commonly used while a polar plot is required. If the position needs to be changed continuously, the *Follow cursor* check box can be selected and move the cursor. Click on *SAVE* will open a dialog box to select the path and file name of current map, for all the v/h/v+h channel. If the *Save image* check box is selected, the image will also be saved.

The last two indicators will help the user to see how much is left to finish the current scan (*% finished*), and if the piezo stage is in motion or not (the green indicator in the bottom right). On the top of the image, there is a *Background* bottom. By pressing/releasing this button, the background will be deducted/added for every pixel in the plotted SHG map.

When the *START SCAN* bottom is clicked, the software will drive the piezo stage to the start position. The shutter will be automatically turn on, to let the fundamental wave go through and bombard the current position of loaded sample. The photon counts of two perpendicular polarization during the acquisition time (can be defined in the *Acq times (ms)*, *Parameter tab*, Figure 5-10) will be recorded simultaneously from the two APDs. The photon counts will then be normalized to photon counts per second, and plotted on the corresponding pixel position. After that, the software will give the order to move the

piezo stage to the next position, and repeat until the whole scan is finished. Once the scan is complete, both the data and the images can be saved.
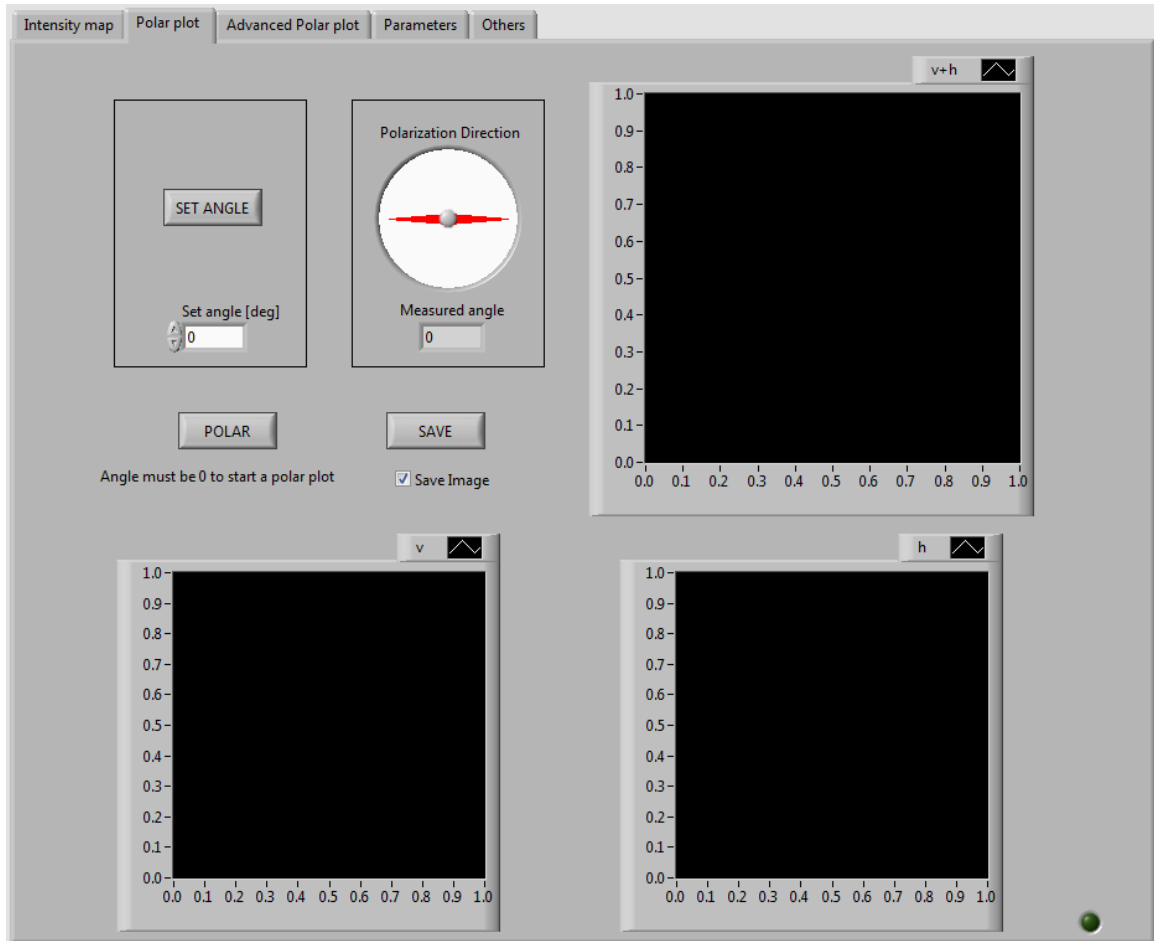
Figure 5-7: The panel to control the fundamental wave's polarization and do a normal polarization analysis (polar plot).

Another important function is to see the polarization dependence. Since second harmonic generation is a nonlinear process, the polarization dependence can offer more interesting details regarding surface or molecular properties. This panel was designed to do so. The basic function is to set the polarization of fundamental wave to a specific angle. The polarization can be oriented by entering the target angle of the half waveplate in *Set angle [deg]* with a unit of degree. However, the polarization will be changed by 2 degree with

every degree the waveplate rotated. This is considered when the program is coded. So the *SET ANGLE* button will set the angle for the waveplate, and to the right the *Polarization Direction* and *Measured angle* will show the polarization both graphically and numerically. Zero degree means a x-polarized fundamental on the sample surface. To obtain a y-polarized beam, the *Set angle [deg]* needs to be set to 45 and click *SET ANGLE*. While the rotation stage is in motion, both the graphical and numerical indicator will be changed in real time. To do polarization analysis, the initial polarization should be set to 0, or x-polarized. After that, the POLAR button will start an automatic sweep from 0 to 360 degree and collect the photon count. The polar plot will be displayed as three graph, indicating x-polarized (*h*), y-polarized (*v*), and the sum intensity (*v+h*).

This polarization analysis will require the piezo stage to be frozen at a given position keeping the laser focused on the object of interest. However, in some certain case, polar plot collected over a selection of points is also of interest. On some specific sample, polar plot on one single location may give out a unstable or even false result due to unexpected surface disorder, such as a spike may create a sharp overwhelming second harmonic in a short time. Here, another way to commence a polarization analysis is compiled, and named *Advanced Polar plot*.
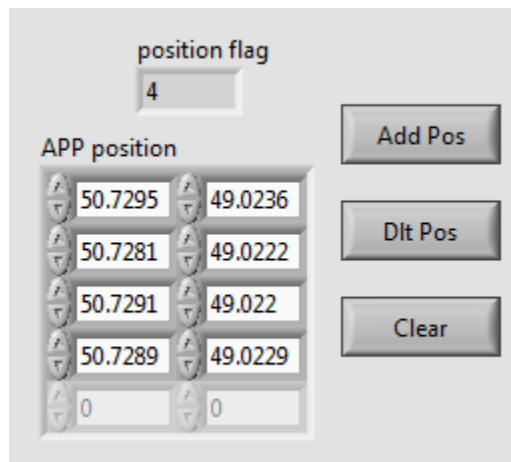
Figure 5-8: The position list used for advanced polar plot

In this advanced polar plot mode, several location coordinates can be selected to commence a polar by using the side panel, as showed in Figure 5-8. The *Add Pos* will

add the current position of piezo stage in the end of the table shown in Figure 5-8, named *APP position*. By doing so, the *position flag* will increased by 1, indicates the number of positions stored in the queue. To remove the last queue element, *Dlt Pos* can be clicked. In some case, a entire new position queue is needed. To delete every element in the queue, *Dlt Pos* can be used until the queue is empty, or *Clear* is recommended to click since this function will purge the whole queue and reset *position flag* to 0.
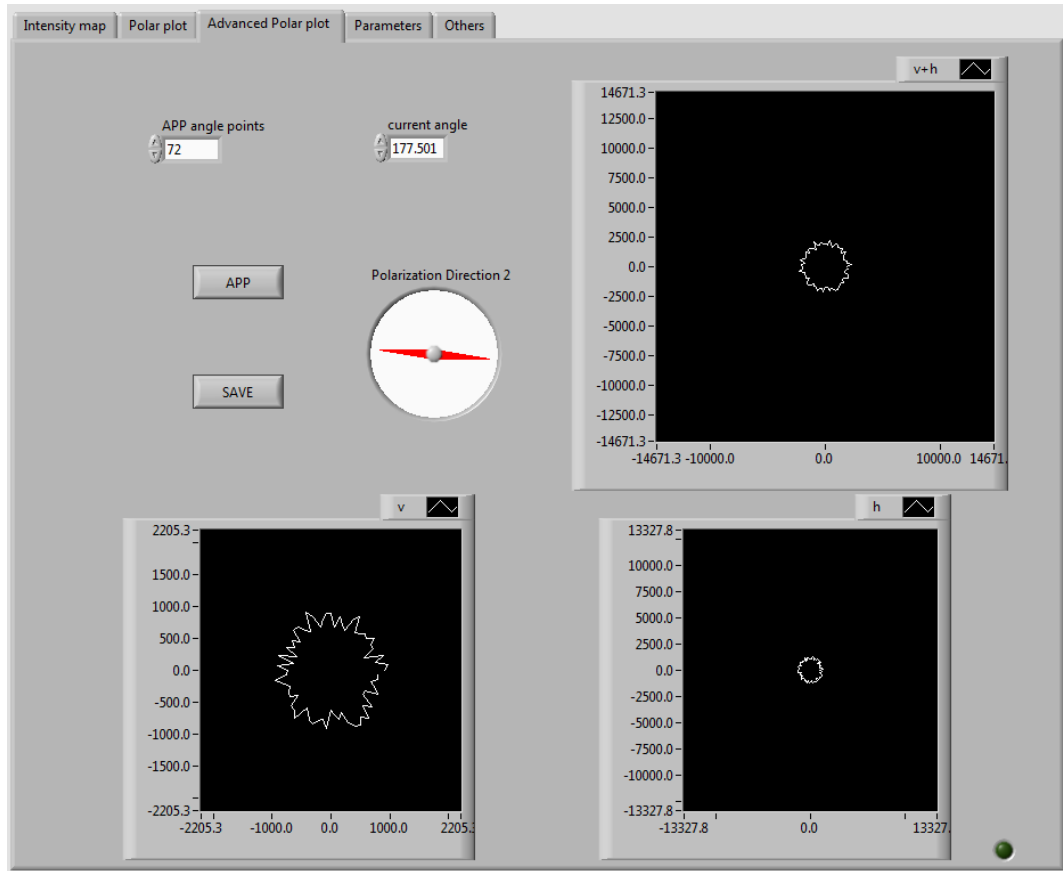
Figure 5-9: Another approach to do polarization analysis. Advanced polar plot will record the polarization dependence on several location.

Once the *position flag* is not 0, or the *APP position* is not empty, the advanced polar plot can be started. More than a default polar plot, this advanced mode will have more freedom to be played with. To obtain the best performance of this position, two more parameters needs to be adjusted. In Figure 5-9, the *APP angle points* defines the angular resolution of this polar plot. Here 72 stands for 72 data points or stops of the 360 degree,

with a angular resolution 5 degree. The second parameter can be modified is the *Acq times(ms)*, the same one used while doing the second harmonic generation map. That can be found in the *Parameter* tab, Figure 5-10. If *Acq times(ms)* is set to be 1000, the software will give command to the rotation motor of the waveplate to remain still for 1 second at every angle this advanced polar plot is required. The APDs will collect signal and convert it to photon counts per second. The polar plots for the listed positions will be averaged and plotted in the three graph, like a default polar plot. The main difference between these two polar plots, is the advanced one will collect the signal from multi-locations over a defined acquisition time. In other words, the advanced plot will provide a statistically relevant set of information.
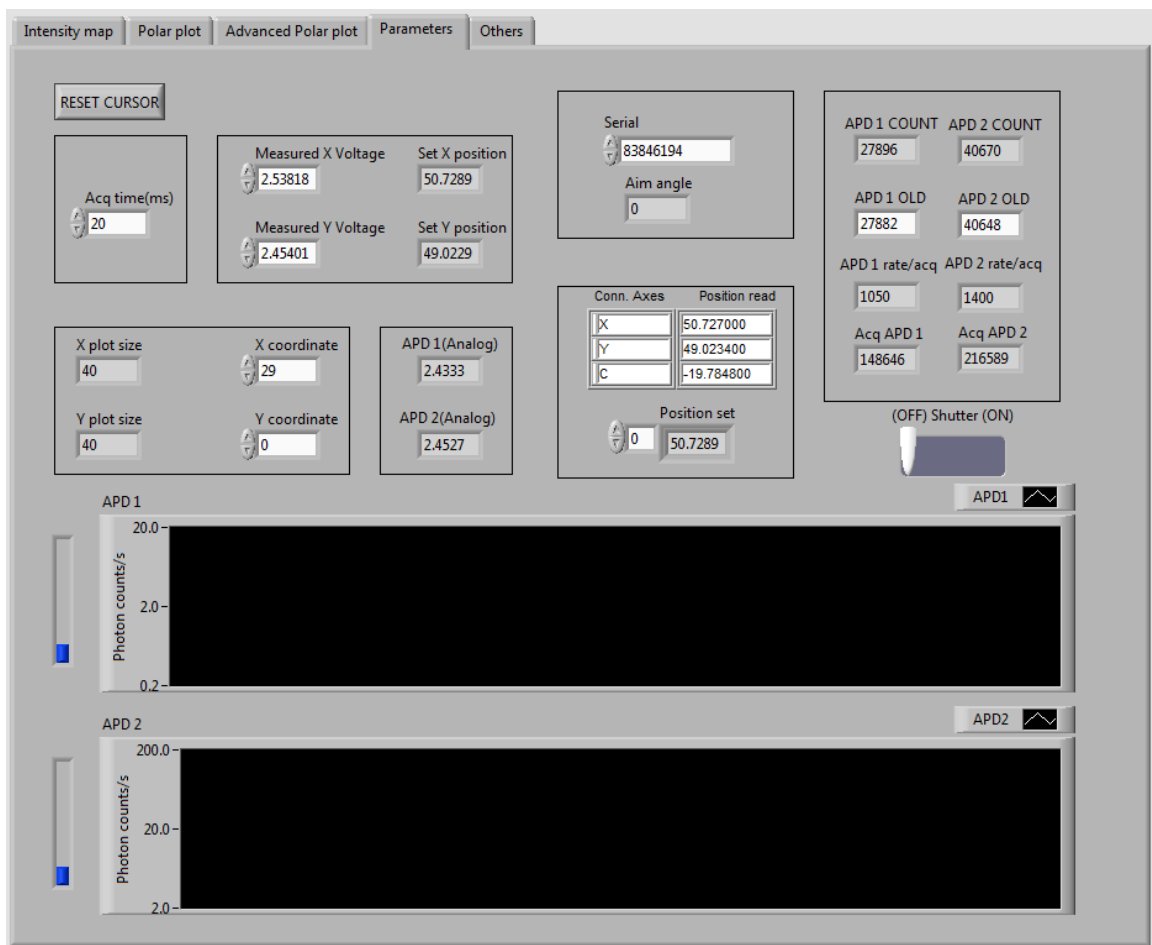
Figure 5-10: The *Parameter* panel. Multiple variables will be displayed here to examine the current state of the electric devices.

Another important panel is *Parameter*. Several controllers are located in this panel providing the current parameters and the status of the whole microscope. At the top left of Figure 5-10, a *RESET CURSOR* will reset both x and y cursors (in the *intensity map* tab) to center, when the cursor is out of screen or lost. As mentioned before, the acquisition time of collecting second harmonic distribution map and advanced polar plot can be modified while changing the *Acq time(ms)*. Shutter can also be manually turned on or off by the *(OFF) Shutter (ON)*, even it is controlled automatically no matter a SHG image or a polarization analysis is gathering. Normally the shutter needs to be turn on in the focusing process. *APD 1* and *APD 2* shows the photon counts in real time, which can also be used to focus the fundamental laser onto the sample by tuning the z-position of the objective. The detail of this operation can be found in the appendix.
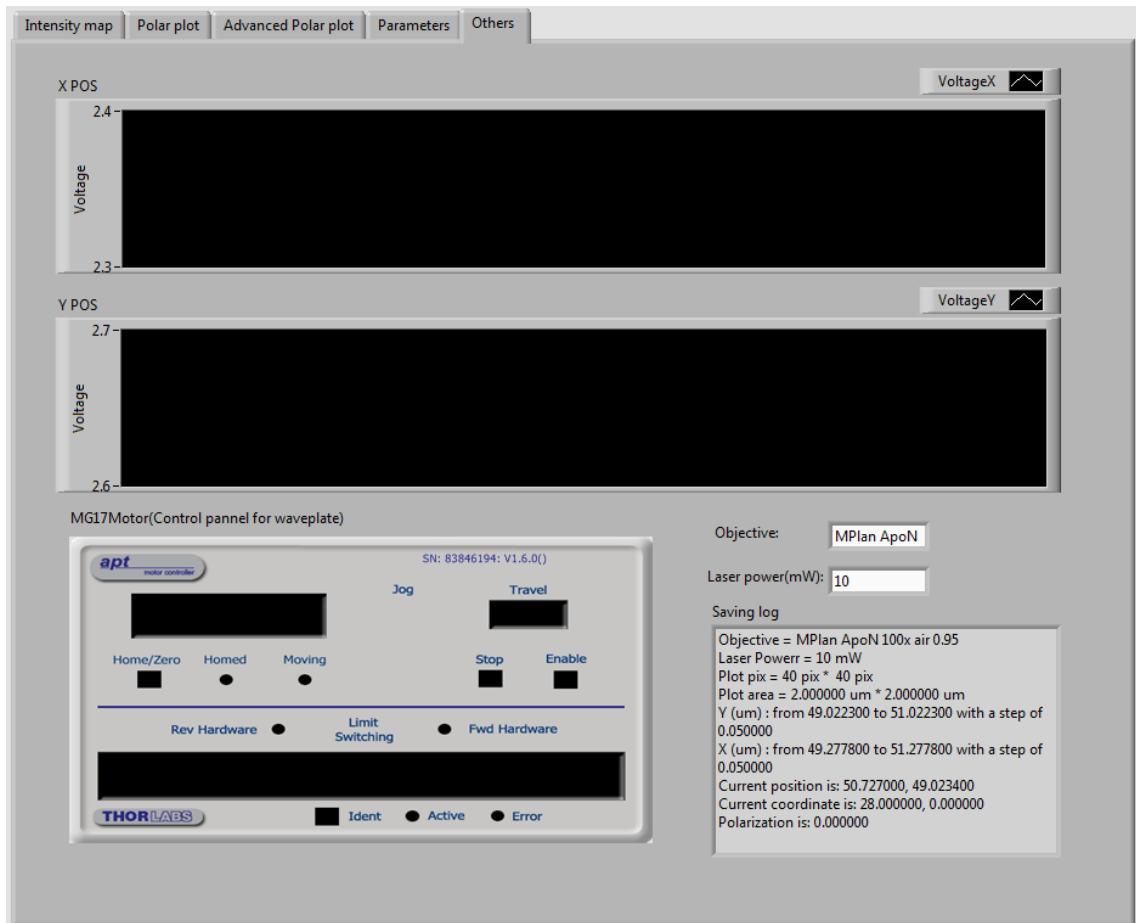
Figure 5-11: The *Others* tab shows the feedback signal of piezo stage and other information.

The feedback signal from the piezo stage can be checked in the last tab *Others*. The piezo stage will deliver a voltage signal which is proportional to the current location. The voltage is plotted in *X/Y POS*, can be checked to confirm that the software and the piezo stage are functioning properly. The *MG17Motor* at the bottom left is another interface to control the polarization manually. The last part of this panel is an information text box which contains the detail of current experiment, such as the objective and the power used. Both of them should be manually defined. In addition, current position/polarization, scan detail are also included here. This text box will be save automatically whenever a SHG map or a (advanced) polar plot is saved, under the same filename. With the help of this text box, the current condition can be bundled with every single data to make sure no information is missed.

5.3   Conclusions

I have fully develop a SHG microscope during the scope of this thesis. Details are provided to give future users a sense of why and how we made such setup that will continued to be used in the FLL group. The application and testing of this setup is described in the next two chapters on samples that are presumably SHG active due to the absence of inversion center of the structures.

5.4   References

(1) Physik Instrumente *PZ217E User Manual* Karlsruhe, Germany, 2012.

(2) National Instruments *Labview User Manual* Austin, Texas, 2009.

(3) Travis, J.; Kring, J. *LabVIEW for Everyone: Graphical Programming Made Easy and Fun (National Instruments Virtual Instrumentation Series)*; Prentice Hall PTR, 2006.

(4) Physik Instrumente *Updating PI Software* Karlsruhe, Germany, 2011.

Chapter 6

6 Second Harmonic Generation Microscopy from Non-centrosymmetric Gold caps on Polystyrene Spheres

Nonlinear optical properties of gold coated polystyrene nanospheres are investigated using second harmonic generation microscopy. After being deposited onto a glass surface, the polystyrene particles were coated with a thin layer of gold deposited by electron-beam evaporation. Since only half of its surface is coated, it results in a non-centrosymmetric nano-object that can presumably yield a second-harmonic signal. The non-linear signal was collected from isolated half-capped particles and the polarization measurements of the SHG signal were performed on both bare particles and particles where the gold surface was further functionalized with molecules that possess a high hyperpolarizability. The functionalization of the gold surface slightly improved the overall magnitude of the second harmonic signal.

6.1 Introduction

Nonlinear optical spectroscopy offers an innovative arsenal of advanced methods. Second harmonic generation, as the lowest order of nonlinear optical phenomenon, is only sensitive to non-centrosymmetric materials, makes it a ideal technique for surface characterization, high-resolution imaging and bio-imaging[1-3] as long as the sample present an organization with no center of inversion. The label-free feature allows the possibility to achieve living sample imaging[4,5] with improved focus volume, and fine details to be visualized with a high spatial resolution.[6] Metallic nano-particles were also investigated as good candidates for SHG measurements. The optical properties of these nano-particles have attracted major attention due to a variety of applications such as biomarkers[7], photonic elements and for ultrasensitive spectroscopy applications.[8] Furthermore, since the nonlinear susceptibility $\chi^{(2)}$ vanishes in bulk isotropic material, only metal materials with local non-centrosymmetry are second harmonic generation (SHG) active due to the absence of inversion center in the structure.[9] More specifically, SHG from a variety of nanostructures was investigated in the past decade.[10-12] At surface of some symmetric particles like spheres, the interfacial region where the inversion

symmetry is broken provides a source of the optical nonlinearity.[13] There are also some theories about SHG from metal spheres.[13,14] However, due to its symmetric shape, the second harmonic is easily overwhelmed by surface defects, and possible applications are limited. Many nanostructures have been designed and fabricated using top-down or bottom-up approaches. However due to surface tension, the nanoparticles tends to form a sphere shape, which is centrosymmetric shape, in a annealing process.[15] Synthesis methods usually is often limiting factor to provide narrow distribution of sphere with precise control over their size.[16] Another way to fabricate nanostructures is electron beam lithography, which however, is expensive and inefficient for large surface fabrication. For nanosphere lithography (NSL)[17], scientist are mostly interested in the substrate as known as the Fischer's pattern.[18] In the present work we have made use of the particles produced during the NSL procedure. These particles are polystyrene spheres that are partially coated with a metallic thin film as further described later.

There are multiple ways to enhance the second harmonic generation by functionalizing the surface of a given sample with molecules that have a high charge transfer between an electron donor group and an acceptor group.[19,20] Azobenzene-containing molecules mentioned in Chapter 3 do show such high charge-transfer and resulting hyperpolarizability that can be tuned by altering the chemical nature of the donor/acceptor pair.[21-24] A monolayer of such molecules can be formed at the gold surface in particular when thiol groups are present. In such case, the second harmonic signal is expected to be enhanced.

Here, polystyrene nanoparticles were half capped with gold using the nanosphere lithography technique.[17] Such particle is non-centrosymmetric and should presumably be SHG-active. Herein, the SHG signal of such individual particles is first studied using the microscope detailed in Chapter 5. The particles are then functionalized with molecules to provide surface functionality and possibly further enhance the SHG signal.

6.2   Experimental Methods

6.2.1   Second harmonic generation microscope

All the details of the setup used in this work are provided in Chapter 5.

6.2.2   Nanosphere Lithography

Polystyrene microspheres (10% (w/w)) of 1.00 µm diameter in water were purchased from Thermo Scientific Co., Fremont, California. Glass microscope coverslips (22 mm × 22 mm × 0.15 mm) purchased from VWR International, Mississauga, Ontario. In the first step of the cleaning, to remove organic molecules on the surface, the glass coverslips are sonicated in acetone. To further remove any residual organic molecules, the coverslips are sonicated in a solution of Nochromix and concentrated sulfuric acid. Once rinsed with Milli-Q water, the cover slips are sonicated in a 5:1:1 solution of Milli-Q water, ammonium hydroxide and hydrogen peroxide. The coverslips are then rinsed with and stored in Milli-Q water until use. The coverslips were first dried by spin coating them with an acceleration of 670 rpm per second for 10 seconds. This process was repeated to ensure that the coverslip was dry. A 1:400 solution of Triton X-100 in methanol was prepared followed by a 2:1 solution of polystyrene (1 µm, ThermoScientific) in the Triton methanol mixture. To the dry coverslip, 80 µL of the 2:1 polystyrene solution was added. The coverslip with the polystyrene was then accelerated on the spin coater at 135 rpm per second for 20 seconds, then removed and dried. The sample was then etched by oxygen-plasma treatment for 5 min to decrease the polystyrene size. 3 nm of titanium followed by 30 nm of gold were deposited onto the surface by electron beam deposition. Finally, the polystyrene spheres were then sonicated in ethanol for approximately 10-20 sec to detach from the coverslip. The ethanol mixed with polystyrene was collected and 25 µL of which was drop casted onto a clean cover slip. Photoetched coverslips with fiduciary marks (Electron Microscopy Sciences, #72264-18) were used as the substrates, in order to provide possibility of localizing a selected nano-particle and observing it optically with our SHG setup or with an electron scanning microscope.

6.3 Result and discussion.
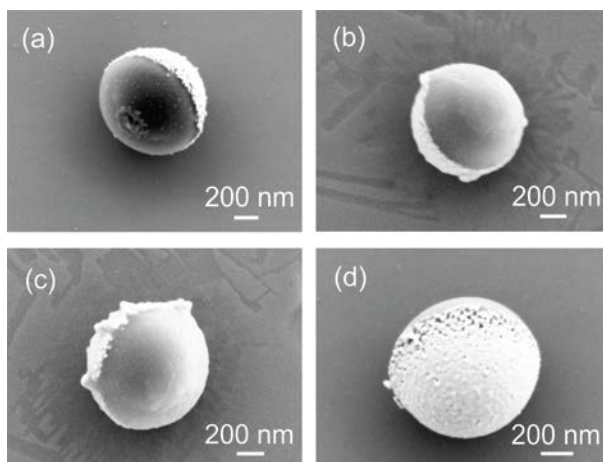
Figure 6-1: SEM pictures of several half gold coated polystyrene particles. Once deposited onto a surface, multiple resulting orientations can be observed (a-d). The deformation of the polystyrene particles at the bottom(a) may due to some local heating during plasma treatment of electron beam deposition of gold. (c)(d) The deposited gold shows large roughness and isolated gold particle on the equatorial line due to the geometry of the deposition process.

SEM images of several individual half-coated polystyrene spheres are presented in Figure 6-1. The mixture of ethanol and gold-polystyrene sphere give rise to the random orientation of these particles on cover slips in our case, or any substrate. The diameter of these spheres is estimated to be around 970 nm, slightly less than 1 μm, due to the diameter reduction after the oxygen plasma treatment. This etching process also results in the deformation in the bottom of polystyrene (Figure 6-1a) which may be due to local heating of the portion of the sphere in contact with the substrate.[25] Such heating can occur during the plasma treatment or during the electron-beam deposition of the metal over the polystyrene spheres. The spherical surface of the gold cap helps to create a rough layer, especially one the equatorial line since the side walls are parallel to the direction of electron beam evaporation of gold atoms. At some locations, the gold layer become discontinuous, forming isolated aggregates (Figure 6-1d). After drop casting, these isolated half-coated particles distributed all over the surface. Some of them assembled to clusters. The experiment was mostly focused on isolated ones, to investigate the

properties while eliminate the effect of coupling within each other. The shape and size of these half coated nanospheres are well-controlled. By using this method, these gold caps can be deposited on any substrate, making it an ideal sample for measurements in both the visible and IR spectral ranges. The size of these gold caps can be modified by using smaller polystyrene spheres.
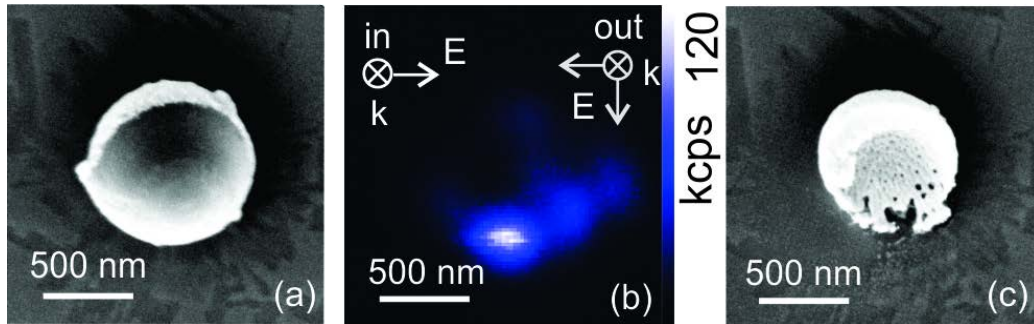
Figure 6-2: An example of laser-caused modification on one half-coated polystyrene particle (a). The second harmonic generation map (b) was obtained by using a focused 10 mW femto-second laser at 800 nm. While doing the imaging of this particle, the polystyrene sphere is removed (c) due to heating effect.

Before getting the SEM image of the particle, a 3 nm layer of Osmium was coated to prevent the sample from charging and reduce damage from the electron beam (Filgen, OPC80T). It is tested that the Os coating does not alter the SHG imaging meanwhile it improves greatly the quality of obtaining SEM images of non-conductive samples or conductive samples deposited over a non-conductive surface. After the locations of several individual nanoparticles are marked, second harmonic generation signal was collected from one gold-polystyrene particle (Figure 6-2a). The combination of our half-waveplate and a glan-laser calcite polarizer keeps the laser power to 10 mW at the sample, to prevent possible damage to gold nano-caps. SHG microscope was used to scan (2×2) μm^2 area, with a resolution 100×100 pixels (Figure 6-2b). After that, another SEM image was done on the same particle, to see the effect of the laser irradiation (Figure 6-2c). Surprisingly, it turns out that the polystyrene spheres have disappeared. We propose two scenarios that can cause such effect: (i) the laser power of the excitation is too high and melt the polystyrene sphere while keeping the gold coating intact. (ii) a local

plasmonic enhancement of the excitation light or the second harmonic induce a local heat sufficient to cause the melting of polystyrene.[26] In both cases the raise of temperature has to be high enough to surpass the melting point of polystyrene (240 °C).[26] With our femto-second pulse laser, the continuous scan will provide much more energy to melt the polystyrene. Eventually, the only thing left is the non-centrosymmetric gold cap. In order to find the origin of the melting/evaporation process, a non-coated polystyrene sphere was irradiated under same irradiance conditions. For the bare particle, no SHG was detected and the particle did not experience any melting behavior, which indicates that a plasmonic-mediated effect is the cause of the evaporation or melting of the polystyrene material.

For the experiments done with gold capped polystyrene spheres, the residual gold cap keeps the same shape and orientation. The size was slightly shrunk due to the absence of polystyrene sphere. SHG map (Figure 6-2b) gives information of the distribution over the cap surface. Strong second harmonic was detected, especially for spot below the center point. The signal was orders of magnitude stronger than the rest of this SHG map. At the similar relative position, a cavity was noticed at Figure 6-2c. It is hard to ignore the correlation between these two abnormalities. The imperfect nanocavity, resulting from either incomplete electron-beam evaporation coating, or peeling-off of the polystyrene, gives additional roughness or finer corrugation. The cavity helps to significantly enhance the SHG, which might be explained by the coupling of fundamental wave to localized modes. The surface symmetry broken was also contributed this extraordinary enhancement. Similar study was performed in other group.[27] This melting effect was observed on many nano-caps. For larger fundamental power or longer irradiation, the femto-second laser may totally damage the gold cap and leaves small gold pieces.
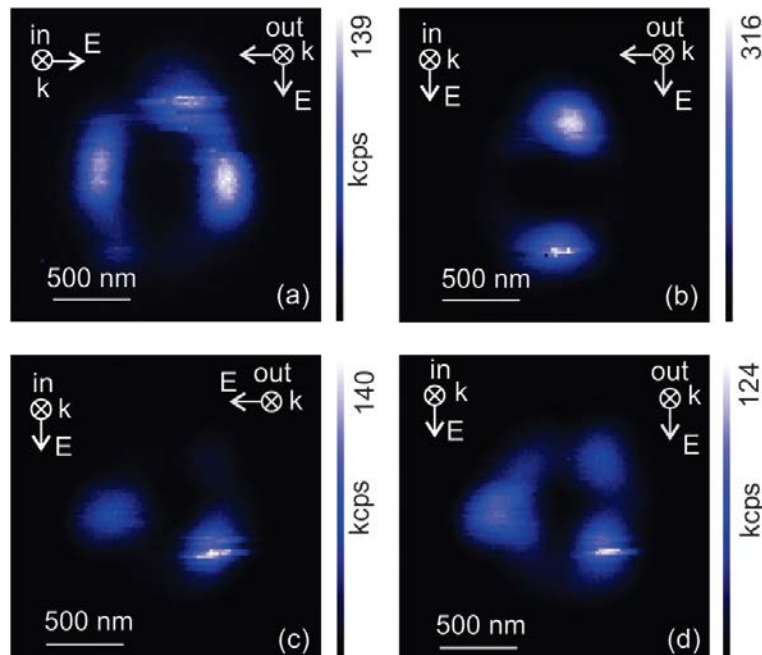
Figure 6-3: Effect of changing input polarization and separate output channels. The polarization of fundamental effects the distribution of second harmonic.(a)(b) The difference of two perpendicular polarized SHG signal shows irregularities of the gold cap surface.

In addition to the dependence of the SHG signal with the spatial orientation of the gold cavity over the surface, the polarization of the fundamental beam can also be tuned to reveal spatially-dependent SHG activity. In order to eliminate the contribution of tilted cavities, a facing up (or down) gold cavity was selected. This regular cap presents a ring shape (Figure 6-3) on the SHGM image highlighting that most of the second harmonic signal generates from the edge. Several reasons can cause this effect. In the center of the cap, the gold deposition is quite smoother than on the edges which does not support this nonlinear phenomenon. This can be explained by accessing the geometry of the central portion of the cap. The central part is relatively large (diameter of 970 nm) and can be considered to be less symmetry broken as compared to the edges of the cavity. At the edge, the roughness or possible cavity contributes SH. The polarization dependence of fundamental wave can visualized in Figure 6-3a. Here, a x-polarized fundamental beam shows intense strong SH signal localized in 3 specific areas (Figure 6-3a) with no direct correlation with the input polarization. While switching the input polarization by 90

degree (i.e. along the y direction), the position of SH dots appears along the y direction (Figure 6-3b). This can be explained by the preferential excitation of the localized surface plasmon modes along the polarization direction. While nanoparticle are irradiated by an external field, the free electron of the metal oscillate due to changing of the electric field direction. If the size of the nanoparticle or nanostructure is similar to the wavelength of the light, localized enhanced area will be localized around this structure the properties of which matches SHG conditions in terms of wavelength resonance and shape compatibility. Such matching conditions are dependent on the polarization direction.

Another parameter of interest is the polarization of the output SH. For another individual particle, the SHG signal can be separated into two polarization: perpendicular with respect to the fundamental beam (Figure 6-3c), and parallel to the fundamental beam (Figure 6-3d). Here again, the SH distribution still looks different for two orthogonal polarization. Considering that the detailed structure of the surface is difficult to control, so is the scattering of the fundamental that may induce more plasmonic coupling mode.
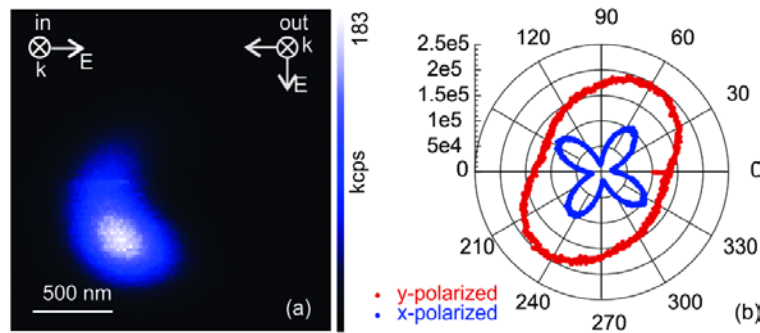
Figure 6-4: Polarization analysis was done on several individual particle. The input polarization is rotated along a full trigonometric circle (360 °). The polarization polar plots are acquired on the two channels simultaneously for each incident input polarization. For a selected particle shown in (a), a pure quadrupolar polar plot is collected along the x-direction ($\chi^1=0$, $\chi^2\neq0$).[28] On the other channel, y-polarized, a pure dipolar was collected (b).

In order to better understand the SHG from the surface, a full polarization analysis was also conducted on particles. Due to the random orientation, various radiation patterns

may result. However, for some particle, a four lobes pattern was detected along the x-polarized SHG channel (Figure 6-4b). This correspond to a pure quadrupolar ($\chi_1=0$, $\chi_2\neq0$) SHG pattern for a x-polarized excitation input. [28] On the other channel, a y-polarized, pattern reveals a pure dipolar SHG pattern.
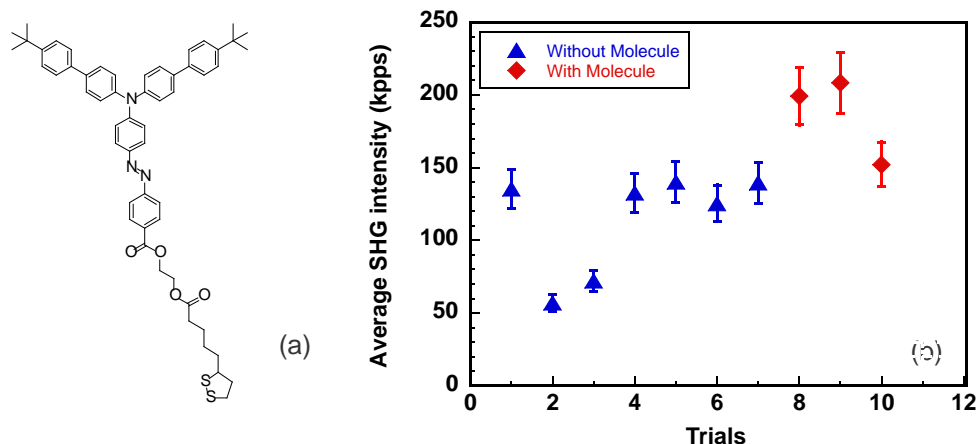
Figure 6-5: Several experiments were done over a cluster of gold caps to demonstrate the effect of introducing the molecule. (a) tBuAzoS2 (b)The average SHG intensity was collected from the top 0.5%-5% of each SHG map, in order to eliminate the spikes and the background.

The second harmonic generation from the gold cap can also be interpreted as a result of surface symmetric broken. Bulk gold exhibits zero hyper-polarizability due to the symmetric lattice structure. However, at the surface, the symmetry is inherently broken. This is not obvious for a large area, but for small particles, the surface hyper-polarizability of a convex object plays an important role in generating second harmonic. Further to the shape of the particle, the hyperpolarizability can be further tuned by functionalizing the gold surface with a molecule that possess an intrinsic large molecular second order polarizability (hyperpolarizability β). Here we made use of a small molecule used in the third chapter of this thesis. $tBuAzoS_2$ (Figure 6-5a) is a molecule with a large dipole moment due to the presence of a donor/acceptor pair along an azobenzene core. It addition it possesses a S-S bond which will enable further chemistry in presence of gold: the S-S bond breaks to form S-Au covalent bond yielding functionalization of the gold cavity surface.[29,30] To this end, a solution of 1 mM of

tBuAzoS$_2$ was prepared in ethanol that contains with PS-gold particle. The gold capped polystyrene were functionalized during 24 hrs then drop casted onto a clean coverslip. The goal of this experiment was to evaluate if the functionalization of the gold half-capped particle could further enhance the SHG signal. Several scans were done for large clusters(10-20 spheres within each cluster), to have a good statistical distribution of the collected signal. Control experiments on bare gold cavities were also conducted to have a reference to compare the intensity change. In order to eliminate the large background signal the collected data were corrected to collect only the pure signal form the particles. The laser intensity was fixed at 10 mW. Several scan on different clusters shows a 60% increase of SHG signal for the cavities functionalized with the azo molecules (Figure 6-5b). Although preliminary, the functionalization of the surface with selected molecules enables enhancement of the SHG signal. Some effects must be investigated to evaluate the temperature raise and possible desorption of damages to the molecular monolayer.

6.4   Conclusion

In this chapter, we used our SHG microscope to probe particles, the surface of which were half-coated with gold. The preparation methods of such particles as well as the SHG experiments are presented. To investigate the gold coated particles nonlinear optical properties, several second harmonic maps were collected from individual particles. By comparing with corresponding SEM image, the polystyrene, which has zero contribution to second harmonic generation, was melted due to the LSPR induced by the 10 mW femto-second laser. Surface roughness appears to enhance the signal, and the polarization of the laser also changes the signal. Not only the distribution of SH, the polarization analysis was also conducted. Additional functionalization of the surface with molecule with high charge-transfer property molecule and show slight increase of the SHG signal arising from these hybrid particles.

6.5   References

(1) Campagnola, P. J.; Millard, A. C.; Terasaki, M.; Hoppe, P. E.; Malone, C. J.; Mohler, W. A. *Biophys. J.* **2002**, *82*, 493-508.

(2) Brown, E.; McKee, T.; diTomaso, E.; Pluen, A.; Seed, B.; Boucher, Y.; Jain, R. K. *Nat Med.* **2003**, *9*, 796-800.

(3) Zoumi, A.; Yeh, A.; Tromberg, B. J. *PNAS.* **2002**, *99*, 11014-11019.

(4) Zipfel, W. R.; Williams, R. M.; Christie, R.; Nikitin, A. Y.; Hyman, B. T.; Webb, W. W. *PNAS.* **2003**, *100*, 7075-7080.

(5) Campagnola, P. J.; Wei, M. D.; Lewis, A.; Loew, L. M. *Biophys. J.* **1999**, *77*, 3341-3349.

(6) Sun, Y.; Chen, W. L.; Lin, S. J.; Jee, S. H.; Chen, Y. F.; Lin, L. C.; So, P. T. C.; Dong, C. Y. *Biophys. J.* **2006**, *91*, 2620-2625.

(7) Hsieh, C. L.; Grange, R.; Pu, Y.; Psaltis, D. *Biomaterials.* **2010**, *31*, 2272-2277.

(8) Yang, S. D.; Weiner, A. M.; Parameswaran, K. R.; Fejer, M. M. *Opt. Lett.* **2005**, *30*, 2164-2166.

(9) Shen, Y.-R. *Principles of nonlinear optics*; Wiley-Interscience: New York, USA, 1984.

(10) Butet, J.; Russier-Antoine, I.; Jonin, C.; Lascoux, N.; Benichou, E.; Brevet, P. F. *Nano Lett.* **2012**, *12*, 1697-1701.

(11) Czaplicki, R.; Husu, H.; Siikanen, R.; Makitalo, J.; Kauranen, M.; Laukkanen, J.; Lehtolahti, J.; Kuittinen, M. *Phys. Rev. Lett.* **2013**, *110*.

(12) Kim, E.; Steinbruuk, A.; Buscaglia, M. T.; Buscaglia, V.; Pertsch, T.; Grange, R. *ACS Nano.* **2013**, *7*, 5343-5349.

(13) Dadap, J. I.; Shan, J.; Heinz, T. F. *JOSA B.* **2004**, *21*, 1328-1347.

(14) Hua, X. M.; Gersten, J. I. *Phys. Rev. B.* **1986**, *33*, 3756.

(15) Švorčík, V.; Kvítek, O.; Lyutakov, O.; Siegel, J.; Kolská, Z. *Appl. Phys. A.* **2011**, *102*, 747-751.

(16) Sandrock, M. L.; Pibel, C. D.; Geiger, F. M.; Foss, C. A. *J. Phys. Chem. B.* **1999**, *103*, 2668-2673.

(17) Hulteen, J. C.; Vanduyne, R. P. *J. Vac. Sci. Technol., A.* **1995**, *13*, 1553-1558.

(18) Galarreta, B. C.; Harté, E.; Marquestaut, N.; Norton, P. R.; Lagugné-Labarthet, F. *PCCP.* **2010**, *12*, 6810-6816.

(19) Ashwell, G. J.; Hargreaves, R. C.; Baldwin, C. E.; Bahra, G. S.; Brown, C. R. *Nature.* **1992**, *357*, 393-395.

(20) Chen, Z.; Chen, W.; Zheng, J.-b.; Wang, W.-c.; Zhang, Z.-m. In *Laser Spectroscopy VII*; Springer: 1985, p 324-325.

(21) Lalama, S. J.; Garito, A. F. *Phys. Rev. A.* **1979**, *20*, 1179.

(22) Oudar, J.-L.; Chemla, D. *J. Chem. Phys.* **1977**, *66*, 2664-2668.

(23) Blanchard-Desce, M.; Runser, C.; Fort, A.; Barzoukas, M.; Lehn, J.-M.; Bloy, V.; Alain, V. *Chem. Phys.* **1995**, *199*, 253-261.

(24) Levine, B. *Chem. Phys. Lett.* **1976**, *37*, 516-520.

(25) Fayyaz, S.; Tabatabaei, M.; Hou, R. J.; Lagugne-Labarthet, F. *J. Phys. Chem. C.* **2012**, *116*, 11665-11670.

(26) Fang, Z. Y.; Zhen, Y. R.; Neumann, O.; Polman, A.; de Abajo, F. J. G.; Nordlander, P.; Halas, N. J. *Nano Lett.* **2013**, *13*, 1736-1742.

(27) Salomon, A.; Zielinski, M.; Kolkowski, R.; Zyss, J.; Prior, Y. *J. Phys. Chem. C.* **2013**, *117*, 22377-22382.

(28) Dadap, J. I.; Shan, J.; Eisenthal, K. B.; Heinz, T. F. *Phys. Rev. Lett.* **1999**, *83*, 4045-4048.

(29) Snell, K. E.; Hou, R.; Ishow, E.; Lagugné-Labarthet, F. *Langmuir.* **2015**, *31*, 7296-7305.

(30) Snell, K. E.; Mevellec, J. Y.; Humbert, B.; Lagugné-Labarthet, F.; Ishow, E. *ACS Appl. Mater. Interfaces.* **2015**, *7*, 1932-1942.

Chapter 7

7   Probing the effects of the size and symmetry of metastructures with SHG

This chapter focuses on the SHG signal generated from nanoparticles with different size and symmetry. Electron beam lithography was used to fabricate series of gold structures with a range of size and shapes. Such ensemble of structures varying from triangles (no center of inversion) to disks (with a center of inversion) were designed as arrays with varied size and variation of the roundness of the triangle apices. Second harmonic signal are collected from these nanostructures the size of which varies from 200 nm to 1.2 μm (triangular base size), and from triangular to circular shape. Furthermore, in order to investigate the relationship between the individual structure (the metamolecule) and the overall structure (the metastructure), we have investigated fractals structures. Sierpinski structures were fabricated and studied by SHG to possibly reveal the presence of hot spots.

7.1   Introduction

As mentioned in the previous chapters, the possibility of fabricating metallic structures with nanometer dimensions has led to the development of a new field in physics where the tuning and the manipulation of the surface geometry and optical properties become possible. The resulting localized surface plasmon resonances can be tuned from visible to near-infrared region by changing the nanoparticle's size, shape, thickness, periodicity or material of individual particles which can be done reproducibly with advanced micro- and nano-fabrication methods. Nanorods[1], spheres[2], pyramids[3], triangles[4] and other shapes[5] are wisely selected and studied by scientists experimentally. Second harmonic generation is a technique of choice since it is sensitive to the local symmetry of the structure.

In this chapter we are investigating the relationship between SHG signal and geometry transition from triangle space group to disk space group. Structures were made by electron-beam lithography with a variation of size and shapes. Another pattern with D_3

symmetry was investigated as well. The Sierpinski nanotriangles was also fabricated by EBL, on a thick glass cover slip. This unique fractal array is named after Wacław Sierpiński (1882-1969) who was a Polish mathematician, to honor his contributions to set theory, number theory, theory of functions and topology. The fractal structures have attracted growing attention from both experimentally and theoretically aspects.[6-9] Among them, Sierpinski triangles have become an interesting conceptual type of fractals used in many fields, including computer science and biology.[10,11] Due to its specific arrangement of individual triangles, this fractal structure has a D_3 symmetric element in every order of structure. The coupling between each repetitive individual element of the structure presumably affect the optical property of the whole structure.

In this chapter, we mainly focus on investigating the optical properties of nanoparticles with three-fold symmetry. To evaluate the effect of symmetric element's changing, several nanoparticles with different size and shape was designed, and fabricated by electron beam lithography (EBL). Theses nanoparticles started from a triangular shape and undergoes sequential morphological changes until they have a disk shape. This changes is performed in 6 distinct steps. The purpose of this design was to decrease the D_3 symmetry gradually. Our SHG microscope was used to study the nonlinear signal from these structures. Several SHG maps were presented. By rotating the polarization of the fundamental wave, some of the nanoparticles showed a clear response of this change. The nonlinear signals from Sierpinski triangles are also reported.

This is an on-going project currently taking place in Lagugné's research group. The purpose of introducing Sierpinski nanotriangles is to study its linear and nonlinear properties in visible and near IR range. In the future, the Sierpinski nanotriangles can be used for other spectroscopy applications such as in surface enhanced Raman spectroscopy (SERS) and surface enhanced IR absorption (SEIRA) platforms due to its possible multi bands absorption arising from the fractal-type structure. In this chapter only SHG measurements are presented meanwhile other members of Lagugné's group are studying the potential of the same structure for SEIRA and SERS applications.

7.2 Experimental methods

7.2.1 Electron beam lithography

Electron beam lithography (EBL) was used to produce the arrays of gold nanostructures, offering high reproducibility down to a 20 nm spatial resolution.[12] Glass cover-slips were first cleaned with a plasma cleaner. A positive photoresist (PMMA) thin film was first spin-coated on the coverslip. A thin conductive layer (AquaSAVE, Mitsubishi Rayon America) was then spin-coated over the photoresist to avoid charging effects and loss of the resolution due to electrons flowing out of the irradiated area. The nanoscale structures were designed using a CAD software and then inscribed on the coverslip/photoresist surface using a LEO 1530 Field Emission scanning electron microscope (SEM) combined with a high precision interferometric stage. The conductive layer was dissolved and the underlying photoresist was developed. Thin films of 3 nm titanium and 20 nm gold layers were deposited by e-beam evaporation.

In this chapter, two patterns are studied. The first one is designed to study the size and shape dependence of second harmonic generation from gold nanoparticles, shown in Figure 7-1. On this array, the triangles undergo morphological change to disks shape defined by 15 points in CAD design, from left side to right. Due to the limited precision of electron beam lithography, the 15 points will be able to create a perfect circle, listed in the very right column in Figure 7-1. Meanwhile, the size of the structure are changed in each row. At the bottom row the triangles are designed to be 200 nm side length, with a 200 nm increase until the top row reach a size of 1.2 μm. However, it is difficult to make the nanoparticles with the exact designed dimensions so the structures are undersized by about 10%, which is verified by SEM. Even though, the symmetric properties are not affected. It is worthy to point out that for the very right column, the circular structures are modified from corresponding triangles. Under this situation, the circular particles are much smaller than ideally designed sizes. For example, the top right circular one should be less than 1.2 μm diameter but in order to help compare with the same size family, that particle is still named as 1.2 μm circle. To help express this comparison, the bottom left particle (triangle with 200 nm base) can be referred as sample (1,1), while the top right

disk (1. 2 μm diameter) can be referred as sample (6,6). The center-center spacing for each nearby particle is 2 μm.
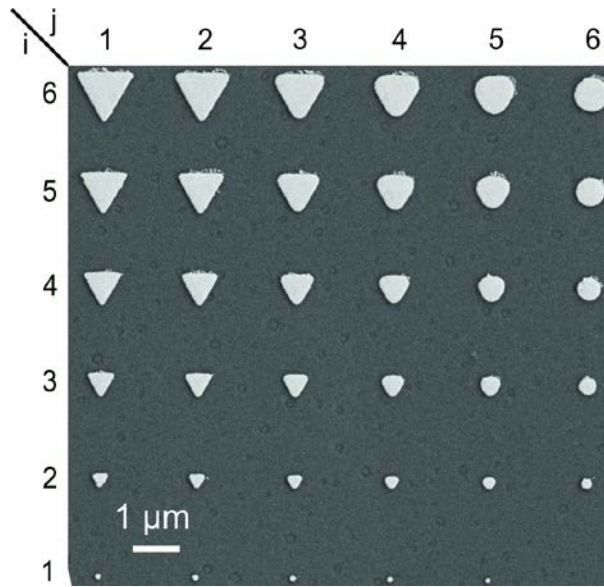
Figure 7-1: Sample A used to investigate the second harmonic generation dependence from gold nanoparticles varying shape and size.
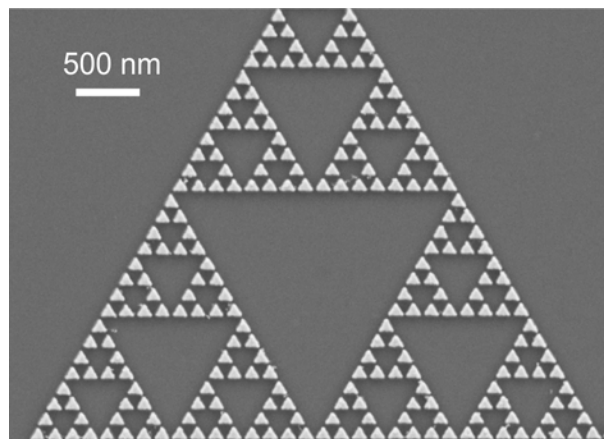
Figure 7-2: SEM image of fabricated Sierpinski nanotriangles (Sample B).

The Sierpinski fractal (Sample B), are also fabricated by EBL onto glass coverslips. The lowest (0th) order are selected to be composed with triangles in 125 nm side length. In total 8 orders of structure are designed including the 0th. In Figure 7-2 only 6 orders are shown, to present a detail structure of a single triangle. Further, in order to use Sierpinski

nanotriangles as SEIRA platform, this pattern needs to be inscribed onto IR-compatible optical windows such as CaF$_2$.

7.2.2   Second harmonic generation microscopy

The SHGM described in Chapter 5 is used.

7.3   Preliminary results and discussion

7.3.1   Size and symmetry dependent of second harmonic generation.

Sample A is first studied to see how the nonlinear signal varies with the change in size and shape of the nanoparticles. While the power of fundamental wave set to 10 mW, a strong SHG signal can be detected from these nanostructures (Figure 7-3). The output second harmonic is not depolarized, so Figure 7-3(a)(b) shows the sum intensity distribution over the array. The resolution was set to be 65 nm in both x and y axis, for a (13×13) μm^2 scan area.
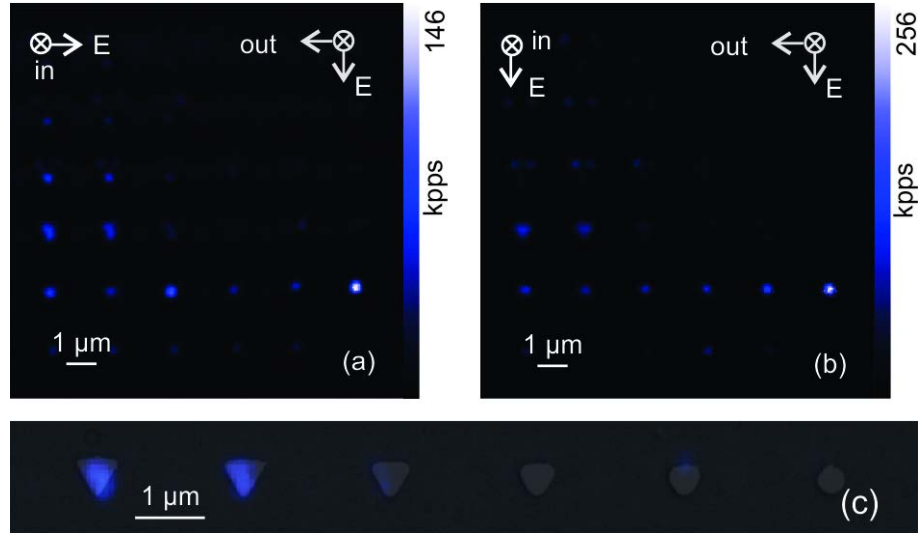

Figure 7-3: Generated second harmonic from the Sample A. The output second harmonic signal are detected for both polarization and summed. Nonlinear signal is excited by two orthogonal polarized fundamentals in (a) x-polarized and (b) y-polarized. (c) A superimposition of the SEM image and SHGM image from the same area.

It is clear that the lowest row, correspond to bottom row (1, j) particles, failed to give a relative strong second harmonic with respect to the upper structures (>400 nm). This unexpected weak signal is resulting from the localized surface plasmon resonance does not match the fundamental wavelength.[13] The positive electron beam resist PMMA are well known as it is widely suited for many applications. However for nanostructures under 200 nm, PMMA appears to be a limiting factor. Additionally, some of the bottom row particle, such as sample (1, 6), are missing because the circular particles are designed to be critically small. In other words, the bottom row reveals a lack of accuracy and is not reliable to yield reproducible results. Until the 400 nm row, these (2, j) particles, the second harmonic become clear. Noting that (2, 6) generates the strongest second harmonic in both (a) and (b) even (2,6) is a circular particle (Figure 7-4). That reproducible hot-spot is predicted due to the surrounded anomaly in Figure 7-4.
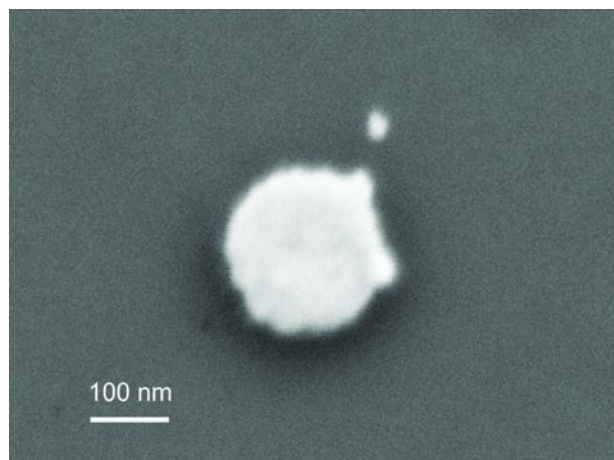
Figure 7-4: (2, 6) disk shaped gold particle with a desired diameter of 230 nm. Surface roughness can be clearly seen around the boundary.

An obvious trend can be observed from the (3, j) row: the second harmonic is decreasing while j increased. A superimposition is shown in Figure 7-3(c). According to the SEM image, the 600 nm array shows a good shape and well controlled by EBL. Triangles with D_3 symmetry do not have an inversion center. However, circular particles are centrosymmetric and will cancel the second order non-linear susceptibility elements.

Higher order contributions such as quadrupolar contributions may be observed but will yield a much weaker resulting SHG.

For larger particles, this SHG modification due to symmetry is similar. The trend of this array is obvious, that except the bottom row, the smaller particles tends to give a better second harmonic because the surface contribution from small particles is larger than in bigger particles, which will be dominated by bulk contribution. Triangular particles also exhibit a stronger SHG because the lack of inversion center.

Figure 7-5: Dependence of the input polarization direction for different particles with a variety of size/shapes. The rows from top row to bottom correspond to particles with 1.2 (6,6), 1.2 (6,1), 0.8 (4,1) and 0.4 (2,1) μm, respectively.

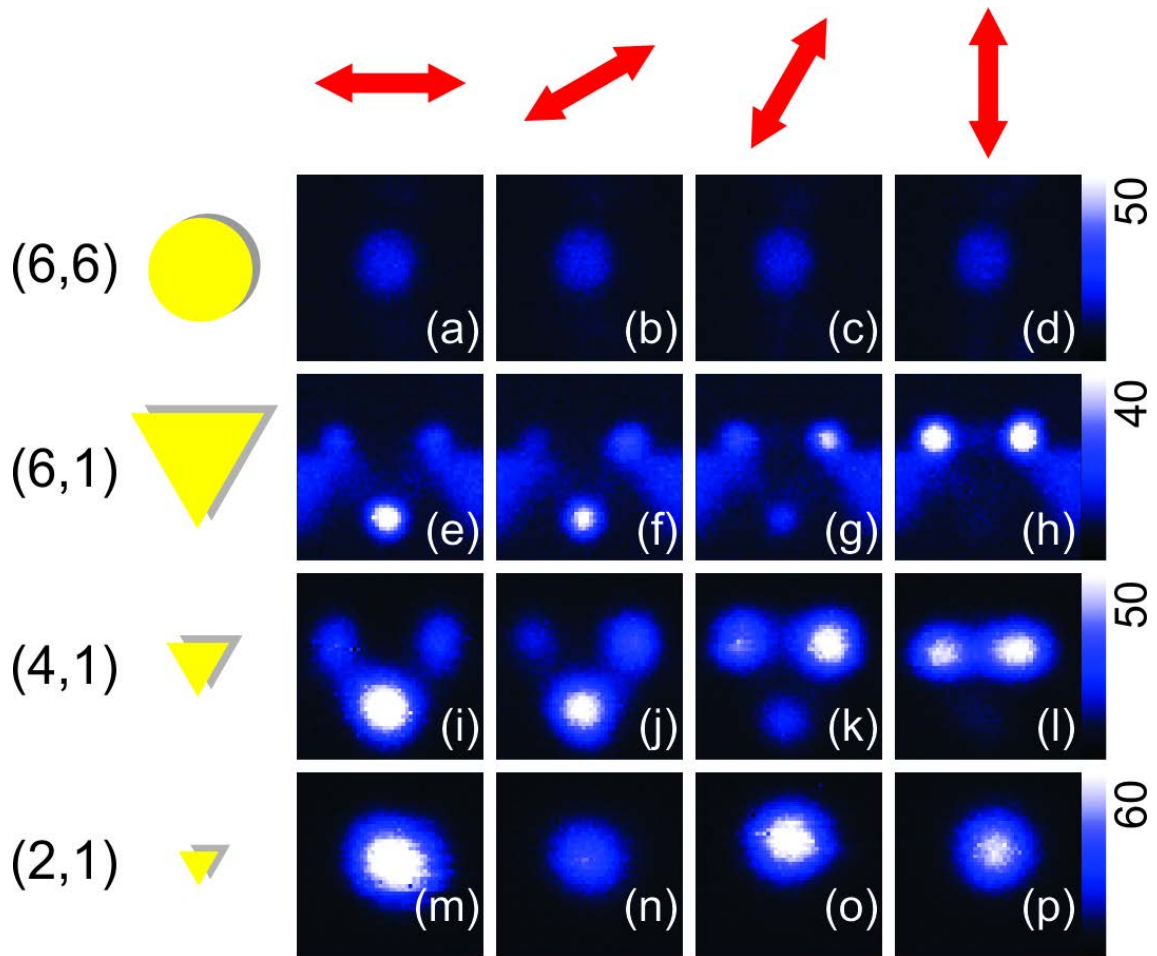In addition, starting from the (4, j) row, since the particle size increased to 800 nm, the high spatial resolution of this two-photon process allows one to distinguish the spatial location of the second harmonic generated from different positions within a single particle. The input polarization is switched from x-polarized (1st column in Figure 7-5) to y-polarized (last column in Figure 7-5). For a x-polarized fundamental, one intense and two weak SHG spots can be observed from the (4, 1) triangle. The top two apexes are much weaker than the bottom apex. Similarly, for a y-polarized input light, the bottom apex almost disappeared. This unique intensity distribution is carefully studied in Figure 7-5.

Several particles are selected here. SHG map from a 1.2 μm level circular particle (6, 6) is displayed from Figure 7-5(a) to (d), which appears to be independent of the input polarization. Due to it is centrosymmetric shape, the second harmonic is less intense than the following three rows. Both of the (6, 1) (Figure 7-5 e-h) represents in the 2nd row and (4, 1) (Figure 7-5 i-l) in the 3rd row have strong polarization dependence. It seems that the second harmonic always aligned in a direction orthogonal to the fundamental polarization. This is possibly due to the extinction resonance of these particles that are not within 800 nm, but in a near IR range. While irradiated at $\lambda= 800$ nm, different mode of electron oscillation can be excited on the surface of these triangular particle, and this localized surface plasmon resonance may further enhance the nonlinear signal. However, for nanotriangles with smaller size, the 400 nm triangle (2,1) (Figure 7-5 m-p) does not show a clear position shift of the second harmonic. It proves that for 800 nm fundamental, a larger nanoparticle (greater than 0.6 μm) will show several SHG active spots located at the apices of the triangular structure. To obtain a clear SH from a single particle, the size of such particle should be controlled below 600 nm side length for triangles.

7.3.2   Second harmonic generation from Sierpinski nanotriangles.

The extinction spectrum of a selected structure indicates what wavelength of the incident electromagnetic field should be selected for maximized interaction. For many near-IR

studies, a perfect platform with an extinction wavelength in the near IR range (750-5000 nm) is required. Usually the nanoparticle should be several μm size to have extinction peak at that range. However, it is strenuous to detect second harmonic from a large nanoparticle. Here, the fractal structures are proposed due to its multi-band extinction peak, and it is also composed by small sized nanoparticles.
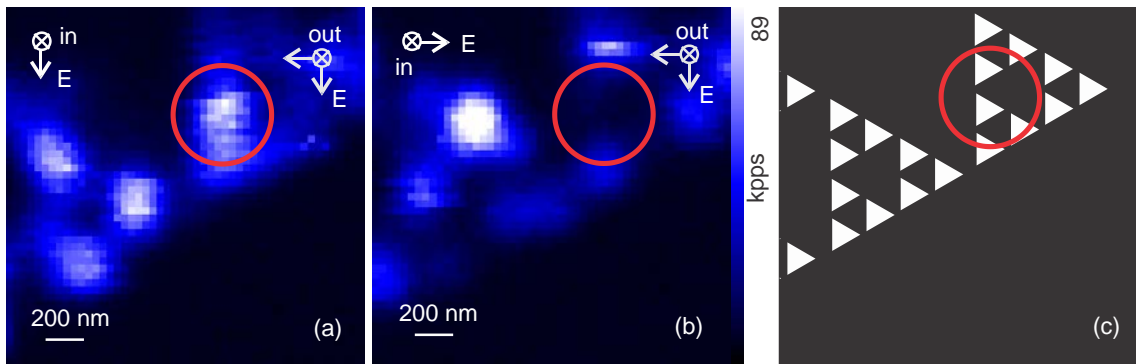
Figure 7-6: An SHG map of Sierpinski nanotriangles. These are 2×2 μm images taken from the same region, but with orthogonal fundamental polarization y (a) and a (b). A sketch of a possible probing area is described in (c).

Figure 7-6 shows two scans with orthogonal fundamental polarization on a (2×2) μm^2 area. A strong SHG signal can be observed from this nanostructure under 10 mW fundamental irradiation. The intense spots, forming a clear triangular shape while the input polarization is vertical (Figure 7-6a). For x-polarized fundamental, the SHG signals are distinct compared to those irradiated with y-polarized input (Figure 7-6b). Presumably, while the polarization is parallel to one side of the triangle, it tends to give out a better resonance, by enhancing the coupling between vertically aligned triangles.

For the smallest generation of triangles, the size being limited to 125 nm it is impossible to spatially resolve the individual triangles as expected. Taking into consideration that we are detecting a SHG signal at a wavelength of 400 nm with a microscope objective of 100x magnification and numerical aperture of N.A=0.95, the ideal lateral spatial would be about 250 nm. For Sierpinski nanotriangles, the structure size does not reach 250 nm

until Level 1. That implies it is inherently impossible to detect this 125 nm nanotriangle by using conventional optical detection, unless other techniques are used such as near field microscopy.[14]

Furthermore, the polarization dependence can also be investigated by carefully observing the gaps between the triangles. In the center of Figure 7-6b, vertically polarized laser connects the gap between two triangle prisms. Another series of scans are done to collect more information about the polarization dependence. In Figure 7-7, the polarization is changed to six directions: x-polarized or 0° (a), 30° (b), 60° (c), y-polarized or 90° (d), 120° (e) and 150° (f) with respect to the positive x-axis. The scan is over a (10×10) μm^2 area, shows several levels of this fractal pattern until Level 6. The resolution is set to be 100 by 100 pixels, with a minimum step 100 nm.

The red arrow (Figure 7-7) points to a gap between two Level 5 structures. In Figure 7-7(a), since the polarization is x-polarized, the gap exhibits as a dark area. While rotating the polarization to vertical, the coupling shows up (d). The mapping of this hot-spot is related to the coupling which is sensitive to the fundamental polarization. The hot-spots are the enhanced area due to the LSPR. The interaction of input electromagnetic wave and nanoantennas created an enhanced electric field, that can significantly increase the nonlinear signal. Because the nonlinear signal is proportional to the square of the input field, the enhancement of this localized phenomenon can be observed. Compared to other ways of mapping hot spots, here SHG requires no other additional over layer on the metal substrates.[15] Similar hot spots can be seen when the polarization is along the apex direction, in Figure 7-7 (a) to (f).
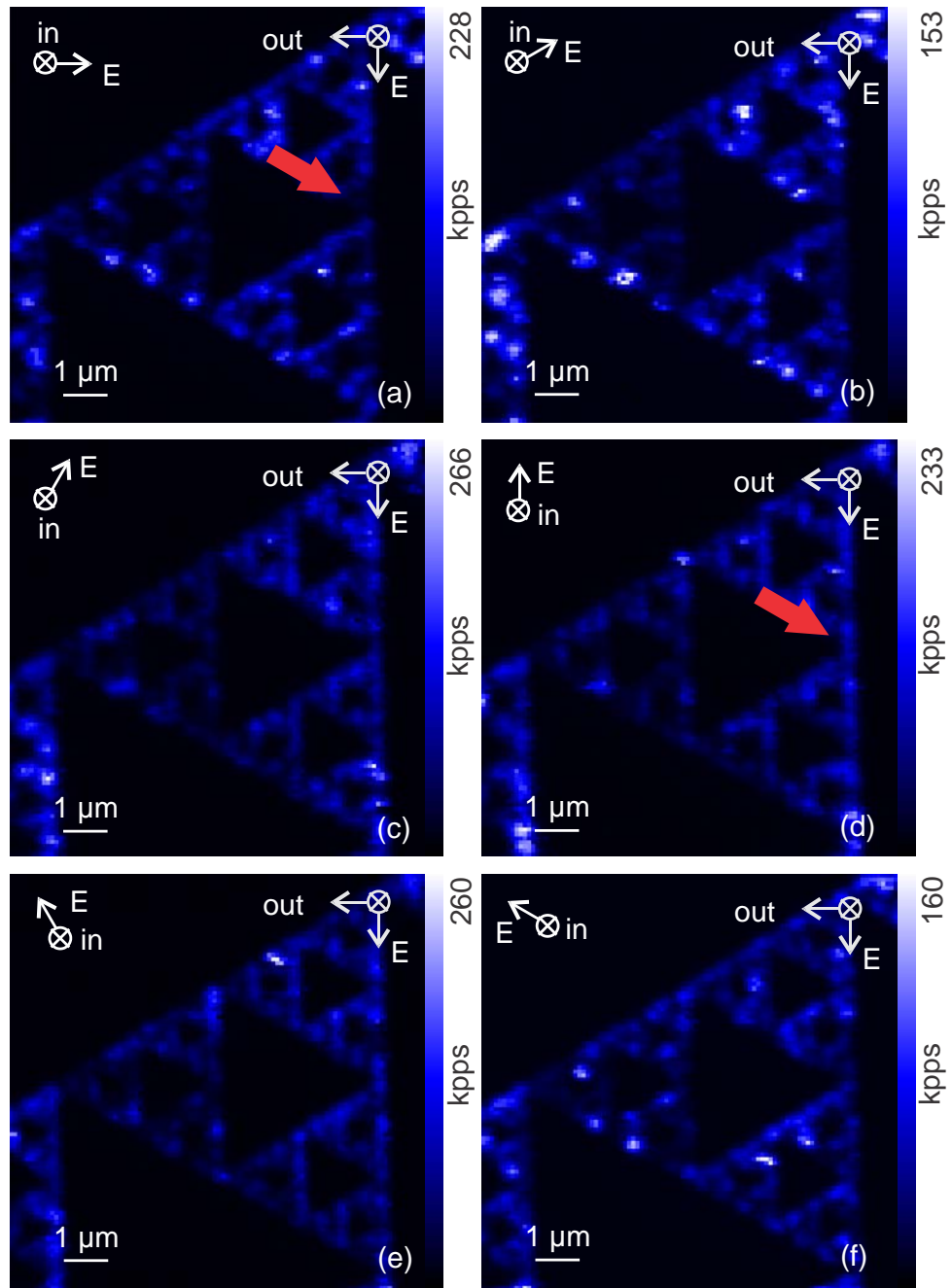
Figure 7-7: Tuning the polarization direction allows one to collect details information revealing area that are strongly dependent of the polarization while other areas are less influenced by the input polarization.

7.4 Conclusion and future work

In this chapter, we have conducted preliminary work using second harmonic generation to probe metallic nanostructures with variable size and symmetry. Increasing size reduces the nonlinear signal. For nanotriangles with side length above 600 nm, the particle itself will not behave as a single SHG source anymore. We have also presented that symmetry also plays an important role due to the lack of inversion center that yield SHG active structures. The tuning of the polarization can be used to tune the spatial distribution of second harmonic emission generated from surface of large nanoparticles.

Non-centrosymmetric particles like triangles can be selected as good SHG-active structures. As a potential multi-usage platform, Sierpinski triangles are also studied. Some preliminary results are shown. These fractal structures can be imaged by SHGM down to 250 nm structure (Level 1). Strong nonlinear signal can be observed from these nanostructures. We are convinced that Sierpinski triangles can be a good substrate for SHG detection. The second harmonic distribution can be changed if another fundamental polarization is used. This pattern can also be used to study the localized enhanced electric field by imaging the hot spots.

In future work, Sierpinski fractals can be used as interesting platforms due to their multi-band extinction peaks. The extinction spectrum can be first simulated and experimentally measured, for both UV-vis and IR range. Knowing its extinction range will help us to understand its linear optical properties, in order to use that in other applications such as SERS and SEIRA.

7.5 References

(1) Wu, C.; Xu, Q.-H. *Langmuir.* **2009**, *25*, 9441-9446.

(2) Chen, C. Y.; Wang, J. Y.; Tsai, F. J.; Lu, Y. C.; Kiang, Y. W.; Yang, C. C. *Opt. Express.* **2009**, *17*, 14186-14198.

(3) Cui, B.; Clime, L.; Li, K.; Veres, T. *Nanotechnology.* **2008**, *19*, 145302.

(4) Moran, A. M.; Sung, J.; Hicks, E. M.; Van Duyne, R. P.; Spears, K. G. *J. Phys. Chem. B.* **2005**, *109*, 4501-4506.

(5) Nehl, C. L.; Hafner, J. H. *J. Mater. Chem.* **2008**, *18*, 2415-2419.

(6) Stockman, M. I.; Pandey, L. N.; Muratov, L. S.; George, T. F. *Phys. Rev. Lett.* **1994**, *72*, 2486-2489.

(7) Drachev, V. P.; Bragg, W. D.; Podolskiy, V. A.; Safonov, V. P.; Kim, W.-T.; Ying, Z. C.; Armstrong, R. L.; Shalaev, V. M. *J. Opt. Soc. Am. B.* **2001**, *18*, 1896-1903.

(8) Stockman, M. I. *Phys. Today.* **2011**, *64*, 39-44.

(9) Dong, J.; Gong, J.; Liu, J.; Chen, M.; Yan, X. *Electrochim. Acta.* **2012**, *60*, 264-268.

(10) Taentzer, G.; Biermann, E.; Bisztray, D.; Bohnet, B.; Boneva, I.; Boronat, A.; Geiger, L.; Geiß, R.; Horvath, Á.; Kniemeyer, O. In *Applications of Graph Transformations with Industrial Relevance*; Springer: 2007, p 514-539.

(11) Rothemund, P. W.; Papadakis, N.; Winfree, E. *PLoS Biol.* **2004**, *2*, e424.

(12) Manheller, M.; Trellenkamp, S.; Waser, R.; Karthauser, S. *Nanotechnology.* **2012**, *23*.

(13) Zoric, I.; Zach, M.; Kasemo, B.; Langhammer, C. *ACS Nano.* **2011**, *5*, 2535-2546.

(14) Huang, B.; Bates, M.; Zhuang, X. *Annu. Rev. Biochem.* **2009**, *78*, 993.

(15) Fayyaz, S.; Tabatabaei, M.; Hou, R.; Lagugné-Labarthet, F. *J. Phys. Chem. C.* **2012**, *116*, 11665-11670.

Chapter 8

8   Conclusions and prospects

In this thesis, we have investigated both linear and nonlinear optical properties of several anisotropic samples, and developed two home-built instruments. The main emphasis here was to manipulate the nanoscale features, as well as optimizing the sensitivity, precision and resolution of detection methods. The electron donor-acceptor chromophore-containing glass shows photoinduced anisotropy to a change of molecular orientation upon irradiation with polarized light. Metallic structures are then characterized using second harmonic generation microscopy. Here we have evaluated the role of the symmetry and the local anisotropy of several structures on the resulting second harmonic signal.

The experimental details of polarization modulation infrared linear dichroism spectroscopy (PM-IRLD) were described in Chapter 2. The use of a photo-elastic modulator allows one to modulate the polarization of an IR beam that yields a differential signal proportional to the linear dichroism of a thin film sample. Calibration method of the IR signal is presented to provide a normalized signal. Compared to standard polarized FT-IR measurements, the fast response of PM-IRLD makes the study of molecular orientation in real-time possible as reported in Chapter 3 for glassy thin films. A polarized pump light induces orientation of the different key infrared active vibrational groups of a series of azobenzene-containing glasses, in order to estimate their anisotropy during cycles of orientation, relaxation and erasure. Similar molecules were later used in conjunction with plasmonic platforms to enhance second harmonic generation, by using molecules with large quadratic hyperpolarizabilities. Importantly, we show that the orientation of these push-pull molecules has a higher rate in glassy materials compared to polymers functionalized azobenzene molecules. Increase of the orientation up to a 7 fold factor is reported, indicating that the right set of donor-acceptor substituents can revive applications such as in optical data storage applications or fast-response photochromic glasses.

Chapter 4 is a second harmonic generation study from several gold nanostructures. Nanostructures with three-fold symmetry are designed and fabricated by electron beam lithography (EBL). The measured extinction peak shows that this structure is in resonance with the incident laser. Some Finite Difference Time Domain simulated extinction spectra were compared to confirm the effect of the rounding of the apices of the triangular structures yielding more accurate results. The nonlinear signal is collected from the metallic structure by second harmonic generation microscopy. The SHG maps show a distinguishable strong signal from each triangle. The polarization analysis from these nanotriangles shows a four-lobes pattern, that corresponds to a three-fold symmetry, highlighting the symmetry-dependence of the nonlinear signal. The coupling between the nanostructures can be further tailored and could result in more complex coupling between adjacent structures.

The design, fabrication and testing of a home-built second harmonic generation microscope is also described in terms of hardware and software and presented in Chapter 5. The standard operating protocol is also provided in the appendix section. A new class of non-centrosymmetric nanoparticles is presented and studied with this apparatus in Chapter 6. The fabrication approach is based on nanosphere lithography methods yielding half-coated gold particles, which presumably enhance optical second order nonlinearities. This approach is capable in producing large quantity of SHG active nanoparticles. The polystyrene spheres can further be vaporized by the focusing a femtosecond laser, while a gold cap is left on the surface. Drastic enhancement of second harmonic signal from the surface roughness is observed. A new possibility of modification of the metallic surface with a molecular monolayer is discussed. Using the molecules with electron donor-accepter group studied in Chapter 3, the surface hyperpolarizabilities can be slightly enhanced. The monolayer on the gold caps successfully increased the second harmonic signal by approximately 60%.

The size and symmetry dependence of metallic nanostructure on the SHG signal is discussed in Chapter 7. EBL is used to fabricate an array of triangular and circular structures with variable dimensions. This series of experiments prove that the non-centrosymmetric particles enhanced the nonlinear signal because the non-vanishing $\chi^{(2)}$

term. The mapping of SHG from the metallic triangles with different sizes shows that for the structures larger than 600 nm the SHG signal can be confined in specific parts of the structure. Due to its fractal-like geometry, Sierpinski structures are selected as potential platforms with SHG properties in addition to other potential in other surface-enhanced spectroscopy methods. The polarization dependence from the triangles is investigated which also shows the ability to image the hot-spots between the triangles corresponding to the local near-field coupling.
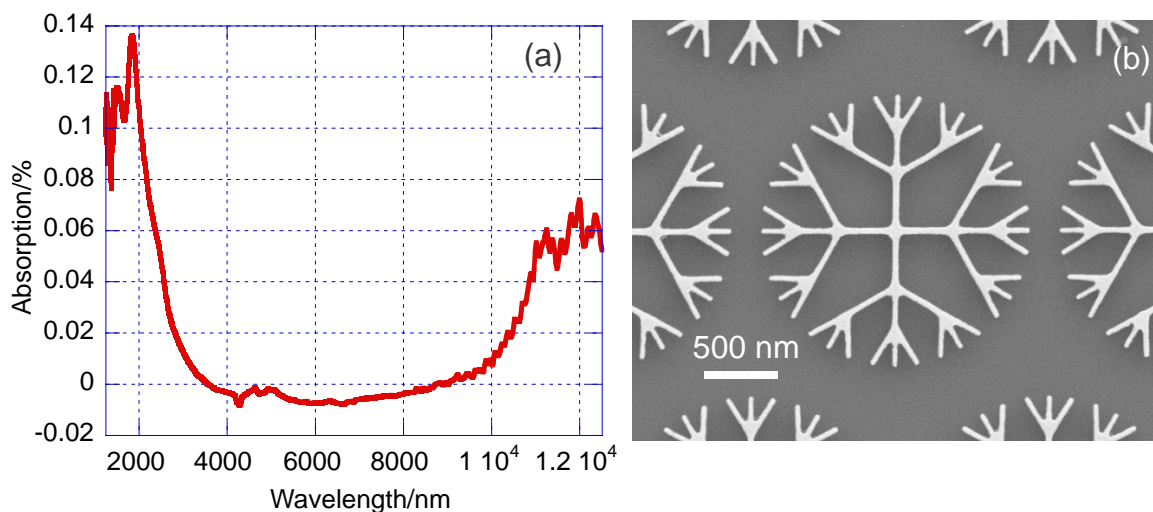

Figure 8-1: (a) Extinction spectrum of Sierpinski triangles. (b) One of the designed fractal pattern, which can be possibly used as enhanced SERS/SIERA platform.

Further research on this these nanostructures triangles needs to be done to uncover the potential of these platforms. Several non-centrosymmetric patterns similar to Sierpinski triangles are also designed and studied in other groups.[1] Not limited to Sierpinski triangles, other fractal patterns such as the Cayley[2]/Ternary tree[3], are also investigated due to their possible application as multi-usage platform. Several experiments presently conducted in Lagugné's lab are focusing on the further optical properties of some similar fractal pattern (Figure 8-1). The extinction spectra lead to further surface enhanced Raman spectroscopy as well as surface enhanced IR absorption studies (Figure 8-1a). A clear understanding of the optical properties of these multi-usage nano-platforms will open new applications in ultra-sensitive sub-wavelength and molecular level photonic sensing.

8.1   References

(1) Hasan, D.; Wang, J.; Lee, C. In *2016 IEEE 29th International Conference on Micro Electro Mechanical Systems (MEMS)*; IEEE: 2016, p 234-237.

(2) Gottheim, S.; Zhang, H.; Govorov, A. O.; Halas, N. J. *ACS Nano.* **2015**, *9*, 3284-3292.

(3) Hegde, R. S.; Khoo, E. *Plasmonics.* **2015**, 1-9.

Appendices

A   PM-IRLD and birefrigence studies

A.1   Sequential polarized measurements and uniaxial model
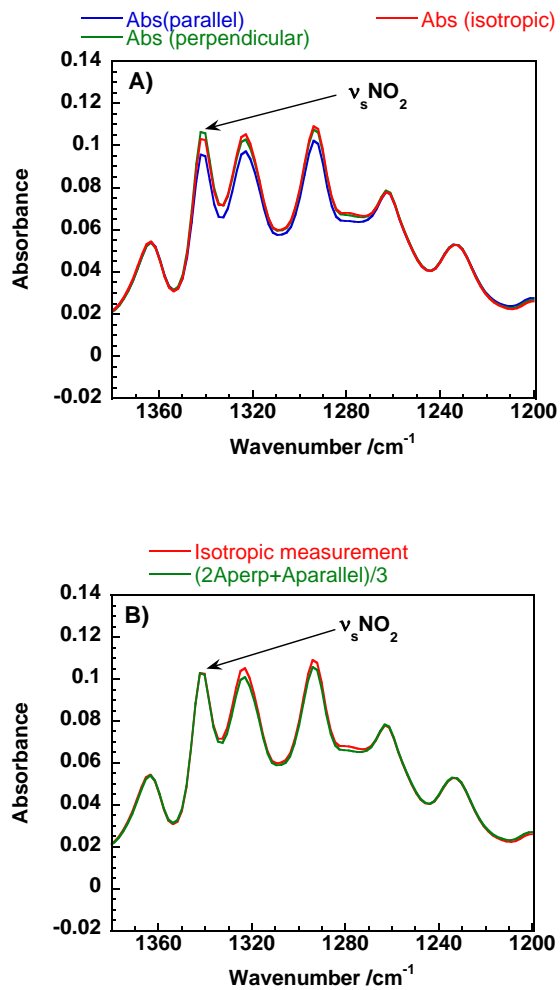

Figure A-1: (A) Polarized spectra of isotropic (before irradiation) and anisotropic (after irradiation) of a CarbNO$_2$ thin film. (B) Calculated isotropic spectrum from the polarized absorbances $A_{//}$ (A parallel) and $A_{\perp}$ (A perpendicular) using an uniaxial model $(2A_{\perp} + A_{//})/3$

A.2   tBuCN PM-IRLD spectra and dynamics

Figure A-2: (A, B) Infrared spectrum of a tBuCN molecular thin film and photoinduced linear dichroism at t = 0 min., after 60 min. of orientation and after 60 min. of relaxation. (C) Dynamics of selected vibrational modes such as the stretching mode of $C \equiv N$ (2225 cm^{-1}), stretching phenyl modes ν_{8a}, and ν_{8b} (1591 cm^{-1} and 1580 cm^{-1}), and coupled $\nu_{N=N}+\nu_{Ph-N}$ mode (1395 cm^{-1}) during irradiation and relaxation cycles.
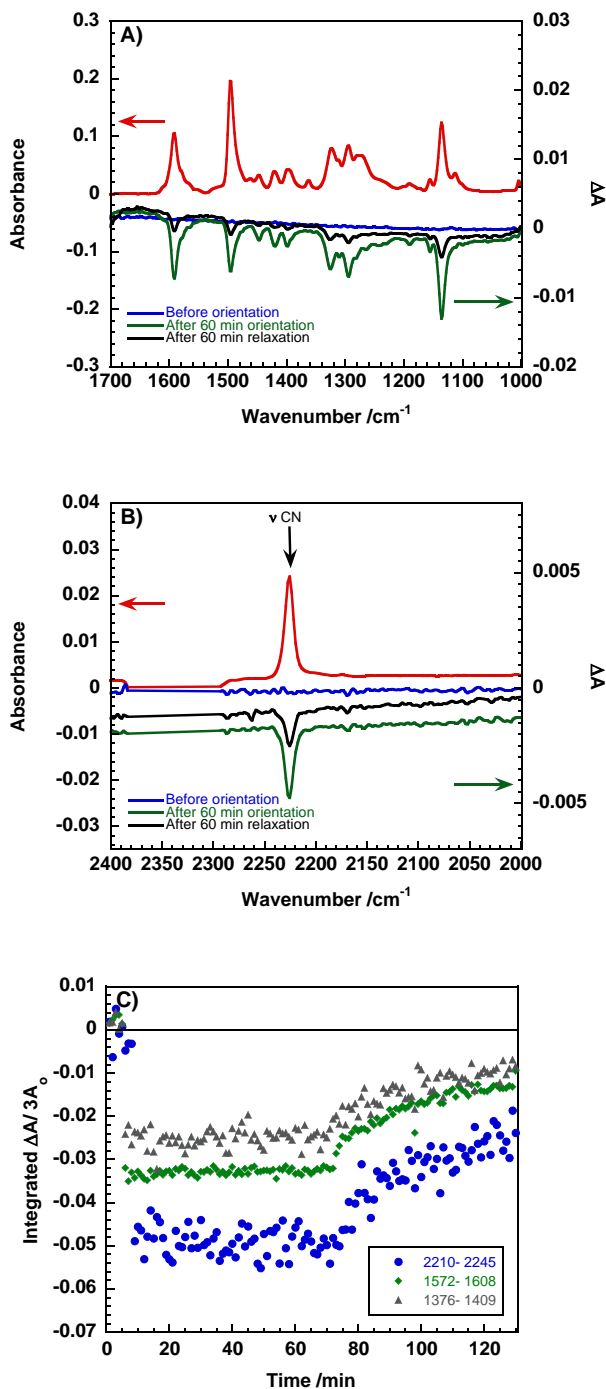
A.3 tBuCO$_2$ PM-IRLD spectra and dynamics

Figure A-3: (A) Infrared spectrum of a tBuCO$_2$Me molecular thin film and photoinduced linear dichroism at t = 0 min., after 60 min. of orientation and after 60 min. of relaxation. (B) Dynamics of selected vibrational modes such as the stretching mode of C=O (1722 cm^{-1}), stretching phenyl modes ν_{8a} (1590 cm^{-1}) and coupled $\nu_{N=N}+\nu_{Ph-N}$ mode (1395 cm^{-1}) during irradiation and relaxation cycles.
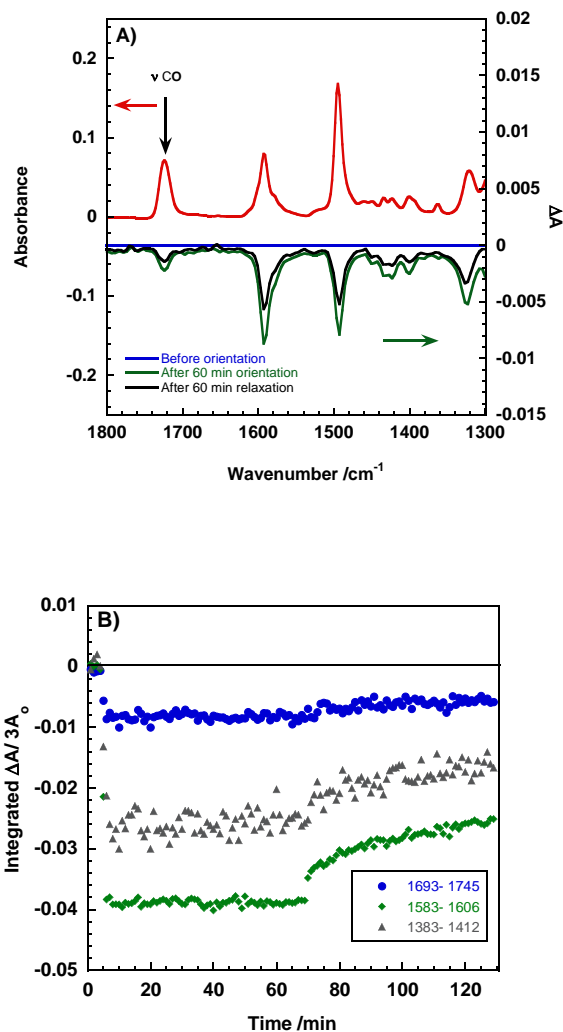
A.4 CarbCN PM-IRLD spectra and dynamics

Figure A-4: (A, B) Infrared spectrum of a CarbCN molecular thin film and photoinduced linear dichroism at t = 0 min., after 60. min of orientation and after 60. min of relaxation. (C) Dynamics of selected vibrational modes such as the stretching mode of $C \equiv N$ (2225 cm^{-1}), stretching phenyl modes ν_{8a} (1591 cm^{-1}), coupled $\nu_{N=N}+\nu_{Ph-N}$ mode (1395 cm^{-1}) and isotropic mode at 1362 cm^{-1}(unknown assignment) during irradiation and relaxation cycles.
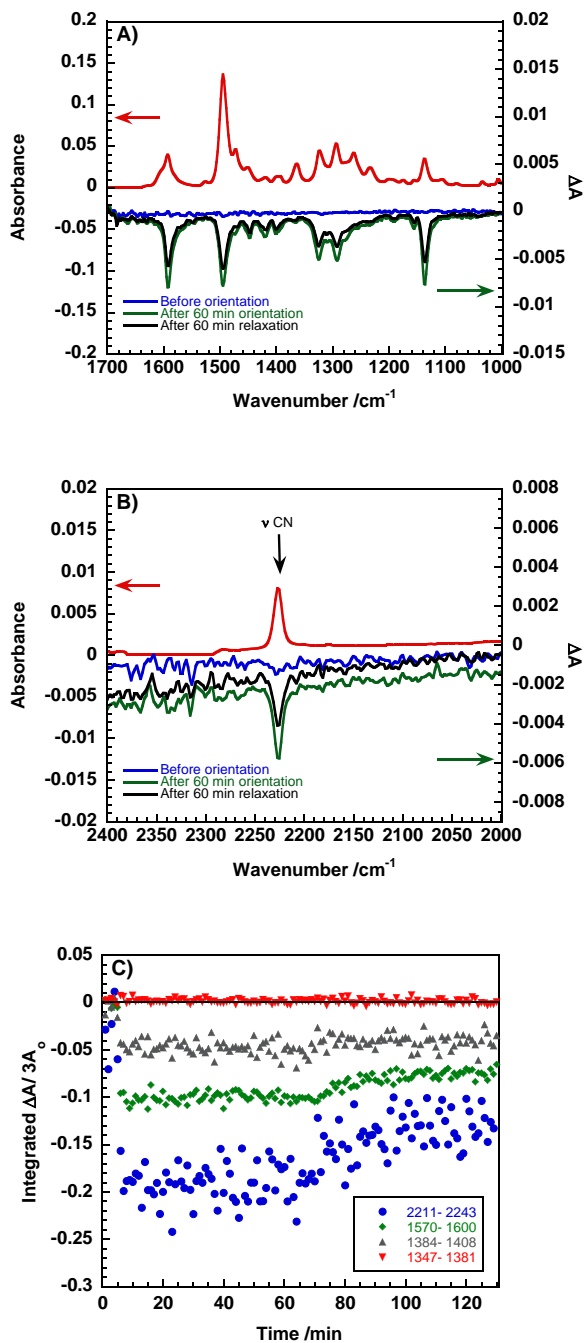
A.5 CarbCO$_2$Me PM-IRLD spectra and dynamics

Figure A-5: (A) Infrared spectrum of CarbCO$_2$Me molecular thin film and photoinduced linear dichroism at t = 0 min., after 60 min. of orientation and after 60 min. of relaxation. (B) Dynamics of selected vibrational modes such as the stretching mode of C=O (1725 cm^{-1}), stretching phenyl modes ν_{8a} (1590 cm^{-1}) and coupled $\nu_{N=N}+\nu_{Ph-N}$ mode (1395 cm^{-1}) during irradiation and relaxation cycles.

A.6 CF$_3$CN PM-IRLD spectra and dynamics

Figure A-6: (A, B) Infrared spectrum of a CF$_3$CN molecular thin film and photoinduced linear dichroism at t = 0 min., after 60 min. of orientation and after 60 min. of relaxation. (C) Dynamics of selected vibrational modes such as the stretching mode of $C \equiv N$ (2225 cm^{-1}), stretching phenyl modes ν_{8a} (1595 cm^{-1}), coupled $\nu_{N=N}+\nu_{Ph-N}$ mode (1395 cm^{-1}) and nearly isotropic mode at 1380 cm^{-1}(unknown assignment) during irradiation and relaxation cycles. CF modes do not shown any anisotropy.

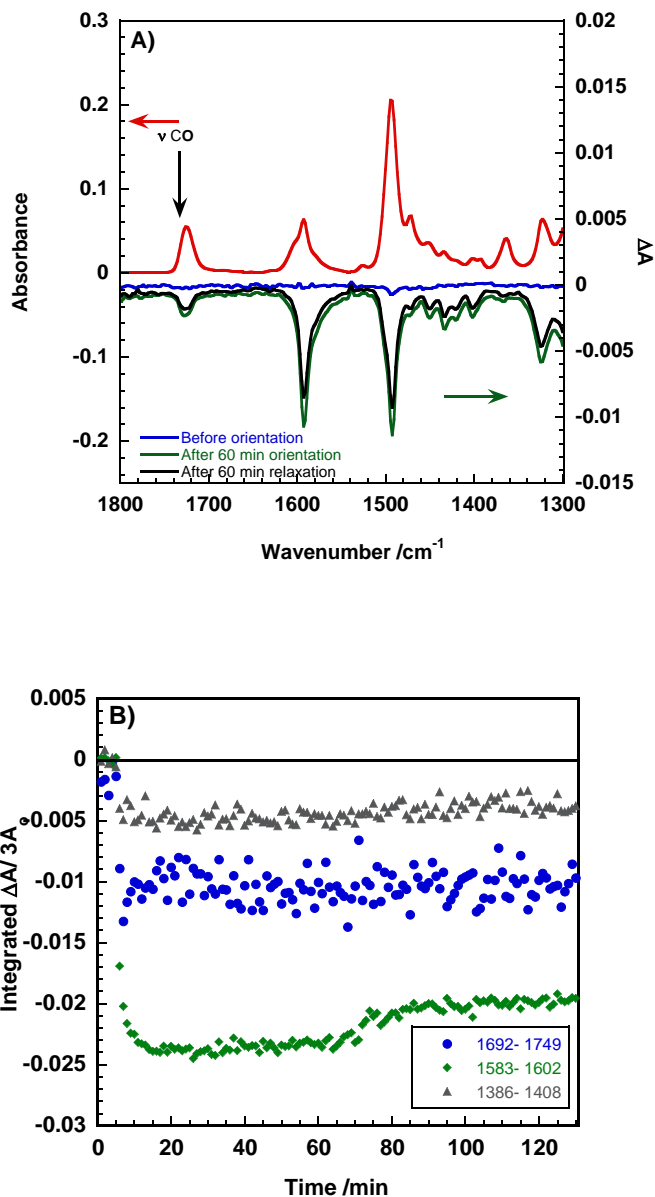## A.7 CF$_3$CO$_2$Me PM-IRLD spectra and dynamics

Figure A-7: A) Infrared spectrum of a CF$_3$CO$_2$Me molecular thin film and photoinduced linear dichroism at t = 0 min., after 60 min. of orientation and after 60. min of relaxation. (B) Dynamics of selected vibrational modes such as the stretching mode of C=O (1725 cm^{-1}), stretching phenyl modes ν_{8a} (1592 cm^{-1}) and coupled $\nu_{N=N}+\nu_{Ph-N}$ mode (1405 cm^{-1}) during irradiation and relaxation cycles.

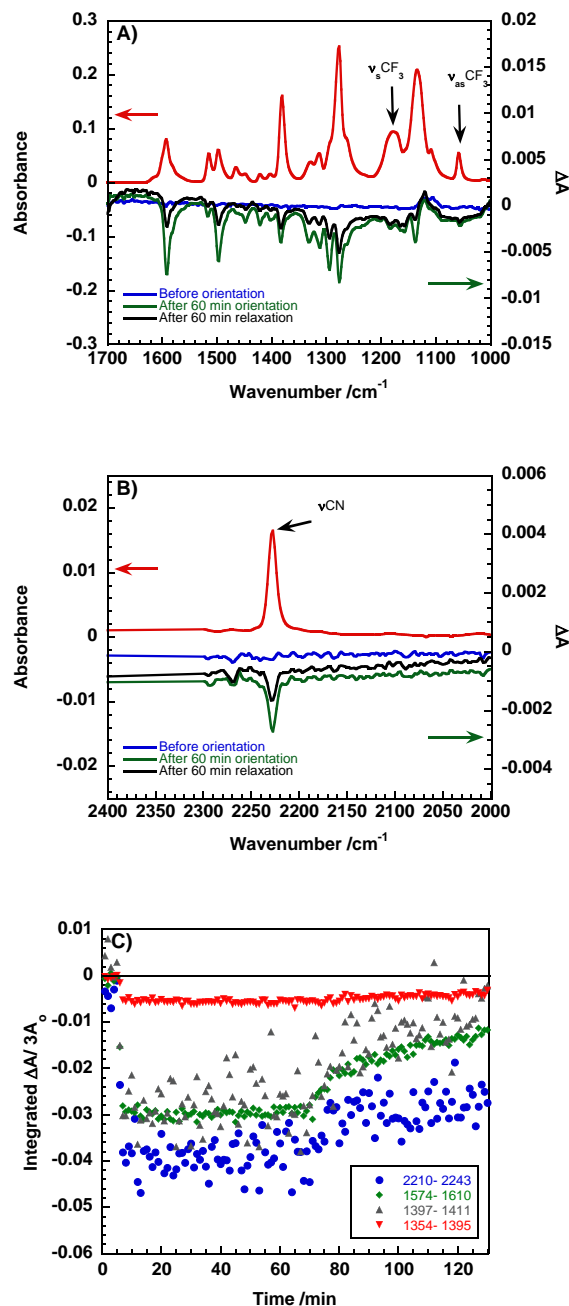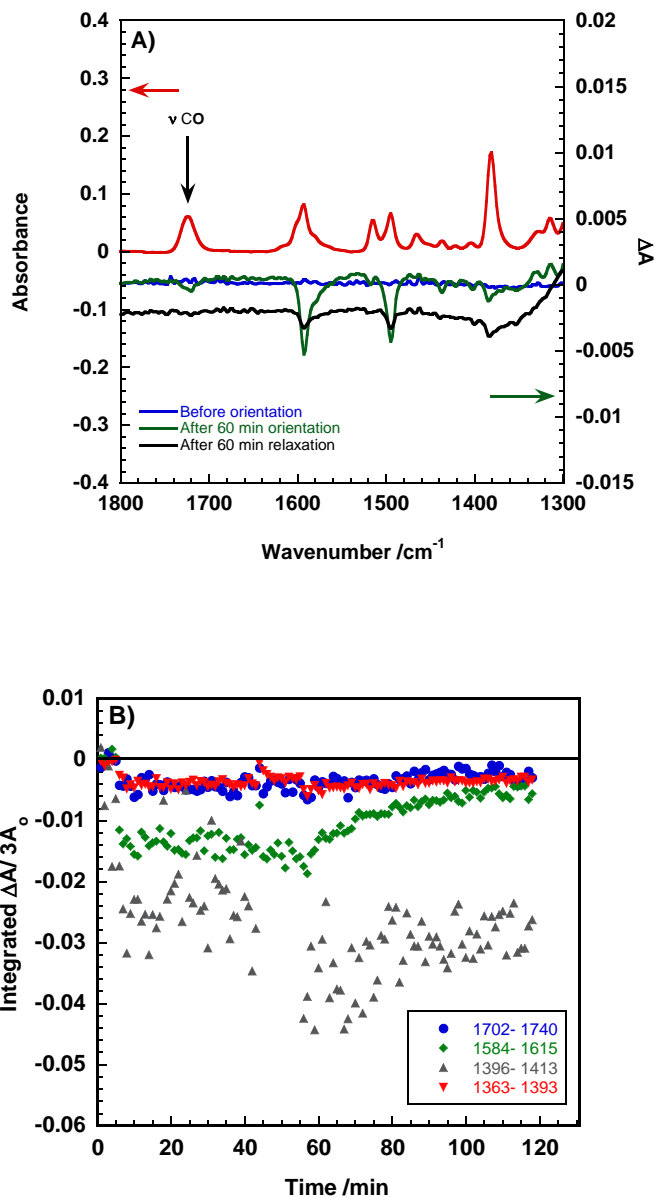## A.8   CF$_3$NO$_2$ PM-IRLD spectra and dynamics

Figure A-8: (A) Infrared spectrum of CF$_3$NO$_2$ molecular thin film and photoinduced linear dichroism at t = 0 min., after 60 min. of orientation and after 60 min. of relaxation. (B) Dynamics of selected vibrational modes such as the symmetric (ν_s, 1343 cm^{-1}) and antisymmetric (ν_{as}, 1515 cm^{-1}) stretching modes of NO$_2$, stretching phenyl modes ν_{8a}, and ν_{8b} (1605 cm^{-1} and 1588 cm^{-1}), and coupled $\nu_{N=N}+\nu_{Ph-N}$ mode (1402 cm^{-1}) during irradiation and relaxation cycles.

A.9   pDR1M PM-IRLD spectra and dynamics

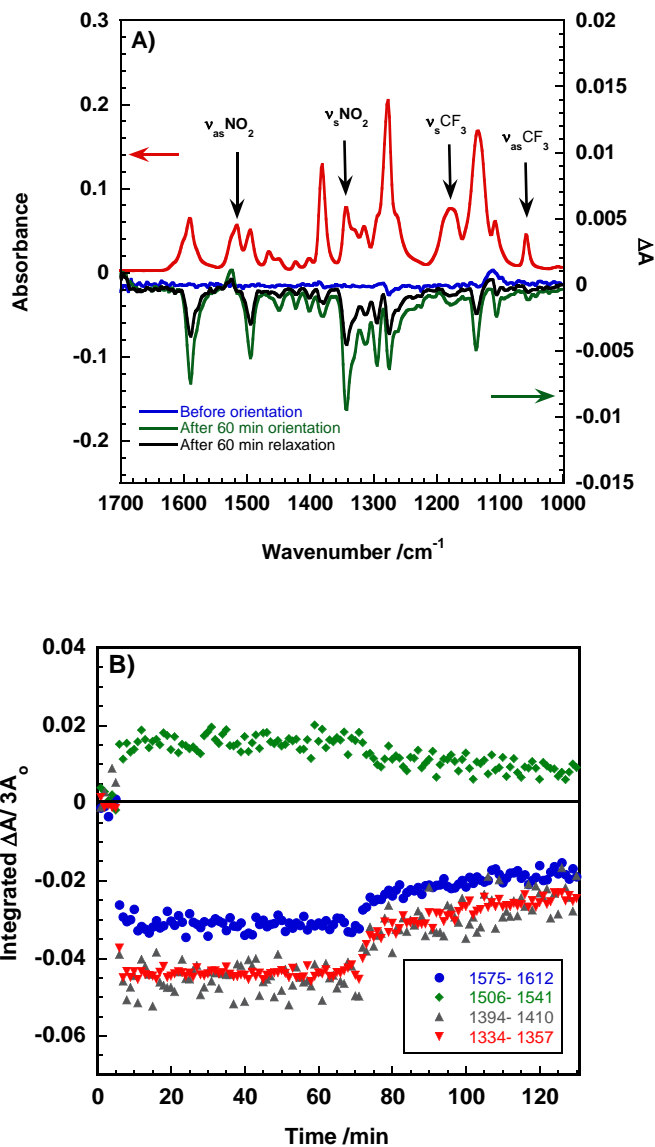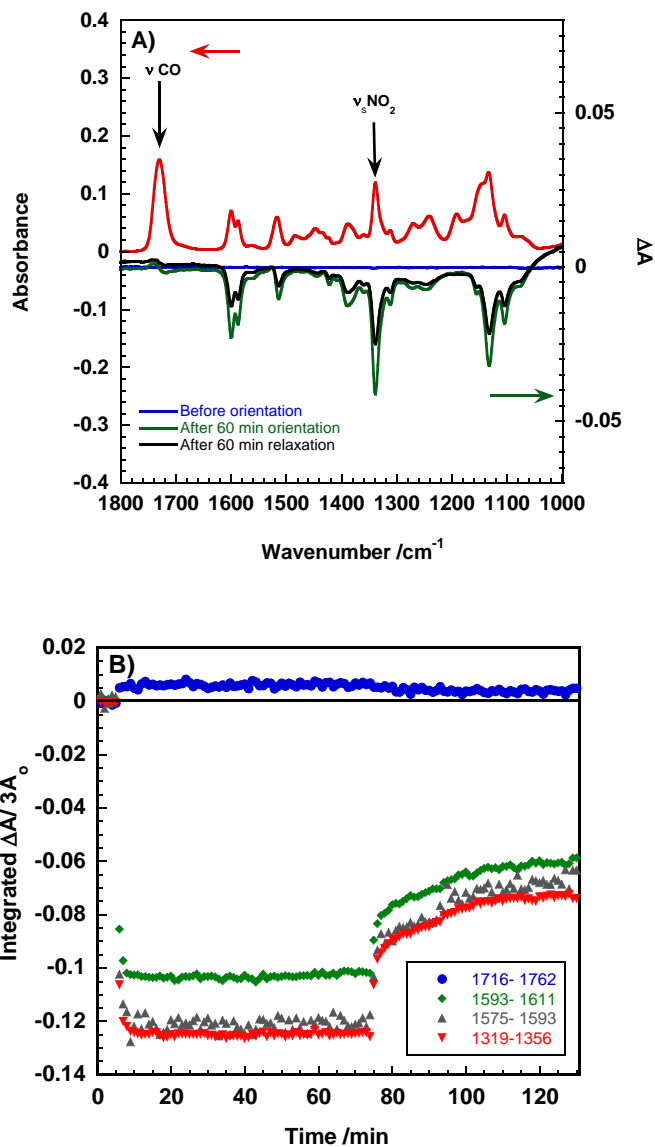**Figure A-9: (A) Infrared spectrum of a pDR1M thin film and photoinduced linear dichroism at t = 0 min., after 60 min. of orientation and after 60 min. of relaxation. (B) Dynamics of selected vibrational modes such as the stretching mode of C=O (1729 cm^{-1}), stretching phenyl modes ν_{8a} (1601 cm^{-1}) and ν_{8b} (1587 cm^{-1}), symmetric stretching mode of NO$_2$ (1341 cm^{-1}) during irradiation and relaxation cycles.**

A.10 Vibrational Assignments

Table A-1: Assignments of the main vibrational bands of the triphenylamino azo compounds.

Vibrational mode	Wavenumber
Deformation (-C=C-)	1107 cm^{-1}
Deformation (-C=C-)	1136 cm^{-1}
ν (φ-N)	1294 cm^{-1}
ν_s (-NO$_2$)	1343 cm^{-1}
ν (-N=N-+ Ph-N)	1395 cm^{-1}
ν_{as} (-NO$_2$)	1516 cm^{-1}
ν (-C=C-) 8b	1588 cm^{-1}
ν (-C=C-) 8a	1600 cm^{-1}
ν_s (-C=O)	1731 cm^{-1}
ν (-CN)	2227 cm^{-1}
ν_{as} (-CF$_3$)	1057 cm^{-1}

Appendices

B   Standard Operating Protocol (SOP) of SHG microscope

Here a standard operating protocol to use the second harmonic generation is illustrated. The listed steps to operate this setup are recommended. The current version of LabVIEW is Version 13.0f2(32-bit). Now the program to control the setup is version 1.3.

B.1   Power on

A-1. Check the APDs and make sure the both the APD is off if the light is on.

A-2. Check the chiller of femto-second laser. Make sure the temperature is 18 Celsius degree, and enough DI water is left in the chiller.

A-3. Check the shutter is off.

A-4. Switch the first flipper mirror at the femto-second laser upright to guide the laser into SHG microscope system.

A-5. Turn on the LASER ON sign. Turn on the femto-second laser. See to the operator's manual[1] for the details. Record the current of Verdi-V5 working at 5V output voltage in **A-6**. the Leica system log book. Use the oscilloscope to make sure the femto-second pulse is at good condition.

A-7. Power on the rotational motor of half-wave plate.

A-8. Power on the controller of piezo stage(PI nano^{TM} Piezo Stage Controller). Check the servo control for CH 1, CH 2 is ON state to remain close loop state.

A-9. Check the CCD is connected to the computer with a USB cable.

A-10. Turn on the computer. Start the LabVIEW. Click on SHG Microscope_1.3.vi. Once the loading is finished, click *Run* button to run the program. Wait for several seconds. Once the startup is finished, the piezo stage will be moved to near (50,49).

B.2   Sample load and Laser focus

B-1. Gently turn the knob of the vertical translation stage(Component 15) counter-clockwise, to lower the objective.

B-2. For a 22 mm microscope cover-slip, load the aluminum sample holder on the PI microscope slide holder. Load the sample on the aluminum sample holder, facing down.

B-3. Transfer the PI microscope slide holder into the piezo stage. Tighten the four screws. Avoid applying too much press on the piezo stage.

B-4. Turn the fiber optic illuminator on as a light source.

B-5. Switch the thin round cover-slip before the CCD to the reflection position(under the objective) to reflect the light into the CCD.

B-6. Start the software(UC480 Viewer), and use Live video mode to get a visible image.

B-7. Lift up the objective by turning the knob(Component 15) clockwise until a clear image is displayed on the screen.

B-8. Flip the silver mirror(Component 9, Figure 5-2b) up. Turn the shutter on. Make sure the femto second laser is leaded into a power meter.

B-9. Use the manual rotation mount for the first waveplate to adjust the power of the femto-second laser to about 10 mW.

B-10. Close the shutter to block the laser. lower the flipper mount of the silver mirror. Open the shutter.

B-11. Adjust the focus of the objective until a clear and focused laser spot can be observed on the screen. This laser spot should be symmetric while focusing and defocusing.

B-12. Move the microscope stage manually, until the focused laser spot is within a interested(SHG active) area on the sample.

B-13. Slightly raise the objective by a little until the laser spot on the screen is about 1/4 of the screen. This number can be adjusted by experience. Because normally the right working distance between the visible light and the laser is not the same. The visible light is not parallel.

B-14. Close the shutter. Turn the fiber optical illuminator off. Switch the round cover-slip away. Turn off any light in the lab. Make sure there is no light in the lab.

B-15. Turn both APDs on. Check the readings for the two APDs in *Parameters* tab, Figure 5-10. Check the sealing of the black tissue and the box to eliminate any possible light noise if the reading is not at 20-200 range.

B-16. Enter a trial scan range and resolution in Figure 5-6. The range can be between 5 to 20, and resolution is recommended to keep at 50 pix.

B-17. Start the scan. Switch to *Parameters* tab. While the scan is undergoing, change the focus little by little, until you see a peak in *APD1/2*.

B-18. If there is no peak until the scan is finished, open shutter, turn off the APDs and turn on the illuminator. Go to **B-12**.

 B-19. Stop the scan. Switch to *Intensity map* tab. Find the bright spot. Mover cursor to the bright spot. If the cursor can't be seen, click *RESET CURSOR* in *Parameters* tab. Click *GO CURSOR* to move piezo stage to that position.

B-20. Switch to *Parameters* tab. Switch *(OFF) Shutter (ON)* to ON state. Adjust the focus by looking at *APD 1/2* below, until the photon counts reach the maximum and stable. Switch *(OFF) Shutter (ON)* to OFF. Now the laser is focused.

B-21. The focus can be checked during the experiment or anytime. To do so, open shutter, turn off the APDs, turn on the illuminator and go to **B-12**.

B.3   Surface scan, SHG map plot

C-1. Set the right polarization. Go to Polar plot tab, set the angle of waveplate in *Set angle [deg]*. If a y-polarized fundamental is preferred, 45 should be entered in *Set angle*

[deg]. Click *SET ANGLE*. Wait until the Polarization Direction indicator reaches the right polarization.

C-2. Define the scan area by using the one of the following way. The scan region should be within (0, 200). The step is recommended to be above 10 nm.

-X/Y start, X/Y end, X/Y step. Example: X/Y start=45. X/Y end=55, X/Y step=0.1.

-Range, Pix. Example: Range=10, Pix=100. Click Set range. Check the numbers in X/Y start, X/Y end, X/Y step.

C-3. Click *START SCAN* to start. There should be a "click" sound from the shutter. While the scan is running, the bottom right indicator will be green and the progress can be checked in *% finished* box.

C-4. When the scan is finished, there should be a "click" sound from the shutter and the indicator will be off.

C-5. To change the color bar manually, the Auto-adjust I needs to be switched off. Then select the number at the top of the color bar, and enter a reasonable number.

C-6. To save the image and data, click SAVE. Select the path and a file name, several files will be saved. For example, the file name entered is "Test8". There will be 5 files:

Test8: This file does not have any extension and can be opened by notepad.exe. It contains the numerical data. There groups of data is in the file leading with S/P/S+P stands for y-polarized/x-polarized/sum, respectively.

Test8.bmp: This is the image of the sum SHG intensity.

Test8.txt: contains several information of this scan, including the range, resolution and other helpful things.

Test8_h.bmp: This is the image of the x-polarized SHG intensity.

Test8_v.bmp: This is the image of the y-polarized SHG intensity.

C-7. To read the SHG intensity at specific pixel, drag the cursor onto that position. The intensity can be read in *Intensity at cursor*.

C-8. To move the piezo stage to a fixed position, drag the cursor on that position and click *GO CURSOR*. Or, select *Follow cursor* then drag the cursor on that position.

C-9. To eliminate the background temporally, press and hold on the button below *Background*. Release to get the image back the same.

B.4   Standard polarization analysis

D-1. Move the piezo stage so the laser will be frozen on the targeted location. To do so, See to **C-8**.

D-2. Switch to *Polar plot* tab. See to **C-1** to set the polarization to x-polarized(0 degree).

D-3. Click POLAR to start the polar plot. The sound from the shutter will be heard both when the scan is started and finished.

D-4. Click SAVE to save the data. Select the path and a file name, several files will be saved. For example, the file name entered is "Test9". There will be 5 files:

Test9: This file does not have any extension and can be opened by notepad.exe. It contains the numerical data. The first column is angle, indicating the polarization. The second and third column contains the photon counts per second for y-polarized and x-polarized second harmonic, respectively.

Test9_pp.bmp: This is the angular dependence of the sum SHG intensity.

Test9.txt: contains several information of this scan, including the current position and other helpful things. This can be used to check at which position this polar plot was done.

Test8_pp_h.bmp: This is the angular dependence image of the x-polarized SHG intensity.

Test8_pp_v.bmp: This is the angular dependence image of the y-polarized SHG intensity.

B.5   Advanced polarization analysis

E-1. After a scan is finished, switch to Intensity map tab.

E-2. Purge the *APP position* array by clicking *Clear* shown in Figure 5-8 if needed.

E-3. Select *Follow cursor*. Drag the cursor to one of the interested location. Click *Add Pos*. Repeat this step until all interested location(s) is/are all entered correctly. Use *Dlt Pos* to delete last location if needed.

E-4. See to **C-1** to set the polarization at 0 degree.

E-5. Enter angular resolution in APP angle points.

E-6. Click APP to start advanced polarization analysis. The sound from the shutter will
E-7. be heard both when the scan is started and finished.

E-8. Click SAVE to save the data. Select the path and a file name, several files will be saved. For example, the file name entered is "Test10". There will be 5 files:

Test9: This file does not have any extension and can be opened by notepad.exe. It contains the numerical data. Two groups of data are headed by VVVV and HHHH respectively. First column is the angle of waveplate. To get the polarization, this number needs to be multiplied by a factor of 2. From the second column to the second last one, is the photon counts per second collected at each location, entered in the *Add Pos* array. The last column is the average over these positions.

Test9_pp.bmp: This is the angular dependence of the sum SHG intensity.

Test9.txt: contains several information of this scan, including the current position and other helpful things. This can be used to check at which position this polar plot was done.

Test8_pp_h.bmp: This is the angular dependence image of the x-polarized SHG intensity.

Test8_pp_v.bmp: This is the angular dependence image of the y-polarized SHG intensity.

B.6   Power off

F-1. Turn APDs off.

F-2. Stop the SHG Microscope_1.3.vi.

F-3. Change the output of Verdi-V5 to 0.01 W. Turn the Verdi's shutter off. Turn the key counter-clockwise 90 degree to vertical position.

F-4. Turn the Mira 900F controller off. Turn the oscilloscope off.

F-5. Close LabVIEW and uc480 Viewer. Turn off computer.

F-6. Power off the shutter, piezo stage controller, rotation optical mount for waveplate.

F-7. If long term shutdown of Mira 900 is required, see to Operator's Manual.

(1) COHERENT, I. **1997**.

Copyrights

RE: Rights and permission questions for materials

CONTRACTS-COPYRIGHT (shared) <   >

Fri 2016-02-26 9:09 AM

To:Renjie Hou <   >;

Dear Renjie

The Royal Society of Chemistry (RSC) hereby grants permission for the use of your paper(s) specified below in the printed and microfilm version of your thesis. You may also make available the PDF version of your paper(s) that the RSC sent to the corresponding author(s) of your paper(s) upon publication of the paper(s) in the following ways: in your thesis via any website that your university may have for the deposition of theses, via your university's Intranet or via your own personal website. We are however unable to grant you permission to include the PDF version of the paper(s) on its own in your institutional repository. The Royal Society of Chemistry is a signatory to the STM Guidelines on Permissions (available on request).

Please note that if the material specified below or any part of it appears with credit or acknowledgement to a third party then you must also secure permission from that third party before reproducing that material.

Please ensure that the thesis states the following:
Reproduced by permission of the PCCP Owner Societies
and include a link to the paper on the Royal Society of Chemistry's website.

Please ensure that your co-authors are aware that you are including the paper in your thesis.

Regards
Gill Cockhead
Publishing Contracts & Copyright Executive

Gill Cockhead
Publishing Contracts & Copyright Executive
Royal Society of Chemistry,

Follow the Royal Society of Chemistry:
www.rsc.org/follow

Winner of The Queen's Award for Enterprise, International Trade 2013

From: Renjie Hou [mailto:]
Sent: 19 February 2016 22:30
To: CONTRACTS-COPYRIGHT (shared)
Subject: Rights and permission questions for materials

Dear RSC:

I am Renjie Hou, a Ph. D candidate at department of physics and astronomy of Western University in London, Ontario, Canada. This email is to acquire the permission to use my published paper "Second harmonic generation from gold meta-molecules with three-fold symmetry" accepted Feb. 12, 2016 in Physical Chemistry Chemical Physics.

Re: Copyright Permission Request

Francois Lagugne-Labarthet <   >

Tue 2016-03-15 4:42 AM

To:Renjie Hou <   >;

Yes I give you my official permission.

Prof. Francois Lagugne-Labarthet
Western University

On 2016-03-14 15:16 PM, Renjie Hou wrote:

> **Hello Dr. Lagugne-Labarthet,**
>
> **I am Renjie Hou, a Ph. D. candidate at department of Physics and Astronomy, Western University. This email is to acquire the permission to use an adapted version of Figure 2.3 and Figure 2.4 of "Tip-Enhances Raman Spectroscopy, Enabling Spectroscopy at the Nanoscale" by Nastaran Kazemi-Zanjani, supervised by you. The original/adapted mentioned figures are intended to be used in my Ph. D. thesis with this permission.**
>
> **Regards,**
> **Renjie Hou**
>
> Renjie HOU
> PhD Candidate
> Department of Physics and Astronomy
> Western University
> London, Ontario, N6A 3K7 Canada
> **Work Email:**
> **Work Phone:**

Curriculum Vitae

Name: Renjie Hou

Post-secondary   Nanjing University
Education and   Nanjing, Jiangsu, China
Degrees: 2007-2011 B.Sc. Physics

Related Work   Teaching Assistant
Experience   The University of Western Ontario
                    2011-2016

Publications:

(1) **Hou, R.**; Shynkar, V.; Lafargue, C.; Kolkowski, R.; Zyss, J.; Lagugné-Labarthet, F., "Second harmonic generation from gold meta-molecules with three-fold symmetry"; *Phys. Chem. Chem. Phys.* **2016**, *18*, 7956-7965.

(2) Snell, K. E.; **Hou, R.**; Ishow, E.; Lagugné-Labarthet, F., " Enhanced Rates of Photoinduced Molecular Orientation in a Series of Molecular Glassy Thin Films"; *Langmuir.* **2015**, *31*, 7296-7305.

(3) Vedraine, S.; **Hou, R.**; Norton, P. R.; Lagugné-Labarthet, F., " On the absorption and electromagnetic field spectral shifts in plasmonic nanotriangle arrays"; *Opt. Express.* **2014**, *22*, 13308-13313.

(4) Pashaee, F.; **Hou, R.**; Gobbo, P.; Workentin, M. S.; Lagugné-Labarthet, F., " Tip-enhanced Raman spectroscopy of self-assembled thiolated monolayers on flat gold nanoplates using Gaussian-Transverse and radially polarized excitations"; *J. Phys. Chem. C.* **2013**, *117*, 15639-15646.

(5) Fayyaz, S.; Tabatabaei, M.; **Hou, R.**; Lagugné-Labarthet, F,. " Surface-enhanced fluorescence: mapping individual hot spots in silica-protected 2D gold nanotriangle arrays"; *J. Phys. Chem. C.* **2012**, *116*, 11665-11670.

Presentations in national and international meetings:

Hou, R., Snell, K. E., Ishow, E. and Lagugné -Labarthet, F., "Study of Photoinduced Molecular Orientation of Azo Compounds Thin Films using Polarization Modulation Infrared Spectroscopy"; Surface Canada 2013, London, May **2013 [Poster]**

Hou, R., and Lagugné -Labarthet, F., "Second Harmonic Generation Microscopy from Non-centrosymmetric Gold-coated Polystyrene Spheres"; Photonics North 2015, Ottawa, June **2015 [Oral]**